2016

Quantum Radiation Pressure Noise: Exposing the Quantum Mechanics of Optomechanical Interactions

Robinjeet Singh
Louisiana State University and Agricultural and Mechanical College, roubein@gmail.com

QUANTUM RADIATION PRESSURE NOISE: EXPOSING THE QUANTUM MECHANICS OF OPTOMECHANICAL INTERACTIONS

A Dissertation

Submitted to the Graduate Faculty of the
Louisiana State University and
Agricultural and Mechanical College
in partial fulfillment of the
requirements for the degree of
Doctor of Philosophy

in

Physics and Astronomy

by
Robinjeet Singh
Bachelor of Science (Honors School), Guru Nanak Dev University, 2004
M.Sc. (Honors School) Physics, Guru Nanak Dev University, 2006
Master of Science, Louisiana State University, 2013
December, 2016

This thesis is dedicated to the everlasting memories of my knight in shining armor, my beloved father.

THIS IS TO YOU DAD!!

Without you and your believe in me, it wouldn't have been possible. I know that you would have been so proud, I would give anything to have you here with me. You were my best friend, my mentor, my wall to lean on, and my shield from all the evils of the world. Although, I feel grateful to be able to spend together the last few days of your life, I wish those moments would have lasted forever.

I love you and will always miss you!!

Acknowledgments

First and foremost I would like to acknowledge the valuable guidance and push in the right direction from my thesis advisors Dr. Jonathan Dowling and Dr. Thomas Corbitt. Without their support and advice, especially through the hardest time of my life, this wouldn't have been possible. I truly feel lucky to have the two most wonderful people as my mentors. But as Jon says, it is the time for the baby bird to fly the nest.

I would also like to thank Dr. Eugeniy Mikhailov and Dr. Irina Novikova from the Physics Department of William and Mary College, for giving me an opportunity to work with them on my first experimental project in the field of Quantum Optics. It was truly a stepping stone towards my career as an experimental physicist.

I thank Dr. Garrett Cole from the Crystalline Mirror Solutions, Dr. Nergis Mavalvala and Dr. Adam Libson from the LIGO labs at MIT, for the expert advice on the experiment.

I equally thank my thesis committee members Dr. Hwang Lee, and Dr. Daniel C. Cohen, and especially the LIGO spokesperson Dr. Gabriela González.

I also acknowledge and congratulate all of the hard working fellow colleagues and the members of the LIGO Science Collaboration.

I truly appreciate and feel loved for the patient support from my girlfriend Shelley. I will never forget the countless thesis writing nights that she stayed awake with me.

Finally, I thank for the unconditional love and support of my mother, my sisters and the rest of my family.

Table of Contents

List of Figures

Abstract

The detection of gravitational waves has further motivated the scientists to push horizons for an improved sensitivity sphere of the advanced LIGO. Below 100 Hz, design sensitivity of the advanced LIGO is predicted to be limited by the quantum backaction or the quantum radiation pressure noise (QRPN). In this thesis, I present the experimental progress towards the measurement of the QRPN. This work is in part an effort towards establishing a tabletop test experiment to calibrate the QRPN evasion through various proposed schemes, and further bring to light new nonlinear optomechanical dynamics.

The experiment consists of a high optical and mechanical quality microresonator used as a movable end mirror in a high finesse optical cavity. To effectively infer the quantum superposition of the optomechanical interactions, the optomechanical dynamics must be stabilized and the microresonator must be maximally decoupled from the noisy thermal environment. I demonstrate the optical dilution of the Brownian dissipation of the mechanical state of the microresonator, by exploiting the optical spring effect of the optomechanical system. I also discuss the pump-probe scheme where two fields are injected into the optomechanical cavity, for enhancing the optomechanical correlations and hence exposing the QRPN.

I further demonstrate a new scheme for the optical trapping of the mechanical state. Here we exploited the polarization dependent frequency shift effects of the birefringent microresonator test mass. Given the development towards the ability to manipulate the frequency shifts between the two polarizations of the input field, the technique may find potential use towards achieving the self stabilizing optomechanics to trap the macroscopic test mass in the desired mechanical state.

In the appendices, I also discussed the computational project to investigate the laser cooling of a two level atomic state by the stimulated emission. Given the effective control over the heat exchange between the atom and the entropy reservoir laser field, this technique serves potential towards the laser cooling of the macroscopic mechanical systems.

Chapter 1
Rise of Gravitational Wave Astronomy

1.1 Introduction

Gravitational Waves (GW) were predicted by Einstein in 1916 as ripples in the fabric of space-time. The wave solution to Einstein's field equation in the linear space-time metric indicates the existence of gravitational waves. The energetic catastrophic processes like supernovae, coalescing neutron stars, colliding black holes, and the remnant radiation from the Big Bang are some of the strongest sources of the gravitational waves in the known universe. The strain due to the gravitational waves produced from such violent events is very small and hence any nonlinear contributions of the spacetime metric are negligible for observations far away from the source. In this linearized gravity approach of general relativity, the metric tensor ($g_{\mu\nu}$) given by Eq 1, is approximated as perturbation of the flat Minkowski space $\eta_{\mu\nu}$. These minuscale, time dependent perturbations in the curvature of the space-time are caused by the accelerating masses and propagate with the speed of light as gravitational waves [1].

$$g_{\mu\nu} = \eta_{\mu\nu} + h_{\mu\nu} \tag{1.1}$$

The h term is the small perturbation that represent the gravitational wave. The gravitational wave propagating in the Z direction is expressed through the wave solution of Einstein's field equation, in terms of the dimensionless strain polarizations h_+ and $h_\times$ of gravitational waves.

$$h_{\mu\nu} = \begin{pmatrix} 0 & 0 & 0 & 0 \\ 0 & h_+ & h_\times & 0 \\ 0 & h_\times & -h_+ & 0 \\ 0 & 0 & 0 & 0 \end{pmatrix} \tag{1.2}$$

The first indirect evidence for the existence of gravitational waves came from the Hulse-Taylor binary in 1974 [2, 3]. The observed shrinking orbit of this inspiral pulsar-neutron star system was in direct correspondence with the predicted release of energy in the form of gravitational waves. Hulse and Taylor were awarded with the Nobel Prize in Physics in 1993, for pioneering work that further motivated the scientists for a more conclusive direct measurement of these gravitational waves passing the Earth.

The first direct detection of a gravitational wave was made on September 14th, 2015 by the two Advanced Laser Interferometer Gravitational-wave Observatory (Advanced LIGO) sites, one each at Livingston, Louisiana and Hanford, Washington [4]. The observed GW150914 signal, in agreement with the numerical relativity model, indicated the source of the waveform to be the final fractional second of the coalescence of binary black hole system. The two black holes with respective masses of about 36 and 26 times the solar mass collided and merged to form a single black hole of approximately 62 times the solar mass, while emitting 3 solar masses worth of energy in the form of gravitational waves [5]. Fig 1.1 shows the waveform of the observed GW150914 gravitational wave by the two Advanced LIGO sites [4].

This direct detection of the gravitational waves not only served as a testbed for the theory of general relativity but it also opened up a new era in the field of observational gravitational wave astronomy. The information imprinted onto the GW waveform is of great astrophysical importance due to the non-scattering nature of the gravitational waves. Hence such detections allow us to infer the far deep universe to answer the fundamental questions about the cosmos that we live in.

The orders of magnitude improvement in the sensitivity of the recently upgraded Advanced LIGO, is unarguably the main factor that led the two detectors towards making the first ever direct detection of the elusive gravitational wave phenomenon. Such improvement in the sensitivity goes in direct correspondence with the quality of detection and the volume of the universe that can be probed by the GW detectors. Hence, constant

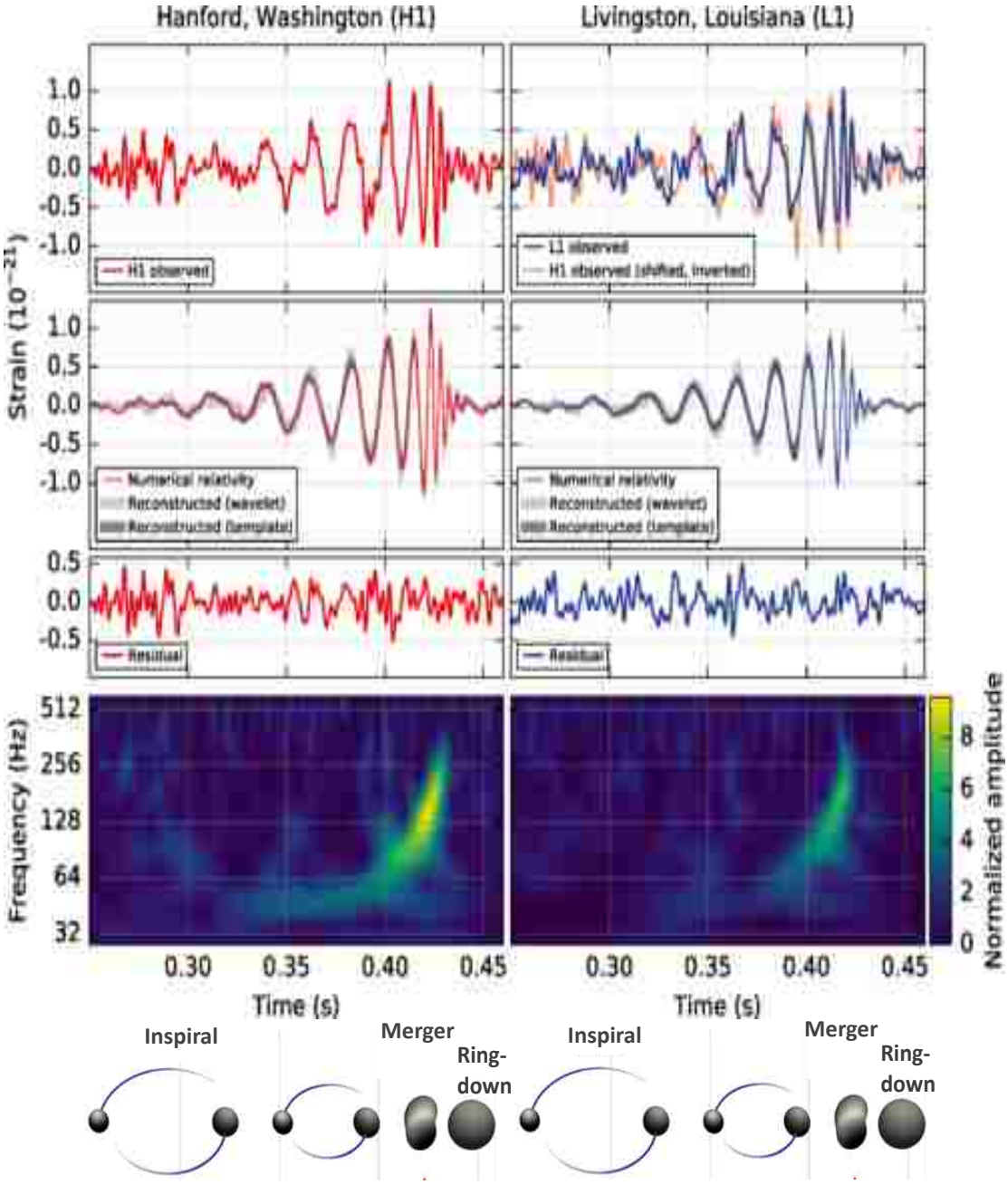

Figure 1.1: The observed gravitational wave GW150914 from the binary black merger, by the two US-led Advanced LIGO sites. H1 is the observed signal at Hanford, Washington site, and L1 is the observation at the Livingston, Louisiana [4].

efforts are always ongoing amongst the LIGO Scientific Collaboration (LSC), to improve the sensitivity of the next generation of GW detectors. Such efforts involve addressing the fundamental noise sources that limit the sensitivity of Advanced LIGO and further device the evasion schemes for these noises.

In this chapter, I will discuss about the brief history of the ground based GW detectors, the design consideration along with the sensitivity floor of Advanced LIGO, the limiting noise sources and the evasion schemes for the further improvement in the sensitivity of the GW detectors.

1.2 Introduction to the Gravitational Wave Detectors

The underlying idea behind the gravitational wave detectors is to build a transducer system that is sensitive enough to convert the minuscale distortions in the spacetime due to the gravitational waves, into a measurable signal. The strain caused by the effects of gravitational waves for instance from a binary neutron stars moving at relativistic velocities can be calculated as:

$$h \approx \frac{Gm}{rc^2} \tag{1.3}$$

where G is the universal gravitational constant, r is the distance between the Earth and the source of GWs, c is the speed of light. The strongest gravitational waves from the known sources in the observable universe is calculated to cause a strain of the order of h $\approx 10^{-21}$. Building a detector that is responsive to such a minuscale displacements require a state of the art measurement precision, and isolation from the ambient noise sources.

Joseph Weber designed the first ground based GW detector in the late 1950s. The device antennae in the form of large metal bars were designed to be set in motion by the gravitational waves predicted by Weber. The bars were seismically isolated and were held under high vacuum to reduce any acoustic noise [6]. Piezoelectric transducers were connected to the center of the device to measure the driven harmonic motion of the bar. Later improvement to Weber's design of resonant bar detector resulted in generations

resonant bar detectors that applied cryogenics to cool the antennae, and used superconduting readout devices (SQUIDS) to enhanced sensitivity measurement [7]. Further design upgrades included a spherical resonant mass to enhance the both linear and directional sensitivity of the detector [7, 8, 9, 10, 11]. Although some of these detectors are still operational and essentially focused on higher frequency gravitational waves, they lack in strain sensitivity bandwidth for the lower frequency gravitational waves from the most dominant sources.

Pulsar Timing Array detectors are the electromagnetic counterparts of the gravitational wave detectors, where the time of flight of the EM radiation from millisecond pulsars is measured and calibrated for the gravitational wave signal [12]. These milisecond pulsars are extremely stable rotating neutron stars that pose as sensitive probes for any irregularities in their environment. The upper limit to the background gravitational waves is expected to be set by tracking any shift in the arrival time of pulses from these pulsars.

The development in the laser technology and the field of laser interferometry led to various prototype experiments for gravitational wave interferometers primarily by Forward and his colleagues in late 1960s [13] and then by Weiss in 1970s [14]. These experiments along with the theoretical investigations by Kip Thorne for the sources of gravitational waves [1], laid a foundation towards the new generation of GW detectors based on laser interferometry. These modified Michelson interferometer gravitational wave detectors utilize the time of flight of the laser field hitting the quasi-free mirrors that are used as test masses, to measure the differential displacement between the orthogonal arms of the interferometer [15].

Fig 1.2 demonstrate the effects of the gravitational waves that distort the spacetime metric, onto the orthogonal arms ($L_X = L_Y$) of a simple Michelson interferometer. In case of no gravitational waves and perfectly symmetric interferometer arms, the phase accumulated by the laser light in the each arm of the interferometer should be equal and opposite. Hence any light field from one arm, entering the dark or antisymmetric port of the interferometer, will destructively interfere with the light field from the orthogonal

arm of the interferometer. Therefore the photodetector in the antisymmetric port will ideally see no photons in the absence of any strain that changes the differential arm length of the interferometer. As h_+ or $h_\times$ polarizations of the gravitational waves enter the interferometer, the x and y arms of the interferometer experience a differential increase or decrease in the length. The asymmetry introduced in the two arms, by the gravitational waves will cause a net phase shift between the light field traveling in the x and the y arms, respectively. In principle, this phase shift can be measured and calibrated at the antisymmetric port of the interferometer, to infer the strain caused by the gravitational waves.

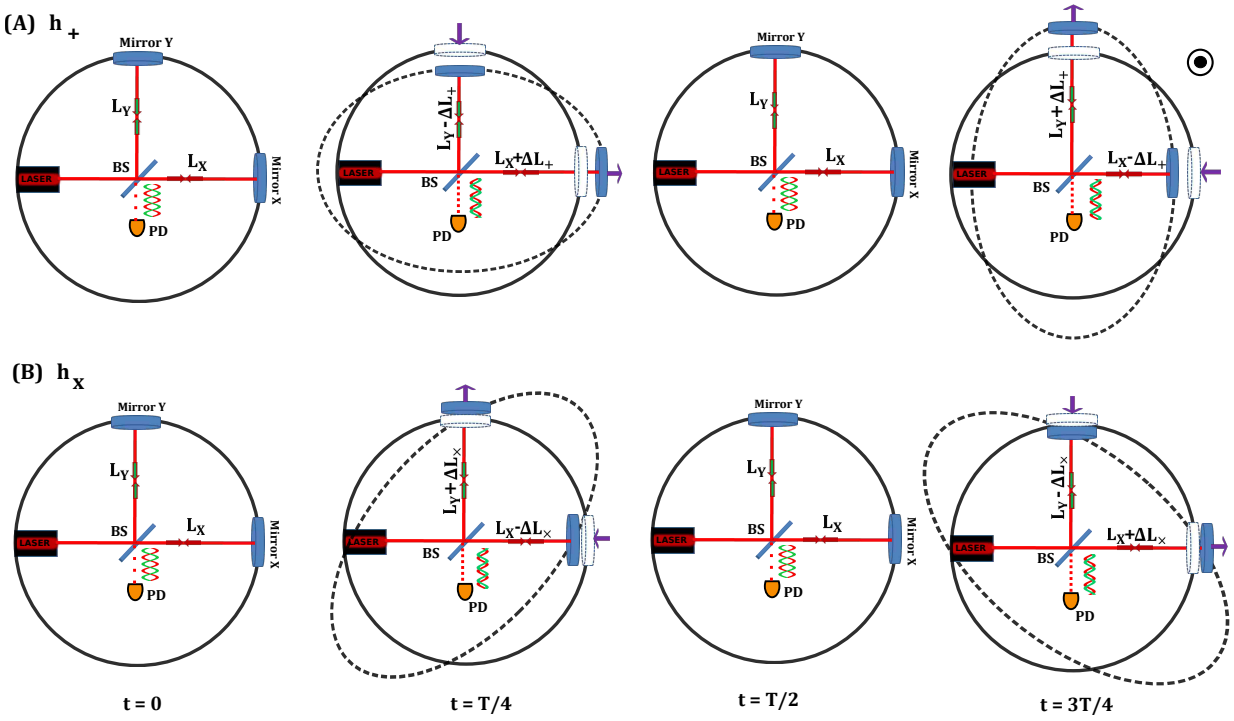

Figure 1.2: The effect of gravitational wave on a symmetric Michelson interferometer with $L_X = L_Y$. The gravitational waves are propagating in Z direction with a wave period T. Set of figures (A) represent a differential squeezing and antisqueezing of the arms of the interferometer, as a function of the period of the gravitational wave in h_+ polarization. (B) is the effect of gravitational waves in $h_\times$ polarization, entering the interferometer. ΔL_+ and $\Delta L_\times$ are the displacements of each arm of the interferometer, caused by the respective polarizations of the gravitational wave. BS represent a $50:50$ beam splitter, and PD is a photodetector.

In terms of technical challenge, the interferometer's test masses should be isolated from all the noise sources that will normally mask the gravitational wave signal. As a first stage of seismic isolation, test masses are normally suspended in the form of pendulum with a resonant frequency much lower than the frequency of the gravitational waves to be detected. This condition is necessary for the test masses to behave quasi-free for the gravitational waves to act on. Further degrees of isolation include state of the art isolation suspension, actuations and feedback control of the ambient motion of the test masses.

The most prominent amongst the interferometer based gravitational wave detectors are the two recently upgraded advanced Laser Interferometer Gravitational wave Observatory (Advanced LIGO). Since the inception of the initial idea by Weiss, Thorne, and Drever; about three decade's worth of collaborative efforts of the LIGO team led to a breakthrough with the first ever direct detection of the gravitational waves on Sept 14, 2015 [4]. This detection, as discussed before, gave a new momentum towards the efforts to build an ever expanding web of both land and space based GW detectors. Such network of detectors is crucial for improved parameter estimation, and sky localization [16] of gravitational waves from sources in broader ferquency spectrum. To name a few ongoing efforts towards this progress of making more sensitive detections; the upgrade of the Italian GW interferometer (Advanced VIRGO) is underway, construction of the cryogenic counterpart (KAGRA) is promising, European Space Agency (ESA) recently launched LISA Pathfinder for the feasibility test of the Evolved Laser Interferometer Space Antenna (eLISA), the third site for Advanced LIGO is commissioned to be built in India.

In order to make a measurement sensitive to the displacement caused by the gravitational wave, the time of flight of the laser field from the beam splitter to the end mirror of one of the arm of the Michelson interferometer, should be equal to one-fourth the wave period of the gravitational wave. Taking into account the double flight of the laser back to the beam

splitter, the total time (t) required to make a sensitive measurement is given as:

$$t = \frac{T}{2} \Rightarrow \frac{2L}{c} \tag{1.4}$$

where c is the speed of light, $T = 1/f$ is the wave period of the gravitational wave of frequency f, and L is the length of one arm of the Michelson interferometer. For a gravitational wave of frequency 100 Hz, the time of flight to and from the end mirror of the interferometer is of the order of 0.005 seconds.

The above condition requires that in order to measure the differential change in the length, the length of each arm of the interferometer should be equal to 750 kilometers. Building such a long interferometer is not only technically infeasible but also unnecessary. In the interferometric GW detectors, the Michelson interferometer is extended with a high finesse Fabry-Perot cavity at the end of each arm. The role of the Fabry-Perot cavity is to increase the storage time and hence the effective optical path length of the laser field. In terms of the strain amplitude caused by the gravitational wave (h), if m is the number of round trips made by the light field before exiting the cavity of length L, the effective optical path length is $L_{\text{eff}} \rightarrow mL$ such that:

$$h = \frac{\Delta L}{L_{\text{eff}}} \tag{1.5}$$

where $\Delta L = L_X - L_Y$ is the differential change in the lengths of the interferometer arms, h is a linear combination of h_+ *and* $h_\times$ polarizations. In terms of phase difference ($\Delta\phi$) between the laser beams from the two arm cavities, caused by the gravitational wave amplitude h that stretches the interferometer's arm in X direction and squeezes in Y direction.

$$\Delta\phi = \delta\phi_X - \delta\phi_Y \rightarrow \frac{4\pi}{\lambda}[m(L_X + \delta L_X) - m(L_Y - \delta L_Y)] \rightarrow \frac{4\pi m}{\lambda}\Delta L \tag{1.6}$$

1.3 Noise Budget of Advanced LIGO

1.3.1 Classical Thermal Noise

The two Advanced LIGO detectors are dual-recycled, extended Michelson interferometers with four kilometer long Fabry-Perot cavities at the end of each arm of the interferometer. A schematic description of the core optics of Advanced LIGO is given in Fig. 1.3. The recently upgraded Advanced LIGO uses optical test masses that are 40 kgs in mass, 34×20 centimeters in the diameter and the thickness, and are made from a high purity, homogenous fused silica. The optical test masses are coated with alternating layers of SiO_2 and TiO_2 doped Ta_2O_5 for creating highly reflective surface with ultra low absorption and scattering losses [17].

The phase sensitivity at the optical readout of Advanced LIGO is maximized as a result of combined effective gain contributions due to the long resonant (Fabry-Perot) cavities (G_{FP}), the power recycling [18] at the symmetric port input of the beam splitter (G_{prm}), and the use of signal recycling mirror (SRM) at the antisymmetric port of the beam splitter (G_{srm}) [19].

Advanced LIGO like any other physical system, is prone to various noise sources that may deteriorate the phase measurement at the optical readout or may limit the displacement sensitivity by contaminating the inertial nature of the test masses. At the lower-frequency region of the detector's bandwidth, the strain sensitivity is limited by the coupling of the seismic driven motion of the test masses. Such vibrations are normally actuated by various Human activities or wind currents, and scale as $1/f^2$ above the eigenfrequency of mechanical motion of the test mass. The typical range of these vibrations is about $10^{-8}\mathrm{m}/\sqrt{\mathrm{Hz}}$ at 1 Hz and above. Further, various microseismic activities and their upconversions pose challenge towards the normal operation of the detector. In order to minimize the effects of these seismic activities onto the strain sensitivity of Advanced LIGO, the optical test masses should be seismically isolated along with stringent active cancellations of the micro-seismic activities.

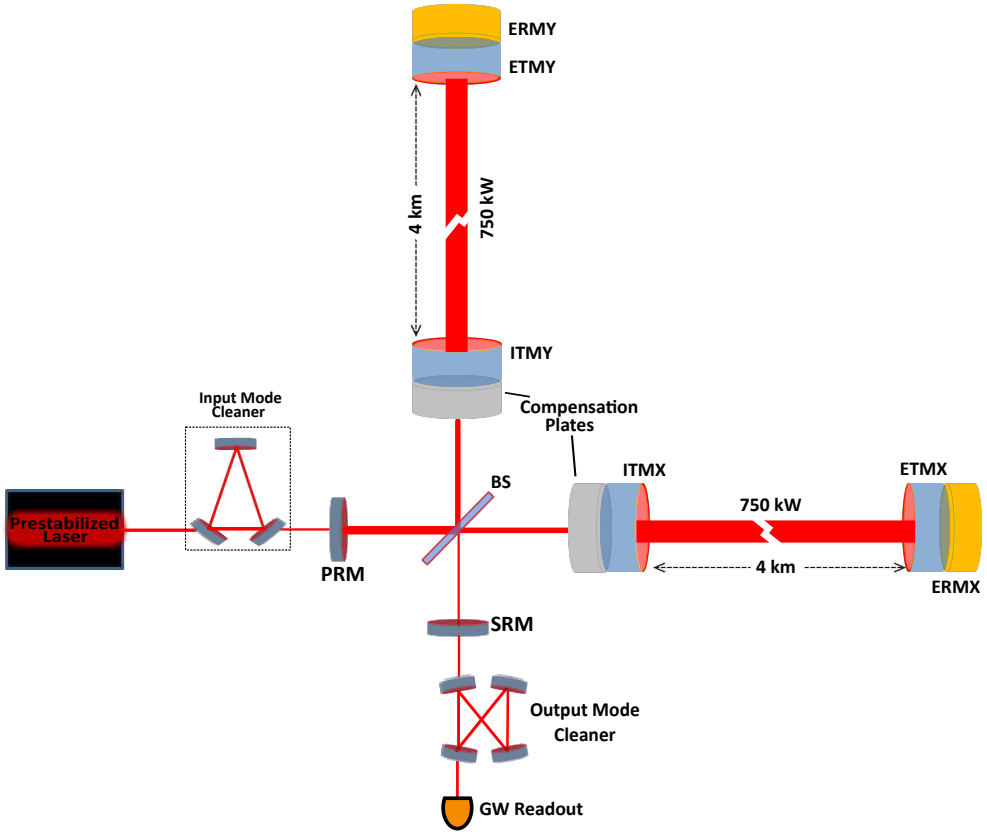

Figure 1.3: The schematic showing the essential optical layout of the dual recycled Advanced LIGO detector. After the amplifier stage (not shown), the maximum output power capacity of the prestabilized laser is 180 Watts. The Input mode cleaner is a traingular cavity with 32.9 m of optical path length that filter out higher order tranverse modes and further stabilize the frequency of the input laser. A set of partially reflective Power Recycling Mirrors (PRM) are used to further amplify the power at the beam splitter by about 40 orders of magnitude. The Beam Splitter (BS) splits the beam equally towards the two orthogonal arms of the Michelson interferometer. Each arm of the interferometer is extended with a coupled high finesse resonator cavity that is 4 kms in length. These Fabry-Perot cavities consist of a pair of quadruple pendulums with 40 kgs Input and End Test Masses (ITMX, ITMY, ETMX, and ETMY), in each. The resonator Fabry-Perot cavities are designed to effectively increase the optical path length by about 300 orders of magnitude, hence enhancing the detection bandwidth. Compensation plates are used to correct the optical curvature mismatch of the test masses. The design circulating power in each of the 4km long Fabry-Perot cavity, at full sensitivity of Advanced LIGO, is about 750 KW. The End Reaction Masses (ERMX, ERMY) provides reference to prevent any ambient noise from re-entering the test masses. A partially reflective Signal Recycling Mirrors (SRM) is used both for enhanced signal detection and tuning the gain-bandwidth of the differential arm-sensitivity. An output mode cleaner is a 1.3 m optical path length bowtie cavity that filter the unwanted spatial and periodic components of light [19].

As a first chain of seismic isolation, the test masses are suspended in the form of quadruple pendulums with a very soft mechanical spring constant of mechanical eigenfrequency (f_m) about 0.4 Hz. The multistage pendulum in combination with active isolation and reference reaction mass, effectively attenuate the ground vibrations by seven orders of magnitude at the optical test mass.

The suspended test masses are further mounted upside down to active isolation stages that provides additional three orders of seismic isolation. These active isolation platforms are also used to minimize the motion due to tidal forces, earthquakes, and other microseismic activities. Additional active cancellation and servo control may be required to stabilize the inertial frame of the seismic isolation and to mitigate the effects due to the self noise of the various feedback loops, and the limiting Newtonian noise below 20 Hz.

To prevent from the acoustic shortening of the seismic isolation and Rayleigh scattering of the optical readout, the core optics of Advanced LIGO reside in an ultra high vacuum system in excess of 1×10^{-6} Pascal.

With the state of art isolation system, the displacement of the test masses is minimally coupled to the seismic vibrations at the center frequency of detection bandwidth. One of the fundamental noise sources at this level are the Brownian impacts of the molecules in the material of the suspension [20, 21], test mass substrate [22, 23] and the reflective coating of the optical test mass [23, 24, 25]. These classical thermal fluctuations limit the strain sensitivity at around 100 Hz for Advanced LIGO. These dissipative thermal forces are guided by the fluctuation dissipation theorem, and can be quantified in terms of the thermal fluctuation spectral density as [24]:

$$x^2(\omega) = \frac{4k_B T}{m\omega} \frac{\omega_o^2/Q}{(\omega^2 - \omega_o^2)^2 + \omega_o^4/Q^2} \tag{1.7}$$

where $Q \approx 1/\phi$ is the quality factor of the mechanical oscillator given by f_o/f_{FWHM} for f_{FWHM} the bandwidth of oscillator natural frequency, ϕ is the loss angle of the pendulum

that quantify dissipation of the mechanical system, T is the ambient temperature of the oscillator, k_B is the Boltzmann's constant, $\omega_o = 2\pi f_o$ is the fundamental frequency of the mechanical oscillator. The Eq 1.7 tells that in order to minimize the thermal fluctuations the mechanical quality factor of the test mass pendulum should be as high as possible. It further suggests in other words in order to minimize the energy flow into the mechanical system, the test masses should be maximally decoupled from the noisy environment. This condition require for the mechanical spring to be as soft as possible.

Further in Advanced LIGO the test masses are suspended through very thin monolithic glass fibers. This prevents any contact noise from entering the test masses. The heavy test masses with low mechanical eigenfrequency along with thin suspension fibers also reduce the effective dissipation losses because of the negligible low frequency moment of motion of the suspension fibers. This dilution of the mechanical losses is called gravitational dilution, where the fraction of energy imparted to the pendulum is stored as noiseless gravitational field. The quality of the pendulum (Q_p) is effectively enhanced as a ratio of the gravitational spring constant (k_g) and the elastic spring constant (k_{el}) . The relation between the effective quality factor of the pendulum (Q_p) to the quality factor of the suspension wire (Q_w) is given as [26]:

$$\frac{Q_p}{Q_w} = \frac{k_g}{k_e l} \Rightarrow \sqrt{\frac{4Tl^2}{n^2 EI}} \Rightarrow \frac{1}{D_{\text{dil}}} \tag{1.8}$$

where l is the length of the pendulum, T is the tension due to the weight of the suspended mass, n is the number of suspension fibers, E is the Young's modulus of the material, I is the moment of the cross section of the wire, and D_{dil} is the ″Dilution factor″. The moment of the suspension fiber is negligible at low mechanical frequency of oscillation, hence:

$$D_{\text{dil}} << 1 \tag{1.9}$$

This enhancement in the quality factor of the pendulum lead to longer thermal decohere-

nce time and hence mitigate the intrinsic thermal noise associated with the poor mechanical quality of the suspensions.

Thermal noise can obviously be reduced by applying cryogenics, various techniques are under ongoing investigations to effectively cool the test masses of the next generation of the LIGO and other gravitational wave detectors [27]. Cooling of the test masses by the known cryogenic techniques is especially challenging since a minimal contact must be made with the test mass, in order to preserve its inertial state.

While development of the cryogenic techniques for the GW detectors is underway, several groups have been investigating new coating materials that exhibit lower intrinsic thermal noise [28, 30, 31]. Recently Cole et. al. demonstrated the effective enhancement of the optical quality factor, along with reduction of the thermal noise in the test masses coated with crystalline reflective coating of GaAs/AlGaAs [68]. The low photo-absorption losses is another important characteristic of such crystalline coatings. Reduction of Brownian thermal noise in the coating and suspension, and losses due to photoabsorption are crucial to expose the quantum superposition between the test masses and the laser field.

In the later chapter, I will discuss further details about the thermal noise performance of microresonator structures fabricated by the stacked layers of GaAs/AlGaAs material. This work is in part an effort towards calibration and evasion of the quantum noises in the displacement sensitivity of the optomechanical interactions.

1.3.2 Photon Shot Noise

In classical interferometry, the measure of interference between the light from the two arm cavities can be measured with an arbitrary precision. The laws of quantum mechanics however impose a bound on such precision owing the discrete nature of the laser field. In Advanced LIGO, the reflected light from the test masses is calibrated at the optical readout of the antisymmetric port to reveal the differential displacement of the test masses due to local and non-local forces. The photon shot noise is the uncertainty in the measurement of displacement sensitivity of the interferometer that arise in quantum statistical picture. The

fluctuations in the arrival time of photons onto the photodetector of the optical readout is governed by Poissonian distribution.

Thus for N photons, the error in the detection of small displacements of the test mass falls as $1/\sqrt{N}$. The number of photons available for detection at the antisymmetric port depends on the laser power output from the antisymmetric port $P_{AS_{\rm out}}$, and the time available for the measurement (t). For gravitational wave of frequency $f = 1/t$, the total number of photons available for detection are:

$$N = \frac{cP_{\rm AS_{out}}}{2\pi\hbar f\lambda} \tag{1.10}$$

where, $\hbar$ is the reduced Planck's constant, c is the speed of light, and λ is the wavelength of the laser light.

The variables that control the $P_{\rm AS_{out}}$ can be identified by quantifying the response of a simplified Michelson interferometer as shown in Fig 1.4.

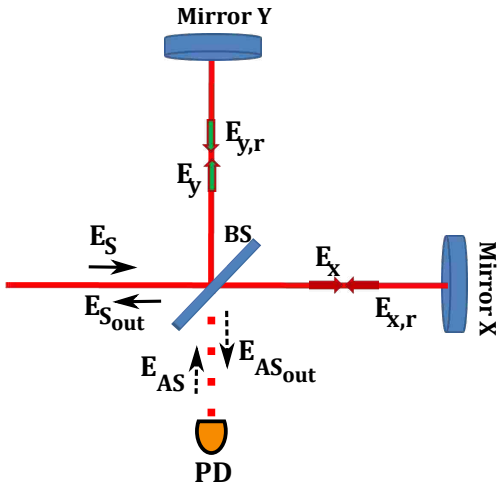

Figure 1.4: A cartoon of the basic Michelson interferometer, with input field E_S at the symmetric or bright port of the interferometer's beamsplitter (BS). E_x amd E_y are the fields input into the respective x and y arms of the interferometer. $E_{x,r}$ and $E_{y,r}$ are the fields reflected from the end mirrors in the x and y arms, respectively. E_{AS} is the input and $E_{AS_{out}}$ is the output fields at the antisymmetric or dark port of BS.

The power available for the optical readout at the antisymmetric port of the interferometer

is given by:

$$P_{\mathrm{AS_{out}}} = \mid E_{\mathrm{AS_{out}}} \mid^2 \tag{1.11}$$

Assuming an ideal 50% beamplitter, the field E_S entering the interferometer through the symmetric port is split equally into the x and y arms. Ignoring any field contributions E_{AS} due to the vacuum vacuum fluctuations entering the dark port of the interferometer, $E_{\mathrm{AS_{out}}} = E_{x,r} - E_{y,r}$. Here the fields $E_{x,r}$ and $E_{y,r}$ are the fields entering the BS after reflections by x and y end mirrors of each arm, respectively. Assuming the end mirrors to be perfectly reflective $r_{x,y} \approx 1$

$$E_{AS_{\mathrm{out}}} = \frac{E_S}{2}\left[e^{i2kL_x} - e^{i2kL_y}\right] \tag{1.12}$$

For the lengths L_x and L_y of the two arms of the interferometer to be equal, the two reflected beams passing through the beam splitter are π out of phase. Hence following the small angle approximation power falling on the dark port photodetector is:

$$P_{\mathrm{AS_{out}}} = P_S(\sin^2(\Delta L)) \tag{1.13}$$

where $\Delta L = L_x - L_y$ is the difference in the lengths of two arms that accommodate for any relative displacement of the test masses. $P_S = \mid E_S \mid^2$ is the input power at the symmetric port of the beam splitter.

The resolution of the minimum detectable displacement of the two arms of the Michelson sensitivity is a function of the size of the fringe or the wavelength of the laser light. In the GW detector, this resolution falls due to shot noise limit as:

$$\Delta L \quad \Rightarrow \frac{\lambda}{\sqrt{N}} \quad \Rightarrow \sqrt{\frac{2\pi\hbar f\lambda^3}{cP_S(\sin^2(\Delta L))}} \tag{1.14}$$

The above Eq 1.14 dictates the shot noise limited sensitivity of Advanced LIGO at the higher frequency region of the detection bandwidth. It may seem obvious to increase

the input power at the beamsplitter, to enhance the shot noise limited strain sensitivity. However, at higher laser powers, the amplitude of the intensity fluctuations in the laser fields impose a bound to the uncertainty domain of the measurement.

1.3.3 Quantum Radiation Pressure Noise

The radiation pressure exerted onto the test masses by the laser field is dependent on the intensity of the laser field monitoring the test masses. Any fluctuations in the laser field intensity will therefore cause perturbations in the inertial properties of the test masses. These perturbations are encoded as phase shifts in the light field being reflected from the test masses.

Although the laser field intensity is normally controlled by stabilization loops, the laws of quantum mechanics impose a limit to the uncertainty of the zero point fluctuations in the amplitude the laser field intensity. These quantum fluctuations in the laser power produce a back-action force known as the Quantum Radiation Pressure Noise (QRPN), given for reflection as:

$$F_{\mathrm{QRPN}} = \frac{2\delta P}{c} \tag{1.15}$$

where δP are the power fluctuations in the field hitting the test mass. The power fluctuations in the optical field entering the arm of interferometer through the bright port are normally negligible at the asymmetric port, either due to the active cancellations or destructive interference. The vacuum or zero point fluctuations that enter the asymmetric port of the interferometer, however may lead to significant noise in the measurement.

To construct a mathematical framework for the effects of these vacuum fluctuations, the optical field should be quantized [32, 33, 34, 35]. In Heisenberg picture, the time evolution of the quantized optical field can be represented in terms of positive and negative frequency

components while normalizing over the slowly evolving spatial modes, as [36]:

$$E(t) = \begin{bmatrix} \cos(\omega_o t) & \sin(\omega_o t)) \end{bmatrix} \begin{bmatrix} E^+(t) \\ E^-(t) \end{bmatrix} \rightarrow \int_0^\infty \frac{\mathcal{A}_o}{2} \hat{a}_\omega e^{-i\omega t} \frac{d\omega}{2\pi} + \quad \text{H.C.} \tag{1.16}$$

where

$$\mathcal{A}_o = \sqrt{\frac{4\pi\hbar\omega}{\mathcal{A}c}} \tag{1.17}$$

$\mathcal{A}$ is the effective cross-sectional area of the optical beam, $\hat{a}_\omega$ and the conjugate $\hat{a}^\dagger_\omega$ are the annihilation and creation operators representing the photon state of the optical mode with frequency ω. For the condition satisfying independent modes of the photon field, the operators $\hat{a}_\omega$ and $\hat{a}^\dagger_\omega$ obey the commutation relation as:

$$\left[\hat{a}_\omega, \hat{a}^\dagger_{\omega'}\right] = 2\pi\delta(\omega - \omega'), \quad \text{and} \quad [\hat{a}_\omega, \hat{a}'_\omega] = \left[\hat{a}^\dagger_\omega, \hat{a}^\dagger_{\omega'}\right] = 0. \tag{1.18}$$

Under the low circulating power conditions, the output light field coming out of the interferometer can be considered as a wave of independent modes with independently resolvable phase shifts induced by the mirror motion. These phase shifts can be seen as the upper and lower sidebands ($\hat{a}_\pm = \hat{a}_{\omega_o \pm \Omega}$) around the carrier frequency.

In high power GW interferometers however, the phase shift induced sidebands of the output light field are parametrically modulated due to the radiation pressure induced test mass motion. Such modulations can be seen as paired modes of light with frequencies $\omega \pm \Omega$ with correlated complex amplitudes. Hence to study the dependence of the displacement sensitivity of the optical readout on the quantum radiation pressure noise, the laser field should be treated in a two photon formalism that was originally developed by Caves and Schumaker [37, 38, 39]. The associated annihilation operators, in this correlated two photon

mode description of the optical field are [34]:

$$\hat{a}_1 = \frac{\hat{a}_+ + \hat{a}_-^\dagger}{\sqrt{2}} \quad , \qquad \text{and} \qquad \hat{a}_2 = \frac{\hat{a}_+ - \hat{a}_-^\dagger}{\sqrt{2}i} \tag{1.19}$$

where $\hat{a}_{1,2}$ are the quadrature operators of the electric field that obey the commutation relation:

$$\left[\hat{a}_1, \hat{a}_2^\dagger\right] = -\left[\hat{a}_2, \hat{a}_1^\dagger\right] \Rightarrow i2\pi\delta(\Omega - \Omega^{'}) \tag{1.20}$$

Under this formulation and the assumption of ideal beamsplitter (lossless, and precisely 50%), the input vacuum fluctuations at the dark port of the interferometer is given as:

$$\delta E_{AS}(t) = \frac{\mathcal{A}_o}{2\pi}\begin{bmatrix} \cos(\omega_o t)\int_0^\infty (\hat{a}_1 e^{-i\Omega t} + \hat{a}_1^\dagger e^{-i\Omega t})d\Omega \\ +\sin(\omega_o t)\int_0^\infty (\hat{a}_2 e^{-i\Omega t} + \hat{a}_2^\dagger e^{-i\Omega t})d\Omega \end{bmatrix} \tag{1.21}$$

The electric field incident on the each arm of the interferometer is given as:

$$E_{x,y}(t) = \frac{1}{\sqrt{2}}\left[E_S(t) + \eta\delta E_{AS}(t)\right] \tag{1.22}$$

where η is ± 1 for y and x arms, respectively.

For the interferometer arm lengths adjusted to an integer multiple of the carrier wavelength, the overall time shift can be normalized over an integer multiple. The displacement $\delta L_{x,y}$ of the mirrors in the two arms, produced by the radiation pressure or the gravitational waves, causes a phase shift in the reflected carrier field such that under the assumption of small displacement.

$$E_{(x,y),r}(t) \approx \frac{1}{\sqrt{2}}\left[E_S(t - \tfrac{2L_{x,y}(t)}{c}) + \eta\delta E_A S(t)\right] \tag{1.23}$$

I have ignored any phase shifts in the vacuum field entered through the asymmertic

port of the interferometer. Therefore field exiting the asymmetric port is given as:

$$E_{AS_{\text{out}}} \approx \frac{1}{2}\Big[E_S(t - \tfrac{2\delta L_y(t)}{c}) + \delta E_{AS}(t) - E_S(t - \tfrac{2\delta L_x(t)}{c}) - \delta E_{AS}(t)\Big]$$

$$\approx \left[\delta E_{AS}(t) + \sqrt{\tfrac{4\pi P_S}{\mathcal{A}c}}(\Delta L)\sin(\omega_o t)\right] \tag{1.24}$$

For an ideal filtered output, any classical noise effects that modulate the carrier frequency are rejected. Hence ΔL is the arm length difference primarily caused by the back action due to the radiation pressure and the gravitational wave.

$$\Delta L = L\tilde{h} + \delta L_{\text{QRPN}} \tag{1.25}$$

Following Eq 1.15, the equation of motion for the mirror displacement caused by the radiation pressure is:

$$\frac{d^2 l_{x,y}^{\text{QRPN}}}{dt^2} = \eta\frac{2\delta P}{Mc} \tag{1.26}$$

where $l_{x,y}^{\text{QRPN}}$ are the radiation pressure induced mirror motions in x and y arms, $\eta = \pm$ for y and x arms, respectively. The source of intensity fluctuations in laser field reflected from x and y mirrors (δP), are the back action effects of the mirror motion due to the vacuum fluctuations that enter through the dark port of the interferometer.

Following Eq 1.21. to solve for the intensity fluctuations in frequency domain, we obtain the amplitude of the back-action induced mirror motion.

$$l_{x,y}^{\text{QRPN}} = \eta\frac{2\sqrt{P_S\hbar\omega_o}}{cM\Omega^2}\hat{a}_1 \tag{1.27}$$

or the total differential displacement

$$\delta L_{\text{QRPN}} = l_y^{\text{QRPN}} - l_x^{\text{QRPN}} \Rightarrow \frac{4\sqrt{P_S\hbar\omega_o}}{cM\Omega^2}\hat{a}_1 \tag{1.28}$$

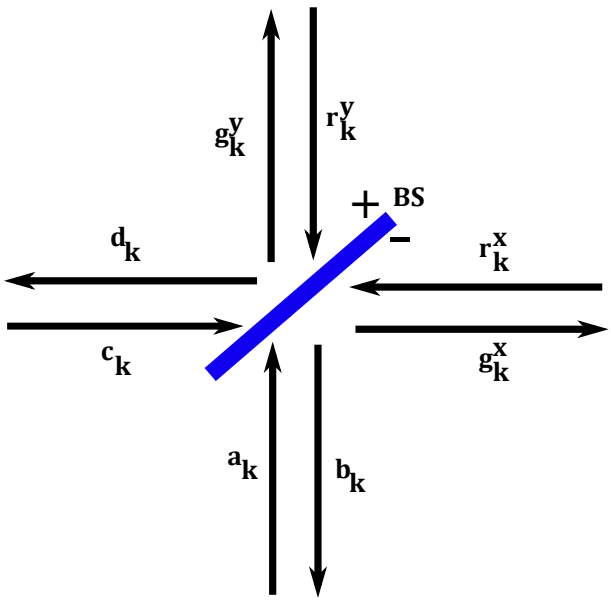

Figure 1.5: The schematic representing the input-output field operators at the beamsplitter. The Asymmetric side of the beam splitter is by convention represented by a negative sign owing to the field amplitudes being subtracted at the asymmetric output.

Assuming a Michelson interferometer with a perfectly reflective end test masses. The input-output relation as shown in Fig 1.5, suggest that the field quadratures after being reflected from the end mirrors will contain a phase shifted component due to the back action of the motion of test masses.

Since the back action effects of the mirror motion are encoded onto the phase quadrature of the reflected field. Therefore, the output amplitude quadrature at the asymmetric port should be unchanged except for picking up a normalized phase. Hence,

$$\hat{b}_1 = \frac{\hat{r}_1^y - \hat{r}_1^y}{\sqrt{2}} \Rightarrow \hat{a}_1 \tag{1.29}$$

The phase quadrature of the reflected field picks up a phase shifted sideband due to the backaction of the mirror motion induced by the gravitational wave and the radiation pressure noise.

$$\delta\hat{r}_2^{x,y} = \hat{g}_2^{x,y} - \sqrt{\frac{I_o}{\hbar\omega_o}}\frac{2\omega_o}{c}(\Delta L)$$

$$\Rightarrow \frac{\hat{c}_2 + \eta\hat{a}_2}{\sqrt{2}} - \sqrt{\frac{I_o}{2\hbar\omega_o}}\frac{2\omega_o}{c}(Lh + \delta l_{x,y}^{\mathrm{QRPN}}) \tag{1.30}$$

The output field at the asymmetric port is

$$\hat{b}_2 = \frac{\hat{r}_2^y - \hat{r}_2^x}{\sqrt{2}} \Rightarrow \hat{a}_2 - \sqrt{\frac{I_o}{\hbar\omega_o}}\frac{\omega_o}{c}(L\tilde{h} + \delta L_{\mathrm{QRPN}}) \tag{1.31}$$

Substituting the value of δL_{QRPN} from Eq 4.5

$$\hat{b}_2 = \hat{a}_2 - \mathcal{K}\hat{a}_1 - \sqrt{\frac{P_S\omega_0}{\hbar c^2}}L\tilde{h} \tag{1.32}$$

Here

$$\mathcal{K} = \frac{4P_s\omega_o}{c^2 M_r \Omega^2} \tag{1.33}$$

where $\mathcal{K}$ is the radiation pressure coupling coefficient. M is the reduced mass of the test mass in each arm of the interferometer, hence $M_r = M/2$ for an extended Michelson with two test masses in a Fabry Perot cavity. The classical noise components, assuming efficient filtering at the optical readout, are ignored in the above expression for the phase quadrature ($\hat{b}_2$) of the output field at the asymmetric port.

The above Eqs 1.31. and 1.32. tells us that for a vacuum state with an equal uncertainty in the two quadratures of the input field, the uncertainty in the output state quadratures is squeezed or anti-squeezed due to the imprinted backaction effects of the mirror motion. This parametric amplification of the output optical field quadratures is called the ponderomotive squeezing [34, 40, 41, 42].

At the most sensitive frequency spectrum around 100 Hz, the design sensitivity of Advanced LIGO is limited by the Brownian motion of the reflective coating molecules of the test masses. The enhanced thermal noise due to higher laser power along with some factor of contributions due to the thermal lensing, is relaxed by increasing the diameter of the beam at the test masses. Additionally, the compensation plates are used to cancel the

technical noises due to the distortion of the mirrors by thermal lensing.

Hence, the total phase noise budget of Advanced LIGO is limited by a combination of thermal noise of the suspensions, the Brownian noise of the reflective coating, the shot noise or the photon counting error, and the radiation pressure induced noise. Fig 1.6 shows the measured noise during the O1 run of Advanced LIGO at Livingston, LA [4]. The total circulating power in each arm cavity, during the O1 run, was about 100 kW. The figure further depicts the limiting noise sources predicted to contribute to the overall noise floor at the design sensitivity of Advanced LIGO.

In Advanced LIGO, at the design sensitivity Fig 1.6, the quantum radiation pressure noise is projected to be the dominant noise source at detection bandwidth between 10 Hz and 100 Hz. Below 10 Hz, the suspension thermal noise is dominant and governs the bound to the sensitivity gain by reducing the quantum noise floor. Advanced LIGO is upgraded to have an input laser power of about 200 Watts at the beamsplitter with about 750 kW of circulating power in each arm cavity. Higher laser power is used to enhance shot noise limited sensitivity floor at higher frequencies (above 100 Hz) of detection bandwidth. Substantially heavier test masses of Advanced LIGO (about 40 kgs), in comparison to the test masses of the initial LIGO (about 11 kgs), are used to compensate for the increase in the quantum radiation pressure noise contributions at higher input laser power.

The optimal interferometer bandwidth for Advanced LIGO lies in the GWs from the inspiral neutron stars and binary black hole systems. This optimization along with the low frequency noise contributions from the above mentioned factors are taken into consideration for the detector's half bandwidth, given by.

$$\gamma = \frac{Tc}{4L} \tag{1.34}$$

where T is the transmission of corner test masses.

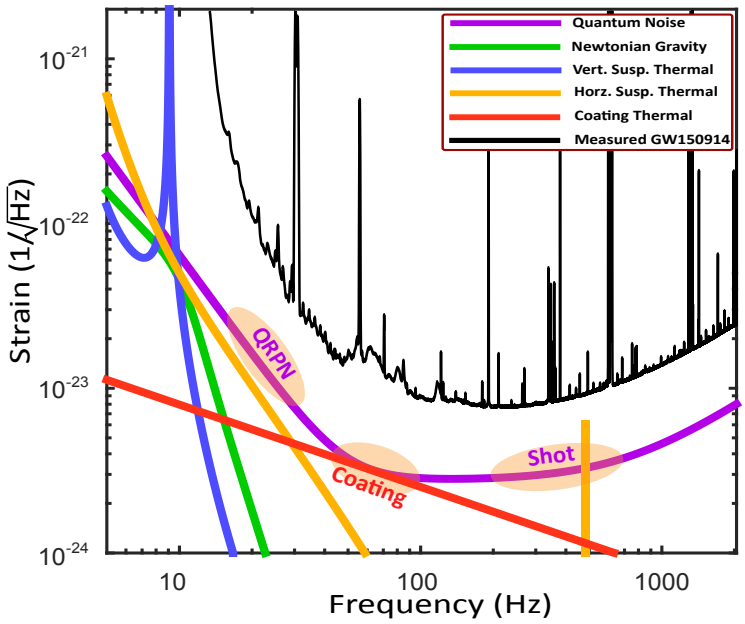

Figure 1.6: Noise plot of Advanced LIGO showing the measured noise sensitivity during the O1 run, and the projected limiting noise sources at the full design sensitivity of Advanced LIGO.

1.4 Noise Evasion Schemes for Advanced LIGO

The total phase noise budget of Advanced LIGO is limited by a combination of thermal noise of the suspensions, the Brownian noise of the reflective coating, the shot noise or the photon-counting error, and the radiation pressure induced noise. The shot noise and the QRPN are orthogonally correlated in quadrature and frequency dependence. Hence the conventional use of nonclassical or squeezed light is not advantageous as such. In order to efficiently enhance the sensitivity at the overall detection bandwidth of Advanced LIGO, modified noise evasion techniques needs to be devised and tested. Many frequency dependent noise evasion schemes that include the variational readout, frequency dependent squeezing, and speedmeter design for the QND detection, have been proposed to relax the QRPN and the shot noise limited bound on the sensitivity of Advanced LIGO. Although extensively studied, a tabletop experimental investigations to quantitatively calibrate the gain in sensitivity through these schemes is necessary to ascertain the efficiency of these schemes before their application to the next generations of the GW detectors.

The primary goal of my thesis project is to establish an experimental setup for the measurement of the quantum radiation pressure noise in an optomechanical cavity. Once QRPN is measured, the setup can be used for the prototype testing of the various quantum noise evasion schemes. Here I will briefly overview the two main noise evasion schemes for their applicability in the next generation of gravitational wave detectors.

A free mass respond in the frequency domain with a mechanical susceptibility $\mathcal{X}_{xx}(\omega) = -1/M\Omega^2$. As derived by Braginsky [43, 44], for a continuous position measurement system, the minimum uncertainty in the second position measurement is given as

$$(\Delta x)_{\mathrm{SQL}} = \frac{2\hbar}{M\Omega} \tag{1.35}$$

This uncertainty in the future position measurements at the , dictates the standard quantum limit in the strain sensitivity of the detected field in an interferometric measurement.

$$h_{\mathrm{SQL}} = \sqrt{S^h_{\mathrm{SQL}}} \Rightarrow \sqrt{\frac{4\hbar}{M_r\Omega^2 L^2}} \tag{1.36}$$

The shot noise due to the photon number fluctuations and the radiation pressure noise due to the fluctuating force are the dominant sources of noise in Advanced LIGO. The total noise spectral density for the strain sensitivity of Advanced LIGO is hence given as the sum of the noise spectra due to the shot noise and the QRPN.

$$S_h = S^h_{\mathrm{shot}} + S^h_{\mathrm{QRPN}} \tag{1.37}$$

The uncertainty in the output phase quadrature due to the shot noise is governed by the root mean square fluctuations in the number of photons ($\sqrt{N}$). Therefore, for the gravitational waves of frequency f, the shot noise and the QRPN spectral densities are

given respectively as:

$$S^h_{\rm shot} = \left|\frac{\delta\phi_{\rm shot}}{L}\right|^2 \approx \frac{\hbar c^2}{P_S\omega_o}, \qquad \text{and} \qquad S^h_{\rm QRPN} = \left|\frac{F_{\rm QRPN}}{M\Omega^2}\right|^2 \approx \frac{P_S\omega_o\hbar}{c^2M_r^2\Omega^4} \tag{1.38}$$

Hence the spectral density and the corresponding strain sensitivity can be written in terms of the standard quantum limit and the radiation pressure coupling constant:

$$S_h = \frac{\hbar c^2}{P_S\omega_o} + \frac{\hbar P_S\omega_o}{c^2M_r^2\Omega^4} = \left(\frac{1}{\mathcal{K}} + \mathcal{K}\right)\frac{h^2_{\rm SQL}}{2} \tag{1.39}$$

The above Eq 1.39. for the spectral density of the measured strain can be rewritten in terms of the output phase quadrature such that,

$$S_h = \frac{h^2_{\rm SQL}}{2}(\Delta b_2)^2, \qquad \text{where} \qquad \Delta b_2 = a_2 - \mathcal{K}a_1. \tag{1.40}$$

1.4.1 Variational Output Interferometer or Frequency Dependent Homodyne Detection

Originally formulated by Vyatchanin, Matsko and Zubova [45, 46, 47], variational output readout is essentially a Quantum Non-Demolition (QND) technique where a frequency dependent homodyne detection is performed at the asymmetric output of the interferometer. In contract to the conventional balanced homodyne readout, where the local oscillator fix the phase (Φ) of detection to the suitable quadrature, the variational output readout homodyne phase ($\xi(\Omega)$) follows the frequency varying quadrature of the output field. In other words, and optimal measurement for the evasion of QRPN can be made at frequency dependent quadrature readout as a combination of the output quadratures [34].

$$\hat{b}_\xi(\Omega) = \hat{b}_1{\rm cos}\xi(\Omega) + \hat{b}_2{\rm sin}\xi(\Omega) \Rightarrow {\rm sin}\xi(\Omega)\left(\hat{a}_1{\rm cot}\xi(\Omega) + \hat{a}_2 - \mathcal{K}\hat{a}_1 + \sqrt{2\mathcal{K}}\frac{h}{h_{\rm SQL}}\right) \tag{1.41}$$

QRPN limited backaction noise in the output readout is due to the vacuum fluctuations

entering the amplitude quadrature (a_1), at the dark port of the interferometer. As is evident from the above equation, the contribution due to the QRPN limited component, in the output measurement, can in principle be removed by following the homodyne phase $\xi(\Omega) = \text{arccot}\mathcal{K}$.

Such a frequency dependence in the proposed variational output readout scheme, is achieved by filtering the output light field through two detuned Fabry-Perot cavities. The filter cavities essentially put a tunable phase shift $\alpha_{\pm}$ onto the light with respective sidebands $\omega_o \pm \Omega$. The phase shifted output light from the filter cavity is then monitored by the conventional balanced homodyne detection such that overall homodyne phase is

$$\Phi - \frac{(\alpha_+ + \alpha_-)}{2} = \xi(\Omega) \tag{1.42}$$

The two detuned filter cavities at the signal recycled dark port output are that are red and blue detuned, respectively to obtain the desired tunability in the homodyne phase matched with the output of the detuned SRM cavity. The optical losses pose as the main limitation to the desired bandwidth and the sensitivity of these filter cavities. These losses are minimized in the proposed scheme by making the cavities very long. Although, there have been Electromagnetically Induced Transparency (EIT) and Optomechanically Induced Transparency (OMIT) based counterparts for the narrow linewidth filter cavities, but such schemes are not applicable to Advanced LIGO. This is either due to the absence of the known atomic system with transition wavelength of the order of 1 micron, or the huge coupling losses in the OMIT systems.

1.4.2 Frequency Dependent Squeezed Input

According to the laws of quantum mechanics, Heisenberg uncertainty principle put a bound on the the precision in the measurement of the dynamics of a system interacting with the optical field. This bound is dictates the minimum uncertainty or noise in the complex amplitudes of the optical field. Such uncertainty is normally symmetric in the

two quadratures of a vacuum state or a displaced vacuum (coherent) state of light. Such a symmetric distribution of uncertainty however, can be experimentally modified to minimize the noise in one quadrature at the expense of increase the noise in the orthogonal. The state of light with minimized noise in one quadrature is called a squeezed-state light. In principle, if a balanced homodyne measurement is made sensitive to the quadrature with minimum noise, the enhancement in the sensitivity in measurement of the optical system can be gained. Since the pioneering work towards generating squeezed states in 1980s [48, 49], the improvements in the techniques for the generation of robust squeezed states with lower noise floors have been demonstrated and exploited as an in-expendable tool by a vast scientific community [50, 51].

In Advanced LIGO however, an improvement in the overall enhancement in the design sensitivity require a squeezed input with a varying squeeze angle $\lambda(\Omega)$ that is dependent on the frequency (Ω) of the detection band. Originally devised by Unruh and explained by Kimble et. al. [34], the proposed FD squeezed-state input at the asymmetric port of Advanced LIGO is expected to surpass the SQL sensitivity. The input state at the dark port of the interferometer can be viewed as a squeeze operator ($\hat{\mathrm{S}}(\mathrm{z})$) applied onto the input vacuum state.

$$|a\rangle = \hat{S}(z)|0\rangle \tag{1.43}$$

where for frequency dependent squeezing angle ($\theta(\Omega)$) and $z = re^{i\theta(\Omega)}$, the squeeze operator in two photon formalism is given as:

$$\hat{S}(z) = \exp(re^{-i\theta}\hat{a}^2 + re^{i\theta}\hat{a}^{\dagger 2}) \tag{1.44}$$

As mentioned in [34] and shown in Fig 1.7, at a squeeze angle of $\theta(\Omega)$ given as:

$$\theta(\Omega) = -\mathrm{arccot}(\mathcal{K}) \tag{1.45}$$

the sensitivity at the overall detection bandwidth of the interferometer is improved by a factor of e^{-2R}. In other words, the spectral density $S_{h(SQ)}$ of the FD squeezed input interferometer get reduction in the noise floor as given below.

$$S_{h(SQ)} = S_h \times e^{-2r} \tag{1.46}$$

where S_h is given by Eq 1.39.

1.4.3 Squeezed-Input Variational Output Interferometer

The frequency dependence to the squeeze angle is achieved in a similar fashion as in variational output interferometer, by sending the generated squeezed state through filter cavities.

To obtain a maximum gain in the sensitivity floor, especially at the lower frequencies of the detection bandwidth of Advanced LIGO, the upgrade with a combination of a squeezed-state input and a variational output optical readout is required. In this scheme a squeezed-state input reduce the overall noise in the output spectral density at the asymmetric port of Advanced LIGO. This reduced noise signal is further subjected to a frequency dependent homodyne detection for the rejection of the QRPN dependent back-action noise in the output signal.

The spectral density of the the interferometer strain signal hence becomes

$$S_h = e^{-2r} \times S_{h(\mathrm{var})} = e^{-2r} \frac{h^2_{\mathrm{SQL}}}{2\mathcal{K}} \tag{1.47}$$

1.5 Overview

In this chapter, I have outlined the concept and the design sensitivity of Advanced LIGO along with the proposed changes to further enhance the sensitivity of Advanced LIGO. I have also laid foundational description to explain the limiting fundamental noise sources in both classical and quantum regime for Advanced LIGO. In the last section of

this chapter I briefly described the physics behind the various exploitable techniques that can be used for the mitigation of quantum noise in the future avatars of the GW detectors. The schematic for the overall improvement in the strain sensitivity of a GW interferometer, by the quantum noise evasion techniques discussed earlier is shown in the Fig 1.7.

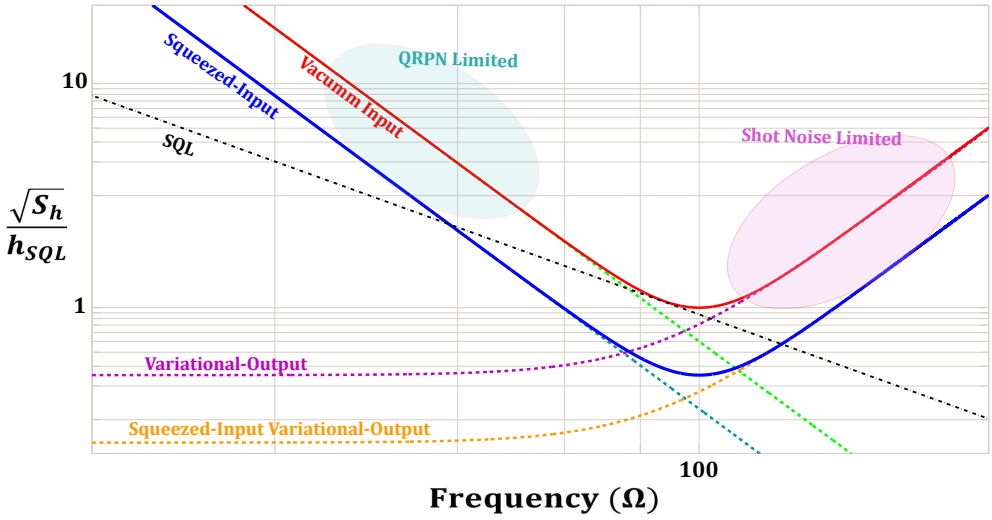

Figure 1.7: The schematic (not to scale) showing the improvement in the strain sensitivity of a GW interferometer, with the application of various noise evasion schemes. The strain sensitivity on y axis is normalized to the SQL strain at the optimal frequency of the interferometer.

The proposed noise evasion schemes are the motivation for my experimental thesis work, discussed in the later chapters. The measurement of the quantum radiation pressure noise (QRPN) has posed a major challenge to the scientific community, either as an outcome of being masked by the other noise sources or being partially insensitive in the measurement quadrature. Although being recently measured in the on-resonance experimental setups, the broadband effects of the QRPN has still been elusive. The measurement of the QRPN in a broad detection bandwidth is important in particular to the GW community to further demonstrate the effectiveness of the various noise evasion techniques proposed for Advanced LIGO. Further since the quantum radiation pressure noise causes correlated parametric amplification of the output light field, this effect can be utilize to demonstrate the ponderomotive generation of the squeezed state of light as a pure optomechanical

effect. It is also of particular interest to the physicist to study the quantum mechanics of a macroscopic resonator and hence infer the entangled state in a dissipative optomechanical system. All this is possible only after an effective measurement of the quantum radiation pressure noise.

In the next chapter, I will discuss the fundamentals of the optomechancial coupling in an effort to lay foundation towards the effective manipulation of the artifacts of correlations between the mechanical oscillator and the optical cavity that are exploited in the experimental setup for the measurement of the QRPN.

Chapter 2
Cavity Optomechanics with a Microresonator

2.1 Introduction

The dual wave-particle nature of the light has long been explored and exploited by the scientific community. Such exploitations had lead to pioneering work on optical trapping of the atoms for the cooling to their motional ground states [52, 53, 54]. These frontier experiments laid foundations towards the quest to study effects of momentum driven radiation pressure of the photons onto the macroscopic harmonic oscillators. Further lead by the earlier investigations of Braginsky et. al. [44, 55], about the effects of radiation pressure on the dynamics of the suspended test mass in an interferometer, the framework of optomechanical cavity based interferometer experiments that include the GW detectors, was established.

In addition to the development of highly reflective and low loss optical mirrors, the advancements in the field of nano- and micro-fabrication has lead the field of non-linear optomechanical spectroscopy towards exploring the non-dissipative effects of the radiation pressure force. In order to effectively extract the information about mechanical state in an optomechanical coupling regime, the decoherence time for the prepared optomechanical state should be relatively large.

Hence the race towards cooling of these macroscopic resonators to the quantum ground state has one hand gained a new momentum due to the potential applications in the hybrid quantum systems. On the other hand such systems are limited to measurements around the cavity resonance at high frequencies, and hence lack the information about the broadband dynamics of the optomechanical system, in frequency space. Further to reduce the intrinsic thermal noise of test resonator, the mechanical Q and the eigenfrequency of such resonators are desired to be as high as possible. Building such high frequency resonators suffer

serious technical challenges due to dissipation losses from the noisy environment, hence these systems either mostly require intensive application of cryogenics.

The low frequency broadband mechanical oscillator system in addition to being used at large scale in the GW detectors, also pose as valuable candidate for the tabletop demonstration of the linear and the nonlinear dynamics of the optomechanical cavity. Such experiments have already lead to realization of the stable optical traps, and cooling of a suspended gram scale mechanical resonator [56, 57, 58].

In addition to the optical losses, the experimental realization of such robust optomechanical systems are bound by various thermo-elastic dissipative forces acting on the mechanical resonator. To isolate the mechanical motion from such losses, various suspension techniques for the macroscopic mirrors have been proposed. Typically by exploiting the gravitational dilution discussed in Chapter 1, such suspensions are made very soft to minimize the coupling between the mechanical oscillator and the noisy environment. The soft spring mechanical oscillators on the flip side can be very floppy and excessively responsive to the ambient fluctuating forces, thus requiring intensive isolation at low frequencies. As will be discussed in detail in further sections, it has been previously demonstrated that the effective response of such soft springs can be made stiff as an outcome of optomechanical interactions [57]. Hence such a low frequency mechanical oscillator based optomechanics offer effective isolation from the ambient noise in addition to the dilution of the source of thermal decoherence.

As a part of my thesis, I have built an optomechanical experiment based on the dynamics of a Fabry-Perot cavity with a movable end mirror. The end mirror of the one centimeter long linear cavity is a microresonator mirror fabricated in collaboration with Dr. Garrett Cole from the Crystalline Mirror Solutions [28, 29]. The chip containing the fabricated microresonator test mirrors is shown in Fig 2.1. The goal of the experiment is to directly measure the broadband effects of the quantum radiation pressure noise due to the fluctuations in the instantaneous number of photons hitting the microresonator mirror.

The experimental effort involve isolating the mechanical system from ambient noises and further reducing the thermal fluctuations due to the viscous damping and the structural dynamics of the fabricated supports. The details of the experiment are mentioned in the next chapter.

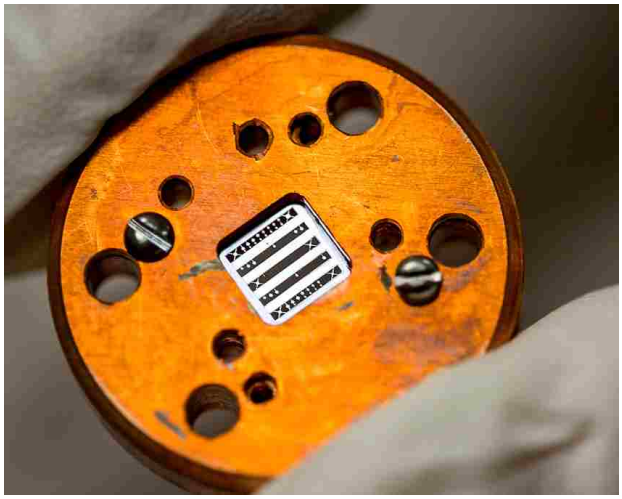

Figure 2.1: Image of the chip containing the microresonator mirror masses used in the experimental effort to measure the QRPN.

In this chapter I will review the fundamentals of the optomechanical system with a suspended test mass to describe the dynamical sources of decoherence, and define the control parameters in the interaction picture. Further I will build up the theory to show the usefulness of the effects like optical spring, optical dilution as an artifact of optical spring, and the evasion of backaction noise due to feedback cooling.

2.1.1 Optical Resonator

In a simple highly reflective Fabry-Perot resonator cavity, the optical losses are generally the key source of decoherence. For a given length L of the optical resonator, the roundtrip power losses (P_{loss}) due to scattering, internal absorption and the finite transmission of the cavity optics, govern the response (linewidth) of the cavity towards the small frequency shifts in the resonant optical modes, given as [59]

$$\delta\omega_c \propto \frac{\pi^2 c^2}{L^2 \mathcal{F} \sqrt{P_c}} \tag{2.1}$$

where P_c is the circulating power inside the cavity. For cavity mode of angular frequency $\omega_c = \pi c/L$, finesse in terms of the cavity losses is given as:

$$\mathcal{F} \approx \frac{2\pi}{P_{\text{loss}}} \tag{2.2}$$

To be noted here that the an optical resonator of finite length (L) contains an integer (k) number of optical resonance modes (ω_c^k) separated in longitudinal frequency domain by the free spectral range (FSR).

$$\Delta\omega_{\text{fsr}} = \frac{\pi c}{L} \tag{2.3}$$

An optical field driven Fabry Perot cavity is generally operated close resonance to a single cavity mode ω_c through one or a combination of control sequences that include reference cavities, proportional feedback for the length control of the cavity, etc. A single resonant mode cavity is valid under the assumptions that:

1) The finesse of the optical cavity is relatively high with minimum losses due to transmission through the optical end mirrors.

2) The free spectral range of the cavity is much larger than the length of the cavity.

3) Detuning δ of the pump laser field from the cavity resonance ω_c is much smaller than the FSR.

In terms of the cavity decay rate κ_c or the inverse of photon lifetime τ inside the cavity.

$$\kappa_c = \frac{1}{\tau} \Rightarrow \frac{cP_{\text{loss}}}{2L} \tag{2.4}$$

The finesse of the cavity can be redefined as:

$$\mathcal{F} = \frac{\Delta\omega_{\text{fsr}}}{\kappa_c} \tag{2.5}$$

The finesse of the optical resonator can be seen as an analog of a quality factor of

the mechanical oscillator. Whereas the mechanical quality factor (Q_m) is a measure of the number of harmonic oscillations of the resonator, the finesse is the measure of the number of round trips that a resonant photon can make before escaping the optical cavity.

2.1.2 Mechanical Resonator

The high sensitivity measurement for the effects of photon induced momentum onto the massive particles can in principle be experimentally achieved by using a movable resonator test mass as one of the mirror in an optical cavity. The resonant optical cavity usually filter out most of ambient vibrational modes of the oscillator associated with the noisy environment. The mass of the resonator is generally orders of magnitude smaller than the input fixed mirror, so that effective dynamics of the optomechanical system is only dependent on the mass of the movable mirror. The Fig 2.2 below shows the schematic of the dynamics of the optomechanical cavity with a movable test mass.

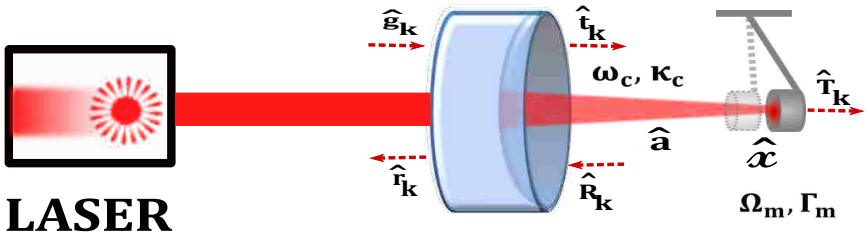

Figure 2.2: A cartoon showing an optomechanical cavity in a hemispherical configuration. The output mirror is a suspended low mass resonator. For input optical mode represented by the quadrature operators $\hat{t}_k$, the modes associated with the reflection and transmission of the input coupler mirror are represented as $\hat{r}_k$ and $\hat{t}_k$, respectively. $\hat{R}_k$ and $\hat{T}_k$ are the quadrature operators associated with the reflection and the transmission of the resonator test mass. For a resonant cavity frequency ω_c, $\hat{a}$ is the cavity operator, and κ_c is the cavity decay rate. $\hat{x}$is the eigen vibrational mode for the mechanical resonator.

Under the boundary conditions provided by the theory of elasticity and assuming the lowest eigenmode of vibration (Ω_m) for the mechanical oscillator, the dynamics of the associated test mass is governed by the equation of motion for a damped oscillator under

the total external force $F_{ext}(t)$

$$M\ddot{x}(t) = -k_m x(t) - M\Gamma_m \dot{x}(t) + F_{ext}(t) \tag{2.6}$$

where Γ_m is the mechanical damping rate, M is reduced mass, and $k_m = m\Omega_m^2$ is the mechanical spring constant. The Fourier transform of the above equation can be solved for the mechanical susceptibility or the transfer function of the mechanical resonator in frequency domain.

$$G(\Omega) = \frac{\delta x(\Omega)}{F_{\text{ext}}(\Omega)} = \frac{1}{M(\Omega_m^2 - \Omega^2) - iM\Gamma_m\Omega} \tag{2.7}$$

It is worth noting that the mechanical response at any given time include the contributions due to the random influence of the dissipative Brownian force and the mechanical damping. The Fourier transform, on the contrary, gives the response of the mechanical resonator separated in frequency space and hence can be analyzed to infer the correlation of the known frequency dependent forces. At thermal equilibrium, the frequency dependent displacement noise in the mechanical resonator can hence be derived by applying fluctuation dissipation theorem (FDT) onto the auto-correlated spectral response [55].

$$x(\Omega) = \sqrt{\frac{k_B T}{\Omega_m} \text{Im}(G(\Omega))} \tag{2.8}$$

2.2 Optomechanical Coupling

2.2.1 Hamiltonian Formulation

As previously mentioned in a pioneering work by Aspelmeyer [55], the Hamiltonian for an single resonant mode optomechanical system can be represented in analogy to the Jaynes Cumming model for the atom field interactions. The dynamics can be approximated in a time independent Hamiltonian under the rotating wave approximation of the driving laser field, as two coupled harmonic oscillators representing the optical cavity mode and

the mechanical oscillator.

$$\hat{H} = \hat{H}_{\text{field}} + \hat{H}_{\text{cav}} + \hat{H}_{\text{mech}} + \hat{H}_{\text{int}} + \hat{H}_{\text{diss}} \tag{2.9}$$

where $\hat{H}_{\text{cav}}$ and $\hat{H}_{\text{mech}}$ are the uncoupled contributions to the total Hamiltonian by the optical cavity and the mechanical oscillator, respectively. $\hat{H}_{\text{field}} \approx -\hbar\omega_L \hat{a}^\dagger \hat{a}$ is the contribution due to the the driving laser, and $\hat{H}_{\text{diss}}$ include the dissipative terms due to the optical losses, thermal and mechanical decoherence. For a closed interaction system we can ignore any dissipative terms.

The second quantization of the harmonic oscillator, optical field and the mechanical oscillator are represented in terms of their respective Hamiltonian as. As per many body formalism, the optical and the mechanical oscillators can be represented in terms of their respective ladder operators as:

$$\hat{H}_{\text{cav}} = \hbar\omega_c \left(\hat{a}^\dagger \hat{a} + \tfrac{1}{2} \right), \tag{2.10}$$

$$\hat{H}_{\text{mech}} = \frac{\hat{p}^2}{2M} + \frac{1}{2} M \Omega_m \hat{x}^2 = \hbar\omega_c \left(\hat{\tilde{x}}^\dagger \hat{\tilde{x}} + \tfrac{1}{2} \right), \tag{2.11}$$

where the position $\hat{x}$ and the momentum $\hat{p}$ operators given in term of the ladder operators $\hat{\tilde{x}},\ \hat{\tilde{x}}^\dagger$ as:

$$\hat{x} = \sqrt{\frac{\hbar}{2m\Omega_m}} (\hat{\tilde{x}}^\dagger + \hat{\tilde{x}}); \qquad \text{and} \qquad \hat{p} = i\sqrt{\frac{\hbar m \Omega_m}{2}} (\hat{\tilde{x}}^\dagger - \hat{\tilde{x}}) \tag{2.12}$$

The interaction term in the Hamiltonian essentially carry the information about the parametric modulations of the cavity resonance due to the mechanical oscillations of the movable mirror. To a linearized approximation, such modulations can be represented as

displacement amplitude-dependent frequency shifts.

$$\hat{H}_{\text{int}} = \hbar\hat{x}\frac{\partial\omega_c}{\partial x}\hat{a}^\dagger\hat{a} = -\hbar g_o\hat{a}^\dagger\hat{a}(\hat{\tilde{x}}^\dagger + \hat{\tilde{x}}), \tag{2.13}$$

where g_o is the single photon coupling constant. While ignoring the contributions due to the dynamical Casimir effects, the total Hamiltonian can be represented as

$$\hat{H} \approx \hbar[\Omega_m\hat{x}^\dagger\hat{x} - \Delta\hat{a}^\dagger\hat{a} - g_o\hat{a}^\dagger\hat{a}(\hat{\tilde{x}}^\dagger + \hat{\tilde{x}})], \tag{2.14}$$

where $\Delta = \omega_L - \omega_c$ is the detuning of the laser field from the cavity resonance frequency.

Further the cavity field constitute of the coherent amplitude and the fluctuations in the amplitude. These fluctuations are the source of the radiation pressure noise in an optomechanical system. Under linear regime, the amplitude fluctuations are:

$$\delta\hat{a} = \hat{a} - \langle\hat{a}\rangle \rightarrow \hat{a} - \alpha, \tag{2.15}$$

where $|\alpha\rangle$ is the coherent eigenstate of the annihilation operator $\hat{a}$. Therefore the interaction Hamiltonian can be written as:

$$\hat{H}_{int} = -\hbar g_o\sqrt{n_c}\Big[\mid\alpha\mid^2 + (\alpha^*\delta\hat{a} + \delta\hat{a}^\dagger\alpha) + \delta\hat{a}^\dagger\delta\hat{a}\Big](\hat{\tilde{x}}^\dagger + \hat{\tilde{x}}), \tag{2.16}$$

where $\sqrt{\overline{n_c}} = \left\langle\hat{a}^\dagger\hat{a}\right\rangle$ to be the average number of photons circulating in the resonant cavity mode.

Here the first term is a contribution due to the average radiation pressure force of the coherent field inside the cavity and can be modified in an experiment by selecting the appropriate detuning of the laser field along with the feedback control loops. The second term represent the dominant contributing dynamics due to the fluctuations in the intensity of the driven cavity field and is the source of various optomechanical dynamics including the

back-acting radiation pressure noise. The schematic of these optomechanical interactions between the driven optical cavity and the mechanical resonator is shown in the Fig 2.3 below. In a stable cavity regime, assuming minimum acoustic decoherence, the movable test mass can be excited either by the radiation pressure force or the thermal excitations ($\bar{n}_{\rm th}$) due to the coupling to the noisy environment.

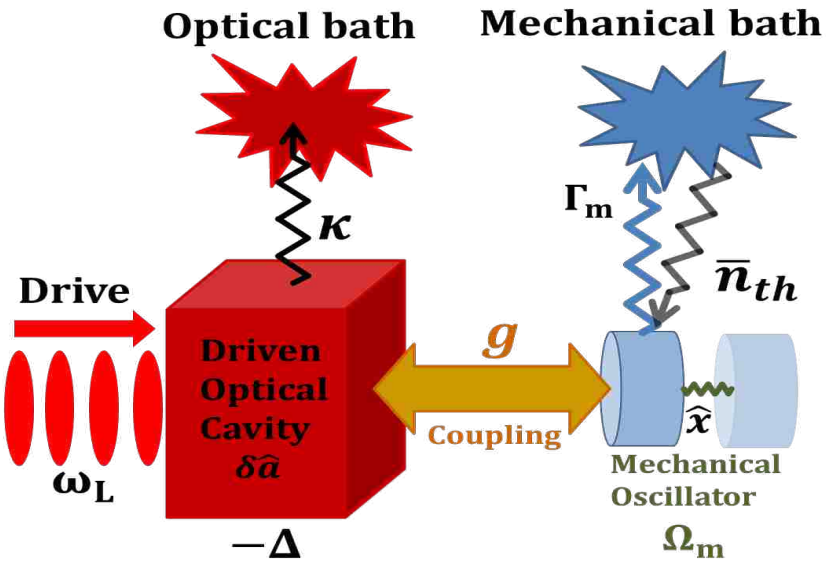

Figure 2.3: A schematic description of the optomechanical coupling parameters between the driven optical cavity and movable mirror that oscillate under the radiation pressure force. $\bar{n}_{th}$ are the thermal phonons responsible for the thermal decoherence.

Many other non-trivial artifacts of optomechanical interactions can be observed in primarily two main coupling regime. In a sideband resolved regime, where the cavity decay rate is much smaller than the mechanical frequency of the oscillator, the mechanical oscillator can be cooled to its vibrational ground state. This cooling of the oscillator is possible by red detuning the laser field at around mechanical frequency. The cooling occur due to the transfer of thermal phonons into the cold reservoir of the photon modes. Here the transition taking the oscillator from the higher quanta to the lower quanta can be understood as an effect of $(\delta\hat{a}^{\dagger}\hat{\tilde{x}} + \delta\hat{a}\hat{\tilde{x}}^{\dagger})$.

Similarly when the cavity is blue detuned, parametric amplifications of the reflected optical mode can be achieved. These effects are understood in part to be the outcome of

strong quantum correlations between the mechanical vibrational and the resonant optical modes. These effects are the source of quantum radiation pressure noise and can in principle be exploited to ponderomotively generate the squeezed states of light.

The dynamical effects of optomechanical can further be understood from the quantum Langevin equations as derived in [55]. The evolution of the optical mode and the mechanical mode as an artifact of backaction effects of each other can be seen in terms

$$\dot{\hat{a}} \rightarrow i(\Delta + \frac{g_o}{x_o}\hat{x})\hat{a}, \qquad and \qquad \dot{\hat{\hat{x}}} \rightarrow -i\Omega_m\hat{\hat{x}} + ig_o\hat{a}^\dagger\hat{a} \tag{2.17}$$

Here, I have ignored uncoupled dissipation of each mode along with the dissipation of the optical field due to the mechanical damping rate Γ_m.

2.2.2 Dynamical Backaction: Optical Spring Effect

It is worth mentioning that in order to expose the quantum mechanics of the optomechanical interactions, the classical dynamical effects serve as inexpendable tools, in particular, to manipulate the dynamics of the mechanical oscillator. These effects primarily originate from the fact that the mirror motion shifts the detuning of the optical cavity, hence the power circulating and the effective radiation pressure force is dependent on the motion of the test mass.

For simplicity, if we assume a cavity with a delta-function-narrow linewidth, the cavity response and hence the circulating power will shift instantaneously due to the mirror motion. The resulting radiation pressure force can be given as:

$$F_{\mathrm{RP}}(x) = -\frac{\partial V_{\mathrm{RP}}}{\partial x} = \hbar\frac{\partial \omega_c}{\partial x}\bar{n}_c(x), \tag{2.18}$$

where the fluctuating number of photons circulating in the resonant mode of the optical cavity can be described in terms of the total number of photons available in the optical

mode ($\bar{n}_c$) as:

$$\bar{n}_c(x) = \frac{\bar{n}_c}{1 + 2(\frac{\partial \omega_c}{\partial x}x + \Delta)/\kappa} \tag{2.19}$$

Hence for an oscillator mirror, the effective back and forth shifts in the radiation potential will drive the optomechanical system. The effective spring constant of the optomechanical system shifts as $\partial^2 V_{RP}/\partial x^2$. For a low mechanical frequency oscillator the shift in the mechanical frequency of the oscillator can be approximated to be,

$$\Omega_{\text{eff}} \approx 8\Delta \Big\{ \frac{g_o}{\kappa} \Big\}^2 \frac{\bar{n}_c}{\Big\{1 + (\frac{2\Delta}{\kappa})^2\Big\}}. \tag{2.20}$$

To fully understand the above dynamics of the optomechanical response, the fact that the optical cavity has a finite linewidth should be taken into account. This finite optical response of the cavity lead to a delay between the mechanical motion and the resulting change in the radiation pressure force. This delayed response of the detuned optical cavity lead to the dynamical effects of the radiation pressure force. Such effects can be represented in the mechanical susceptibility or the transfer function as a weak force acting on the mechanical oscillator.

$$G^{-1}_{\text{opt}}(\Omega) = (M(\Omega_m^2 - \Omega^2) - iM\Gamma_m\Omega) + M\Omega(2\Omega_{\text{eff}}(\Omega) - i\Gamma_{\text{opt}}(\Omega)) \tag{2.21}$$

where the real and imaginary parts of the susceptibility yield the effective shift in the mechanical frequency and the optomechanical damping rate.

$$\Omega_{\text{eff}} \approx g_o^2 \bar{n}_c \Bigg\{ \frac{\Delta + \Omega}{(\Delta + \Omega)^2 + \kappa^2/4} + \frac{\Delta - \Omega}{(\Delta - \Omega)^2 + \kappa^2/4} \Bigg\} \tag{2.22}$$

$$\Gamma_{\text{opt}} \approx g_o^2 \bar{n}_c \Bigg\{ \frac{\kappa}{(\Delta + \Omega)^2 + \kappa^2/4} - \frac{\kappa}{(\Delta - \Omega)^2 + \kappa^2/4} \Bigg\} \tag{2.23}$$

In a bad cavity regime, where the frequency of measurement (Ω) to be much smaller than the cavity linewidth, the above equations can be approximated as:

$$\Omega_{\text{eff}} \approx g_o^2 \bar{n}_c \left\{ \frac{2\Delta}{(\Delta)^2 + \kappa^2/4} \right\} \tag{2.24}$$

$$\Gamma_{\text{opt}} \approx g_o^2 \bar{n}_c \left\{ \frac{2\kappa}{(\Delta)^2 + \kappa^2/4} \right\} \tag{2.25}$$

Hence the effective frequency of oscillation of the mechanical oscillator driven by the detuned optical cavity can either be made soft or stiffe as a function of red or blue detuning of the optical cavity mode. In addition the driven optical cavity also provide the damping (red detuned) and antidamping (blue-detuned) forces. The dynamics of the mechanical oscillator can hence be manipulated by changing the resonance condition of the optical cavity mode.

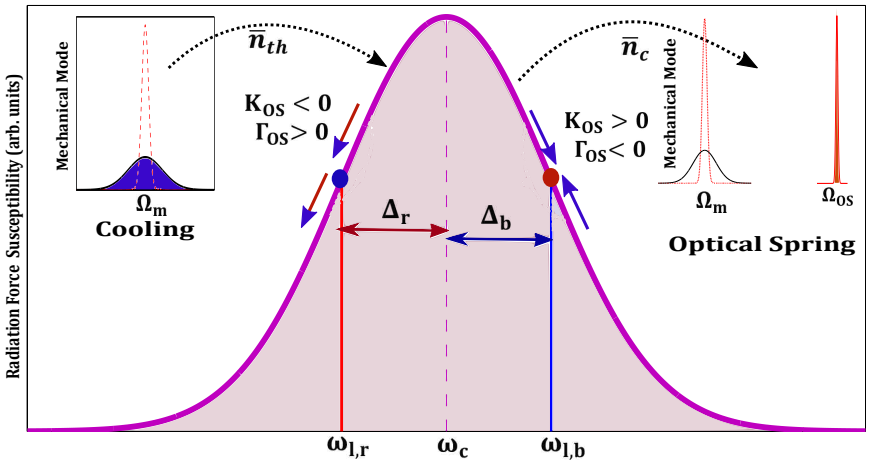

Figure 2.4: A schematic showing the effects of detuning in a driven optomechanical cavity, on the mechanical oscillator.

If the cavity is operated blue detuned to the resonance, the low eigenfrequency mechanical oscillator can be driven at much high frequency of oscillation due to the restoring force provided by the high frequency optical cavity mode. Hence, the movable mirror mass act as being attached to a very stiff spring. This effect is called the *Optical Spring* effect. Unlike the high frequency mechanical spring which couple the oscillator to the noisy environment and hence increase the thermal dissipation of the mechanical oscillator, the optical field is noiseless and does not add to the thermal dissipation.

The optical spring effect is an in-expendable tool in the field of broadband cavity optomechanics and in the large interferometers like GW detectors. The larger test masses that naturally have a lower eigenfrequency of oscillation can be effectively isolated from the excessive motion due to the low frequency acoustic and seismic vibrations, by optical spring effects. An exact derivation of the optical spring constant with notation consistent with the experimental details of Chapter 4, is given in the Appendix A of this thesis.

For a red detuned cavity the mechanical oscillator can be cooled through feedback where the oscillation optical field acts as an error signal carrying the information about the mechanical mode. Further in the sideband resolved regime, where the detuned cavity frequency oscillating with the mechanical motion can be seen in terms of asymmetric Stokes and anti-Stokes sidebands. The cooling of the mechanical oscillator can effectively be achieved by the red detuned optical cavity mode. Here the dominant anti-Stokes scattering causes the energy flowing out of the mechanical oscillator. Cold damping techniques have been proposed to trap the mechanical oscillator in its ground state. This can be explained in scattering picture where where the oscillating the net energy is taken out of the mechanical mode as a result of asymmetry in the Stokes and anti-Stokes sidebands.

2.3 Overview

In this chapter, I have build up a theory for the optomechanical interactions in an optical resonator with a movable end test mass. I have also described the interaction Hamiltonian for the cavity optomechanics, in an effort to expose the nonlinear effects arising due to the fluctuating laser field and the mechanical motion of the movable mirror. Further I have laid foundation towards the optical spring effect used in my experimental setup for the measurement of QRPN and other optomechanical effects.

Chapter 3
Design Consideration: Microresonator Test Mass

3.1 Introduction

In this section I will describe the experimental consideration for the design of the movable test masses used for the tabletop demonstration of the nontrivial artifacts of optomechanical interactions and the direct measurement of the quantum radiation pressure noise.

As discussed earlier, the next generation of the GW interferometers are expected to be limited by the quantum radiation pressure noise or QRPN at the low frequencies of the detection bandwidth. QRPN arises in a continuous measurement as an outcome of the backaction of the mirror motion caused by the photon number fluctuations of the impinging laser field. These mirror motions in turn imprints as phase fluctuation in the light field being reflected from the mirror.

$$\begin{bmatrix} Intensity\ Fluctuations \\ of\ the\ Input\ Field \end{bmatrix} \Rightarrow \begin{bmatrix} Mirror \\ Motion \end{bmatrix} \Rightarrow \begin{bmatrix} Phase\ Shift \\ of\ the\ Output\ Field \end{bmatrix}$$

Hence the contributions of the radiation pressure noise can be seen in the output phase quadrature as an input amplitude quadrature dependent term is given as:

$$\hat{b}_2 = \mathcal{K}_{\rm rp}\hat{a}_1 + \hat{a}_2 + \tilde{h};$$

where as per Eq 1.33, the radiation pressure coefficient is given as

$$\mathcal{K}_{\rm rp} = \frac{4P_s\omega_o}{c^2 M_r \Omega^2}$$

Here we can see that the effects of QRPN are enhanced with the increased input

laser field, reduction in the mass of the mechanical oscillator, and a lower frequency of measurement. Hence the fabricated microresonator bragg mirrror structures that has a mass of about few hundred nanograms are the ideal candidates to directly measure the QRPN in a tabletop experiment.

Since our goal is to setup a prototype experiment for the testing and calibration of various noise evasion schemes to test their feasibility for the future generation of the GW detectors, the measurement of the optomechanical interactions should be close in frequency and bandwidth to the GW detectors. Taking into consideration the practical constraints of minimizing the requirement of active seismic isolation, we chose the natural mechanical mode frequency of the movable test masses to be mechanical oscillator to be in the range of few hundred Hz.

Ideally to infer the quantum mechanical of the prepared optomechanical state, the decoherence rate due to dissipation should be as low as possible. This condition require the microresonators to have very low transmission, mechanical and absorption losses. The decoherence time is further enhanced by using a high finesse, free space Fabry-Perot cavity as discussed in the earlier chapter.

Techniques like optical spring for vibrational isolation, optical dilution enhanced effective quality factor, and laser intensity/frequency stabilization for shot noise limited input laser field, are exploited to enhance the stable displacement response of the optical cavity. The noise floor for the measurement is further reduced by applying cryogenics to reduce the mechanical losses due to the Brownian noise. These considerations are discussed in details in the next chapter, where I will discuss the experimental details for the measurement and stabilization of thermal noise limited frequency response of the optomechanical setup.

3.2 Testing New Optical Coating for the Future Gravitational Wave Detectors

The test masses of advanced LIGO are made of high quality fused Silica (SiO_2) and coated for high reflectivity with an alternating layers of amorphous SiO_2 and Tantala (TaO_5). The SiO_2/TaO_2 coating provide high optical quality and low losses, but suffer a

severe limitation of introducing excess coating Brownian noise [17].

While cryogenic techniques are being considered to reduce these thermal fluctuations in the mirror masses of LIGO, new coating materials with lower Brownian noise are also being investigated for the next generation optics [30, 28, 29]. In the recent investigations, Cole et. al. studied the crystalline coatings of alternating stack layers of gallium arsenide (GaAs) and aluminum-alloyed gallium arsenide ($Al_xGa_{1-x}As$). These studies were done in part for developing new for the optical systems that include test masses for the next generation gravitational wave detectors. The optical, thermal conductivity and thermal noise performances of such crystalline coatings are asserted to be surpassing the amorphous metal oxides counterparts. It was also noted that mirrors fabricated with such crystalline coatings enjoy low optical losses over a wider spectral range [68].

In the next chapter, I presented the experimental investigations for the Brownian fluctuations in the highly reflective microresonator structures that are fabricated from the crystalline coatings of GaAs and ($Al_xGa_{1-x}As$). The further design considerations and the fabrication details of the cantilever microresonator structures are discussed below. Our investigations, being performed at a center wavelength of 1064 nm, are in parallel to the research and development of the new optical systems for the next generation gravitational wave detectors.

3.3 Fabrication Details of the Microresonator

The cantilever microresonators are fabricated by Dr. Garrett Cole from the Crystalline Mirror Solutions, from a molecular-beam-epitaxy-grown $GaAs/Al_xGa_{1-x}As/In_yGa_{1-y}P$ heterostructure using a novel double etch stop technique. The material structure consists of a single-crystal distributed Bragg reflector (DBR) based on an epitaxial GaAs (high index, nominal thickness of 77.8 nm for a center wavelength of 1078 nm) $Al_{0.92}Ga_{0.08}As$ (low index, thickness of 90.4 nm) multilayer.

As the ultimate goal is to operate this structure at cryogenic (liquid ^4He) temperatures, the mirror center wavelength is red-shifted to 1078 nm to take into account thermorefractive

effects upon cooling [30]. As shown in Figure 3.1, the DBR is grown atop a lattice-matched $In_{0.49}Ga_{0.51}P$ etch stop, a GaAs structural layer, and a second 3/4-wave optical thickness (271 nm) $Al_{0.92}Ga_{0.08}As$ etch stop.

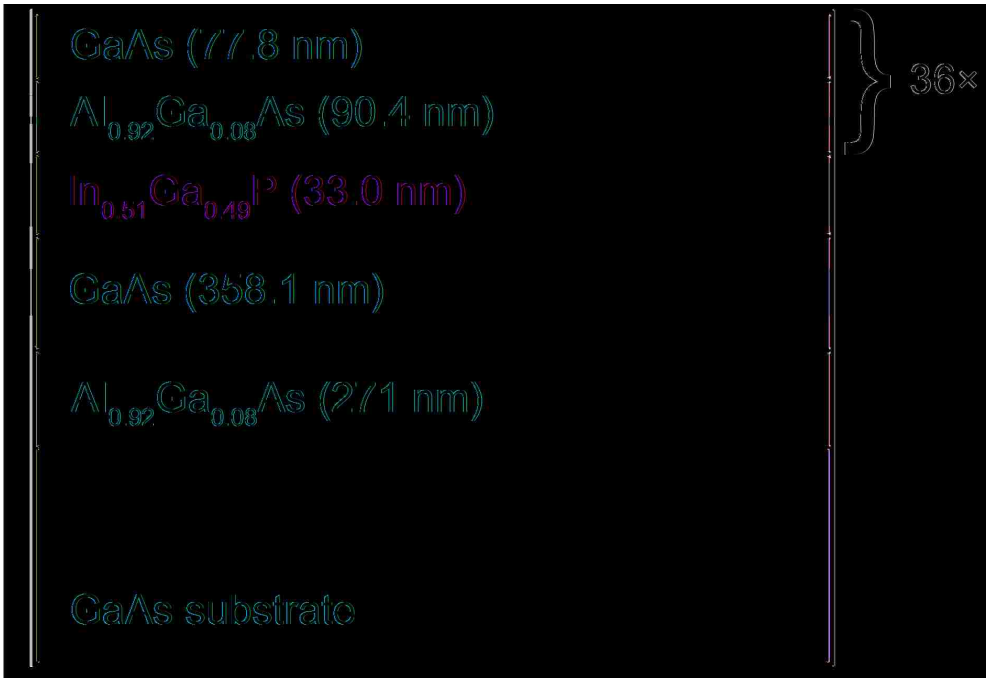

Figure 3.1: Layout of the stack layer structure of the Bragg mirror made from the single crystal GaAs and $Al_{0.92}Ga_{0.08}As$

Unlike the full-thickness mirror structures explored in our earlier work [28], in this design a circular mirror pad is fabricated on a thin film of GaAs in order to de-couple the optical and mechanical properties of the structure, enabling in this case a significant reduction in both the resonator effective mass and spring constant, while maintaining a smaller resonator footprint. This separately optimized structure is similar to previous demonstrations of epitaxial and dielectric resonator designs [60, 62, 63, 64]. To begin the fabrication procedure, the resonator mirror pad is first defined via optical contact lithographically, by patterning small discs ranging from 114-154 microns in diameter. The resist pads are then used as a mask for vertical etching of the DBR layers using a $SiCl_4$-based inductively-coupled plasma etch process. The etch depth is monitored in real time using an in-situ laser interferometer and carried out until only one mirror period remains above

the first etch stop. A phosphoric acid based wet etch ($H_3PO_4 : H_2O_2 : DI$) is then used to remove the final DBR layer pair, stopping with a selectivity of at least 35:1 on the underlying $In_{0.49}Ga_{0.51}P$. Minimizing the total time of this wet etching step avoids excessive undercutting of the DBR structure, maintaining the as-designed diameter to the $<5\ \mu m$ level.

After definition of the epitaxial mirror pad, the first etch stop is then removed with a dilute HCl solution, stopping with near infinite selectivity on the underlying GaAs structural layer. The addition of a lattice matched ternary $In_{0.49}Ga_{0.51}P$ film atop the GaAs structural significantly simplifies the microfabrication procedure due to the excellent chemical selectivity between the DBR and etch stop, as well as between the etch stop and underlying GaAs film, allowing excellent control over the mirror pad geometry and structural layer thickness. It is important to note that previous measurements on free-standing strained $InyGa_{1-y}P$ resonators has shown the potential for high mechanical quality factors in this material system [31], thus we anticipate no additional mechanical losses from the addition of this layer to the resonator structure.

Moreover, the surface of the thin GaAs support layer is only exposed to wet chemical processes and avoids potentially damaging reactive ion etching steps that may lead to excess mechanical losses. These structures ultimately show comparable room temperature quality factors (on the order of 20,000 at 300 K) to our previous low-frequency resonators sculpted from a full-thickness DBR [28]. To complete the definition of the lateral geometry of the resonator, a second lithography and ICP etch step is employed. Here, the etch progresses through the GaAs support layer, $Al_{0.92}Ga_{0.08}As$ backside etch stop layer, and into the GaAs growth substrate, ensuring vertical sidewalls on the final GaAs cantilever structure. The chips are then thinned using a mechanical lapping process to a final thickness of approximately 200 micrometers (original substrate thickness of 675 micrometers), re-polished, and, following a thorough clean, the chip is inverted and a silicon nitride (Si_xN_y) hard mask is deposited on the backside of the GaAs growth wafer via plasma enhanced chemical

vapor deposition (PECVD).

After temporarily mounting the chip to a glass handle using a high temperature wax, a backside lithography step is used to define windows in the PECVD hard mask. The windows defined in this step will ultimately be used to release the micromechanical devices. An SF_6-based RIE process is implemented to pattern the Si_xN_y film and the devices are finally undercut and left free-standing by selectively removing the underlying GaAs growth substrate with a selective $H_2O_2 : NH_4OH$-based wet chemical etch. This process is carried out in an ultrasonic bath to ensure removal of any passivating films formed in etching. This process ultimately terminates on the backside $Al_{0.92}Ga_{0.08}As$ etch stop layer, while the sidewalls of the cantilever and Bragg mirror are protected by the mounting wax layer. To clean up and free the resonators, the etch stop is removed in a dilute hydrofluoric (HF) acid solution and, after rinsing thoroughly, the samples are soaked in acetone to remove the protective wax and demount the chips from the glass handle. Finally, the samples are transferred to an ethanol bath and a critical point dryer is used to avoid collapse of the free-standing resonators during the solvent removal stage.

As discussed previously [65], a small but finite lattice mismatch in the high and low index layers of the epitaxial DBR result in the birefringent properties of the epitaxial DBR. The additional InGaP film may also contribute local stress in this case assuming imperfect composition control [31]. We exploited, the birefringence property of the Bragg microresonator structures are exploited to achieve a single input field stable optical trap. The details of the experiment are discussed in Chapter 5 of this thesis.

Chapter 4
Experimental Details: Towards the Measurement of the Quantum Radiation Pressure Noise

4.1 Phase I: Thermal Noise limited Measurement.

4.1.1 Introduction

In an movable end mirror Fabry Perot cavity, the response of the mechanical system is monitored by the laser light circulating inside the cavity. The precision of such an interferometric system is fundamentally limited by the classical thermal noise inherent to the reflective coatings of the optical test masses. Such classical noise normally mask any nonclassical optomechanical effect that include the quantum backaction due to the photon number fluctuations inherent to the laser light probing the mirror motion [33].

Generally, a mechanical oscillator is coupled to its noisy environment through the cantilever support that may lead to dissipative flow of thermal phonons from the noisy environment. This flow of energy into the optomechanical system leads to excess mechanical dissipation along with large Brownian fluctuations of the macroscopic oscillator. In order to infer the quantum superposition of an optomechanical system, it is desirable to prepare the system in a low energy state that can survive more than one oscillation period n_{osc} [66, 32]. To minimize the thermal decoherence of the prepared ground state, the test mass should be mechanically decoupled from the environment. The rate of thermal decoherence is ideally governed by the mechanical damping of the oscillator, and can be quantified as:

$$\frac{1}{\tau} = \frac{\Gamma_m k_B T}{2\pi\hbar\Omega_m}, \tag{4.1}$$

where τ is the thermal decoherence time, $\Gamma_m = M\Omega_m/Q_m$ is the mechanical damping constant for M to be the mass of the oscillator and Q_m is the mechanical quality factor, T

is the effective temperature, and Ω_m is the eigenfrequency of the mechanical resonance.

Hence to maximize the thermal decoherence time, it may seem obvious to develop mechanical oscillators with a higher eigenfrequency. But the excessive damping of such high frequency oscillator may lead to decoherence of the prepared optomechanical state, unless compensated by a very high mechanical quality factor. The fabrication of a high Q_m and high Ω_m oscillator pose a great technical challenge due excessive mechanical, other thermoelastic losses.

In addition, most of the macroscopic mechanical oscillators that include LIGO test masses, tend to have a very low mechanical eigenfrequency due to their masses. Hence it is of vast scientific interest to develop optomechanical systems with low mechanical frequency oscillators that has high optical and mechanical quality.

4.1.2 Optical Dilution

In 2007 Corbitt *et al.* [57] demonstrated the technique of optical dilution for an enhanced displacement sensitivity of a broadband optomechanical measurement. The optical dilution is based on fluctuation-dissipation model, where a soft mechanical spring (K_m) ensure a maximal decoupling of noise sources from the mechanical oscillator. The prepared oscillator state is rendered stiff by a strong optical restoring force provided by radiation pressure of the blue detuned laser field. The optical spring $K_{\rm os}$ provided by the laser field shifts the mechanical oscillator's resonant frequency without adding any excess sources of mechanical decoherence. This effect leads to an enhanced effective quality factor ($Q_{\rm eff}$) of the optomechanical system at an observation frequency $\Omega > \Omega_m$, given by equation below.

$$Q_{\rm eff} = Q_m \frac{K_{\rm os}}{K_m} \Rightarrow Q_m \left(\frac{\Omega_{\rm os}}{\Omega_m}\right)^2, \tag{4.2}$$

where Ω_m is the eigenfrequency of the mechanical oscillator, and Ω_{os} is the effective resonant frequency of the optomechanical system. It should be noted that counter-intuitively the

mechanical spring is desired to be as soft as possible in order to maximize the thermal decoherence time of the prepared optomechanical state. The effective shift in the resonance frequency of the fabricated microresonator with a mechanical eigenfrequency of about 264 Hz is shown in Fig 4.1 below. Here the microresonator is used as an end mirror of a high finesse optomechanical Fabry-Perot cavity.

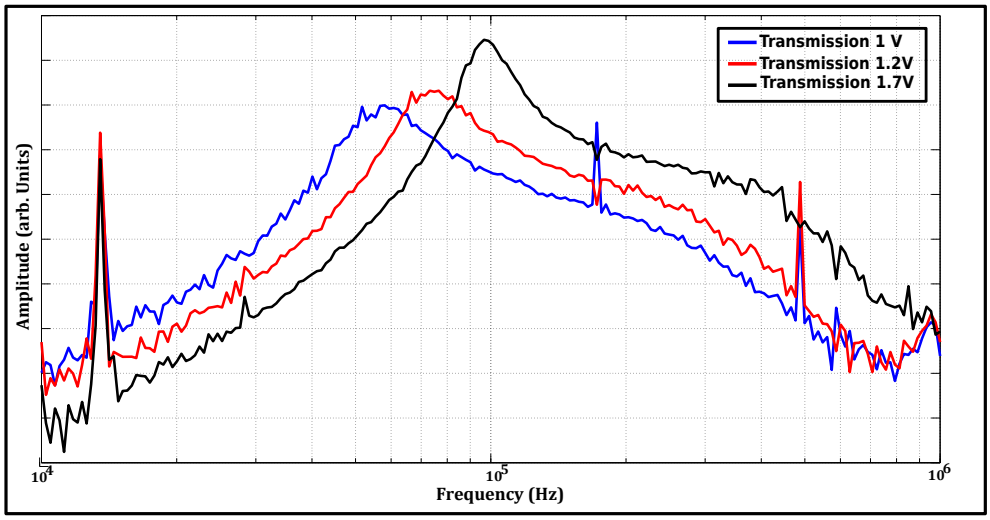

Figure 4.1: A plot showing the enhanced shift in the resonance frequency of the microresonator of eigenfrequency 264 Hz. The detuning of the blue shifted optical cavity is given in terms of the transmission power measured at the photodetector.

The principle of optical dilution works similar to gravitational dilution, where a fraction of energy is stored in the noiseless gravitational field. In optical dilution the fraction of the energy is stored in the noiseless optical field that has a very low moment of motion at the low frequencies.

Together with the high mechanical quality microresonator test mass, we exploit a high finesse optical cavity to achieve a displacement sensitivity that is limited by the Brownian fluctuations of the microresonator test mass. We further demonstrate the improvement in the sensitivity of our optomechanical system by the use of cryogenics that minimize the thermal fluctuations. Such improvements in the displacement sensitivity of the optomechanical system lays the foundation towards our further research to expose and exploit the quantum mechanics of a macroscopic test mass.

4.1.3 Numerical Analysis

Further design considerations and the thermal noise budget for the cantilever microresonators to be fabricated for our experiment are inferred through a finite element analysis (FEA). The FEA derived modal masses (m_n) and the respective frequencies (Ω_n) depends on the microresonator mass, mechanical eigenfrequency, and the structure of the cantilever support. The theoretical prediction for the root-mean-squared thermal fluctuations x_{rms} of the microresonator structures is calculated as:

$$x^2_{\mathrm{rms,therm}} = \sum_{n=1}^{\infty} \frac{4k_B T}{m_n Q_n \Omega} \frac{\Omega_n^2}{(\Omega - \Omega_n^2)^2 + \Omega_n^4/Q_n^2} \tag{4.3}$$

where Q_n is the quality factor for n modes, k_B is the Boltzmann constant, and T is the temperature of the microresonator bath.

The numerical model based on the FEA substantiate the thermal noise predictions that for for a given mechanical quality factor (Q_m) and at the observed frequency (Ω) higher than the mechanical resonance (Ω_m), the effective coating Brownian noise that is driven by the excess mechanical dissipation, is reduced as the resonant frequency of the resonator is reduced. Fig 4.2, shows a predicted thermal noise floor for the two microresonator structures with mechanical eigenfrequencies of 264 Hz and 700 Hz, and a mechanical quality factor of 20000.

Using the designed geometry and anisotropic elastic constants of the multilayer microresonator, the FEA produces resonant frequencies within a margin of error. The numerical model incorporates a Gaussian probe on the cantilever head with a radius matched to that of the optical cavity mode in order to accurately predict the optically-sampled effective modal masses. The calculated noise curve assumes a constant loss angle for each mechanical resonance, an assumption independently verified through ringdown measurement of the individual mechanical modes. Furthermore, the measurement of similar Q values at MHz frequencies for the same materials system suggests that the damping mechanism is likely

velocity-independent and structural in nature. This realization suggests that reduced thermal noise could be obtained by engineering the geometry of the system to reduce the impact of these modes.

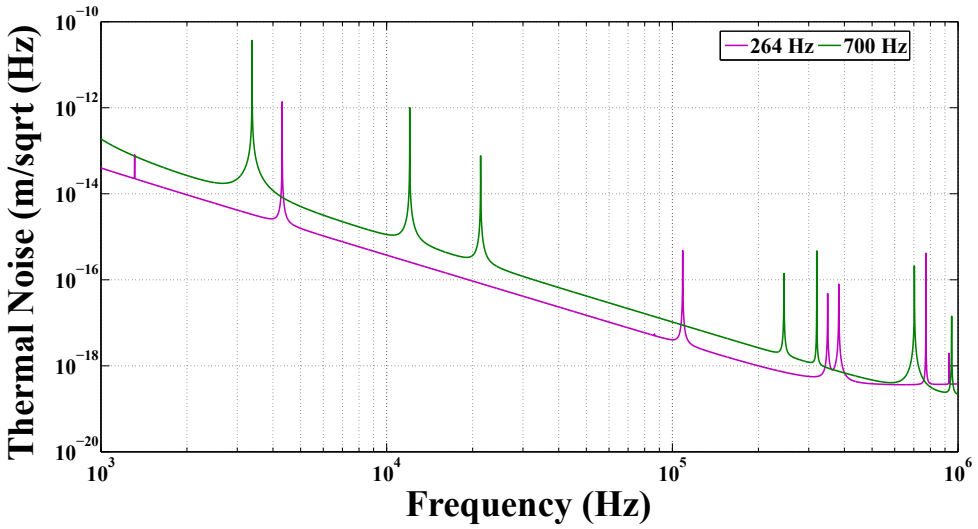

Figure 4.2: Comparison of FEA model for the broadband thermal noise of the microresonator of different eigenfrequencies of mechanical oscillation.

4.1.4 Experimental Setup

The schematic of the experiment performed to measure the thermal noise of the microresonator structure, is shown in Fig 4.3. We use an intensity stabilized, Nd:YAG laser of center wavelength 1064 nm, to probe a one centimeter long Fabry-Perot cavity that is placed in vacuum to reduce any noise due to acoustic effects. The high finesse in-vacuum cavity consists of a fixed 0.5 inch input mirror that has a high optical quality, and a radius of curvature of 1 cm. The optical field transmitted through the input mirror is focused onto a highly reflective microresonator that acts as a movable end test mass. The microresonator is about 400 nanograms in mass and about 100 micron in diameter. The natural (eigen-)frequency of mechanical oscillation for the microresonator used in the experiment, is about 180 Hz. The input mirror is mounted onto an agilis mirror mount through a piezoelectric device that gives us both an ability to fine tune the cavity axis and sweep through the resonant modes of the cavity. Cryogenics is applied through an

open cycle helium cryostat, to cool the microresonator test mass that is thermally isolated from the rest of experimental setup. Scattering losses are minimized by a precise alignment of the microresonator end test mass that is mounted onto the Agilis mirror mount and a movable three axis stage. The transmitted field from the microresonator end test mass is used to qualitatively analyze the cavity modes, study the cavity noise spectrum, and generate a feedback error signal to stabilize the intensity of the input laser field.

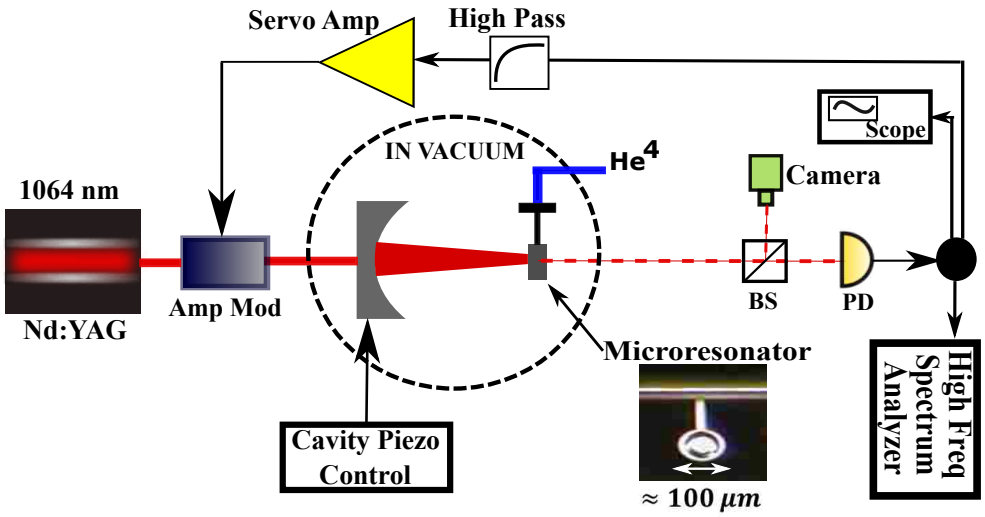

Figure 4.3: Experimental setup: The 1064 nm Nd:YAG laser outputs a 500 mW of laser field. The intensity of the input light is stabilized by actuating the amplitude modulator (Amp Mod) through a high pass feedback control loop. The input laser field enters the in-vacuum optomechanical cavity from the back of a fixed half inch diameter curved input mirror that focuses the intracavity field onto the 100 micron wide mirrored microresonator (inset). The input mirror is mounted on a piezoelectric device to sweep the cavity through its resonant modes. A 90:10 beam splitter (BS) splits the transmitted field towards a broadband photodetector for signal analysis and a CCD camera for a qualitative view of the resonant intracavity mode, respectively. The photodetector signal is used both to generate an error signal for the feedback control and signal analysis for the displacement noise spectrum. The microresonator chip is cooled by a continous flow helium cryostat.

The system resides far into the "bad-cavity" regime where the cavity linewidth γ is much greater than the fundamental mechanical resonance frequency, $\frac{\gamma}{\Omega_m} \sim 10^5$. In addition to the side of fringe locking scheme and large oscillator compliance, this ensures that there will be a significant optical spring effect [67, 58, 69, 59]. In order to achieve accurate calibration, we directly measure the transfer function from an injected modulation of the

laser frequency to the error signal and use this information to convert the measured voltage spectral densities into displacement. It should be noted that this method takes into account the optomechanical response of the cavity, including the optical spring. Figure 4.4 shows the measured displacement noise of the 180 Hz cantilever for a frequencies from 1 kHz to 30 kHz. The displacement noise is measured both at room temperature and when the microresonator is cooled to about 16 Kelvin. Below 1 kHz the spectrum is limited by excess acoustic vibrations of the laboratory setup. At frequencies above 100 kHz, radiation pressure contributes much less to the total imprecision and the noise contribution from the higher order mechanical modes dominate the displacement spectra.

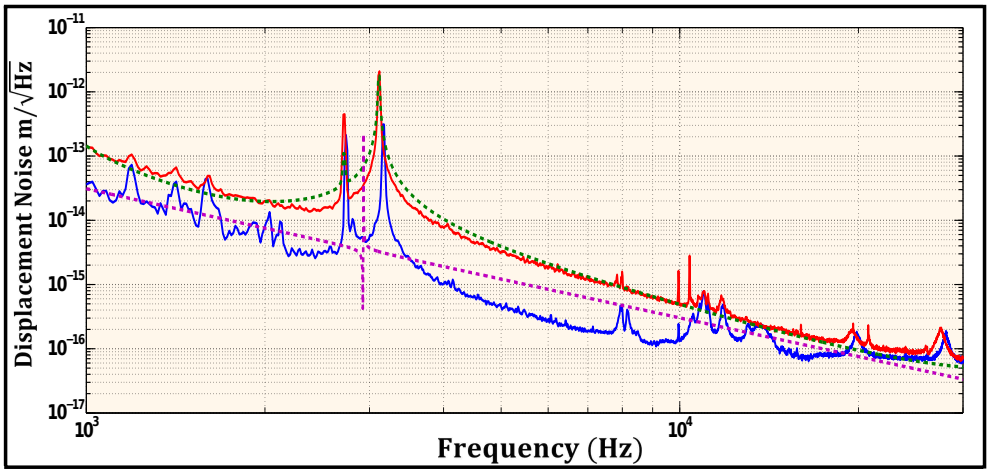

Figure 4.4: Displacement spectra of a microresonator with a mechanical eigenfrequency of 180 Hz at 293 Kelvin and 16 Kelvin. The dotted green curve is the FEA model prediction of the thermal noise for the microresonator at 293 Kelvin. The peak at around 3 kHz is the higher order mechanical mode of the microresonator. The predicted QRPN shows anti-resonances because of interference between different degrees of freedoms of the mechanical system.

It should be noted that the predicted QRPN is in principle exposed when the microresonator is cooled to 16 Kelvins. The detection of QRPN however is more tricky in the continuous dc readout detection. This is due to a number of reason. As explained in [61], the photodetector in principle is insensitive to the origin of power fluctuations. Since the measured noise is in the same quadratrure that is responsible for the backaction effect, the error signal gnerated by the photodetector contains the information about these fluctuations

and hence may partially get cancelled by the feedback loop. Further assumptions for the deterioration of the cavity finesse, and the quality factor of the microresonator, are valid but can be offset by higher input power.

Hence to measure the quantum radiation pressure noise and eventually the ponderomotive squeezing effects of the optomechanical interactions, either a modified detection (homodyne) scheme for the signal extraction through common reference must be employed, or the feedback scheme must be modified to avoid cancellation of the QRPN signal.

It should be noted that a single field homodyne detection is especially challenging owing to the fact that a limited output signal available for both the feedback control and the Homodyne detection.

4.2 Phase II: Measurement of the Quantum Radiation Pressure Noise

4.2.1 Introduction

As asserted in the previous section, the mirror motion due to the quantum fluctuations in the intensity of the laser field can be effectively cooled by feedback control. In other words it is not ideal to use the same signal that controls the cavity dynamics through feedback, to analyze the effects of backaction effects caused by the feedback controlled input field. The effective cancellation is proposed to mitigate the backaction noise or the quantum radiation pressure noise. Being said that, it is important to quantify the amount of cancellation so weigh in the efficacy of such a mitigation scheme. Hence the direct measurement of the QRPN is still very important. In this section, I will briefly describe the ongoing investigations and the experimental development towards the measurement of the QRPN.

4.2.2 Experimental Setup

For exposing the quantum backaction of QRPN effects, we chose a pump-probe scheme, where the optical cavity is driven by the pump field blue detuned to the resonant frequency. The pump field generate the error signal for the feedback control to manipulate and stabilize

the dynamics of the optomechanical cavity. A second (probe) laser field that is mode matched and phase locked at an offset to the pump field, is injected into the optical cavity. The input probe field is intensity stabilized to minimize the classical noise in the amplitude of the input probe field. Schematic of the experimental setup is shown in the Fig 4.5, below. The pump and the probe fields are input in orthogonal polarizations in the reference frame of the cavity axis. The orthogonal output transmissions due to the pump and the probe field are seperated by a polarizing beam splitter. Similar to the experimental setup for the thermal noise measurement, the pump field is sent to a CCD camera and a photodetecto. The photodetector signal from the pump field is used for generating an error signal for the feedback loop, and process the signal for inferring the dyanamics of the mechanical microresonator. The probe field is simply detected by another photodetector in orthogonal polarization that gives an information about the circulating power in the probe field. A future upgrade for the homodyne detection of the probe field is possible to further expose the SQL limited performance of our experimental setup.

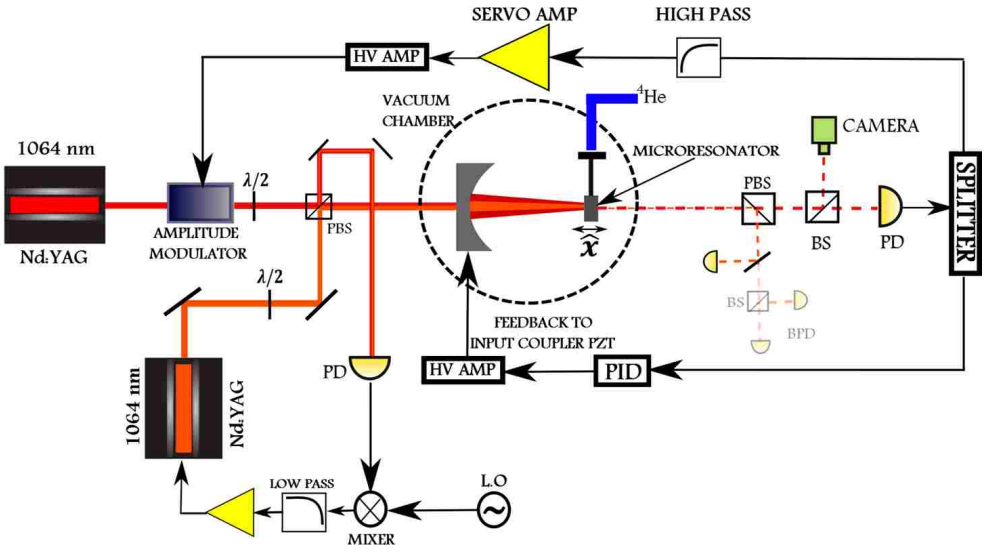

Figure 4.5: A schematic of the experimental setup for the proposed measurement of the quantum radiation pressure noise and the artifact of the quantum correlations between the optical cavity and the microresonator end test mass.

4.2.3 Measurement of Quantum Correlations

The pump-probe scheme exploited here for the measurement of the QRPN offer various advantages in the continous measurement schemes.

a) Since the optomechanical dynamics are controlled by the orthogonal pump field, the probe field does not get stabilized by the feedback signal. Hence any mirror motion caused by the probe field is not cancelled by the subsequent intensity manipulations of the input field. Further such mirror motions

b) The probe field can be operated close to the resonance to enhance the quantum effects, which can be used in future, to improve the level of ponderomotive squeezing generated due to parametric correlations of the optomechanics.

c) Probe field can be used as a test bed for the experimental demonstration of the noise evasion by various proposed schemes that include the variational readout, speedmeters, and other QND detections.

d) Such scheme further lay foundations towards investigating the exotic regimes of hybrid quantum optomechanics, quantum chromodynamics and the macroscopic many body investigations,

In principle any mirror motion induced by the quantum fluctuations in the intensity of the probe field, should induce a correlated noise in the pump field. Hence for a pump field to be essentially limited by the noise from the probe field, the quantum backaction effects can be extracted either through signal processing or averaging out the random noise similar to Weiner filtering. Fig 4.6 shows the experimental progress towards building up the correlations between the pump and the probe field. Ideally the cavity dynamics stabilized through the pump field, can be rendered noisy by the probe field. If the probe field is intensity stabilized to be shot noise limited, the quantum correlations between the probe field and the mechanical resonator should in principle be visible in the analyzed pump signal.

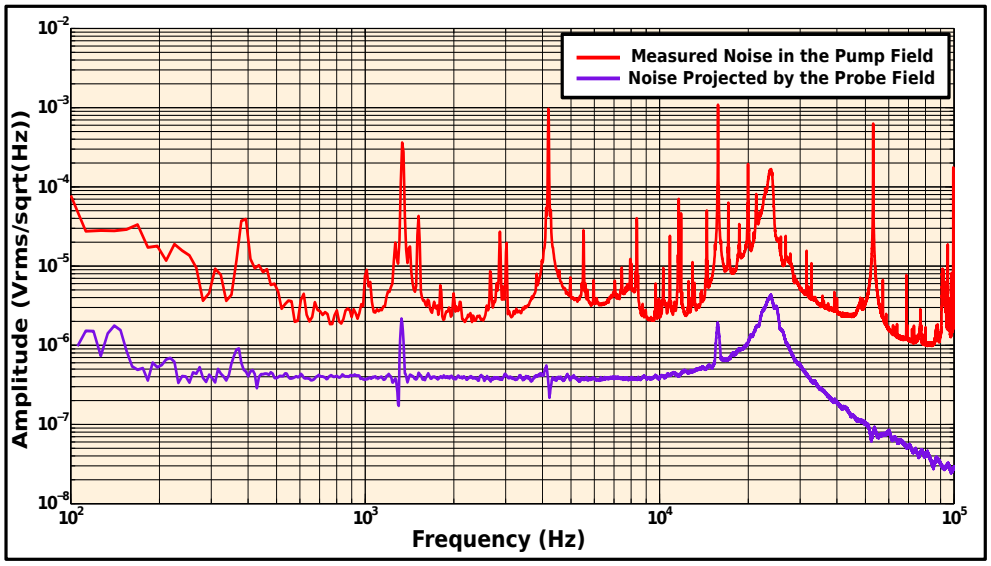

Figure 4.6: Noise plot showing the total noise in the pump field and the noise contribution of the probe field that is projected onto the pump field.

4.3 Overview

In this chapter, I have described the ongoing experimental investigations for the measurement of the quantum radiation pressure noise in an optomechanical cavity. The fabricated high quality microresonator are used as end test mass of the high finesse Fabry-Perot cavity. The sensitivity of our optomechanical system is limited by the mechanical dissipation and the noise due to the thermal decoherence of the microresonator. These dissipative forces are reduced by applying cryogenics to cool the thermal fluctuations in the mechanical mass. At low temperature the displacement noise sensitivity is masked by the combination of shot noise limited input field, and the exciations of the higher order mechanical mode. Further I have shown the future goals towards exposing the quantum correlations using two input optical fields in a pump-probe regime. These artifacts of these quantum correlations are further proposed to push the sensitivity of the experimental setup beyond the Standard Quantum Limit. The aspiration to achieve the sub-SQL sensitivity is based on our numerical analysis of the displacement noise performance of the microresonator, as shown in Fig 4.7. It is to be noted that given and ideal detection, the sub-SQL performance is expected at

the higher than 40 kHz frequency band.

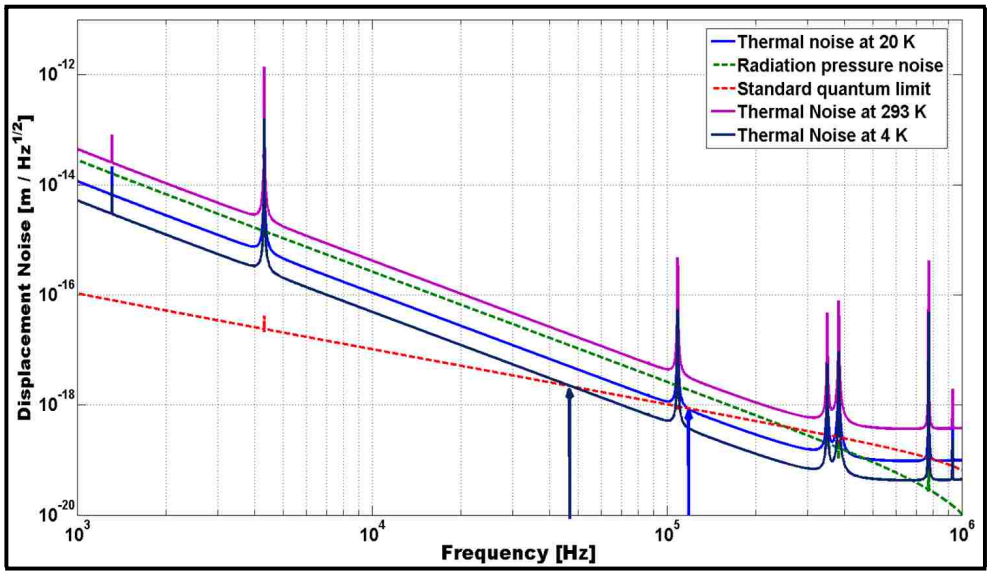

Figure 4.7: FEA based numerical model for the sub-SQL noise performance of the microresonator based optomechanical cavity.

Future upgrades include exposing the quantum correlations at room temperature. This idea require a very high finesse and stable optomechanical cavity that is probed by a shot noise limited input field. The prospective signal processing schemes for the averaging of the random noise is under consideration. One such effort is to build a high frequency dual optical trap, where a feedback signal is not required to stabilize the dynamics of the optomechanical cavity. Such optical traps serve as potential candidates exposing the quantum mechanics of the macroscopic objects without a need to cool them to their mechanical ground states.

Chapter 5
Stable Optical Trap due to the Birefringence of the Microresonator

5.1 Introduction

It is well established that in an opto-mechanical cavity, the radiation pressure due to the circulating field can act as a (anti-)restoring and (anti-)damping force, depending on whether the cavity is red or blue detuned [70, 59, 58, 71]. The (anti-)restoring force is generated by the position dependent intracavity power and radiation pressure, while the (anti-)damping force is due to the finite response time of the cavity to changes of the mirror position. When the cavity is detuned to a frequency higher than the resonant frequency (blue detuned), the radiation pressure gives rise to a positive restoring force and an anti-damping force. Likewise, when red detuned, anti-restoring and positive damping forces are generated. For systems that operate below the detuning frequency, this generally leads to instability from either an anti-restoring or anti-damping force. The optical spring formed by a restoring force has a profound effect in systems with soft mechanical suspensions and can be used to enhance the sensitivity of detection by amplifying the mirror's motion. The strong anti-damping force can dominate the mechanical damping in this scenario giving rise to dynamic instabilities [72, 67, 73], and is usually stabilized by actively controlling the optical response of the cavity through feedback loops [72, 67].

In 2007, Corbitt *et al.* introduced a dual carrier stable optical trap, in which a damping force due to a red detuned sub-carrier field cancels out the anti-damping force due to the blue detuned carrier field [56]. That approach eliminated the need for electronic feedback, but required using two distinct optical fields incident on the cavity. Recently, a new approach that exploits the bolometric backaction due to the photothermal effect was proposed by Kelley et. al. [74]. This approach produces a damping force by exploiting the thermal expansion of the mirrors from absorption the intracavity optical field. Though

stable, such optical absorptions introduces excess vacuum fluctuations and deteriorates the sensitivity of the device.

In this chapter, I will introduce a new scheme to achieve a stable optical trap by exploiting the birefringence inherent to the mirrors, without relying on absorption or multiple carrier fields. In this scheme of stable optical trap, a single field with linear polarization is injected into the optical cavity. The cavity consists of a 0.5 inch input mirror and a microfabricated mirror supported on a cantilever as the end mirror. The microresonator is fabricated from a stack of crystalline $Al_{0.92}Ga_{0.08}As/GaAs$ layers and is inherently birefringent, resulting in differing resonance conditions for the orthogonal polarizations. The two polarization components of the input field undergo a relative phase shift as a function of the birefringence. This phase shift allows the two polarization components to operate at different cavity detunings from each other, which gives the stable double optical spring effect. We note that the phase shifted polarizations behave as if there were two input fields. We will call these orthogonal polarization components as the carrier (C) and the subcarrier (SC) polarizations, for convenience.

The schematic shown in Fig 1 describes the experiment performed to demonstrate our scheme. Initially the intensity of the laser field from the Nd:YAG laser is modulated by an amplitude modulator through a servo-controlled feedback signal from the transmitted cavity output field. This feedback is necessary to keep the opto-mechanical effects stable until the cavity reaches the self-stable regime. The polarization angle of the input field is set using a combination of two half wave plates and a polarizing beam splitter, such that the power in the C polarization is about 22 times the power in the SC polarization.

The in-vacuum cavity is one centimeter long and consists of an input mirror that has a radius of curvature of one centimeter. The input mirror is mounted on a piezoelectric device, to allow for fine tuning of the cavity length. The optical field is focused on a microresonator that is about 100 micron in diameter, and about 400 nanograms in mass. The microresonator has a natural mechanical frequency of $\Omega_m = 2\pi \times 274$ Hz with a

mechanical quality factor $Q_m \approx 2 \times 10^4$. The birefrengence induced frequency shift of the resonance condition between the two polarizations in our experiment is measured to be about 7.4 times the cavity linewidth (HWHM) of $\gamma \approx 2\pi \times 254$ kHz.

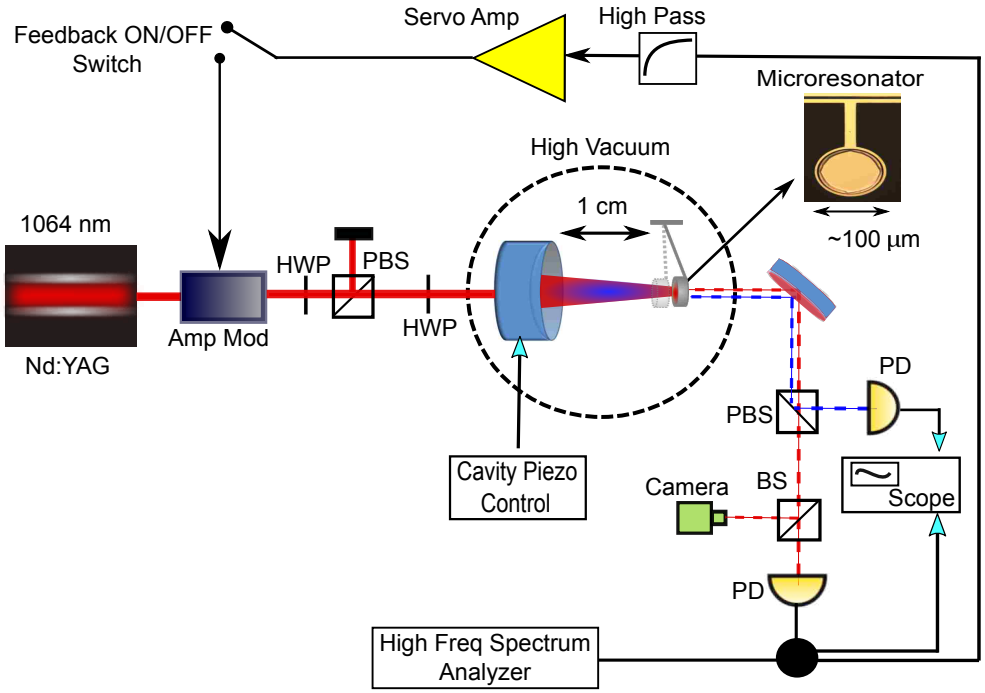

Figure 5.1: Experimental setup: The 1064 nm Nd:YAG laser outputs a 500 mW of laser field. The intensity of the input laser field is controlled by the amplitude modulator (Amp Mod) through a high pass feedback control loop. The first half wave plate (HWP) and a polarization beam splitter (PBS) sets the power of the input laser field to 64 mW and the second HWP controls the power ratio between the carrier (C) and subcarrier (SC) polarization components of the input field to about 22:1. The cavity is located inside a vacuum tank and consists of a 0.5 inch input mirror and the 100 micron diameter microresonator (inset). The transmitted signals from the carrier (red) and the sub-carrier (blue) components are separated by a PBS. A 90:10 beam splitter (BS) splits the carrier transmission for a signal detection by a photodetector and a qualitative detection by a camera. The carrier photodetector signal is used for signal analysis and as an error signal for the feedback control.

The transmitted field from the end mirror is used to qualitatively analyze the cavity modes, analyze the cavity noise spectrum, and to generate a feedback error signal for the initial control of the cavity. The C and the SC components of the transmitted fields are separated using a polarizing beam splitter, and the amplitude of the SC transmission is measured by a photodetector. The transmitted C polarization is further split by a 90:10

beam splitter for which 10% of the signal is detected by a CCD camera for a qualitative analysis of the cavity modes. The rest of the C transmission is detected by a photodetector and is used both for the initial feedback control and the signal analysis of the cavity features. The electronic feedback control to the intensity of the input field is turned off once the self-stable regime is reached.

5.2 Calculations and Measurements

The power inside the cavity and the resulting radiation pressure on the microresonator test mass depends on the resonance condition of the cavity. For a large cavity linewidth, we take the frequency of motion $\Omega \ll \gamma$, such that the associated spring constant is given by [74].

$$K_{\rm os} = \frac{16\pi P_{\rm in} T_1 \sqrt{R_1 R_2^3}}{c\lambda_o (1-\sqrt{R_1 R_2})^3} \frac{\delta_\gamma}{\left(1+\delta_\gamma^2\right)^2} \tag{5.1}$$

where $P_{\rm in}$ is the input power of the laser field. T_i and R_i are the transmittance and the reflectance of the input mirror ($i = 1$) and the end test mass ($i = 2$), $\delta_\gamma = \delta/\gamma$ is the field detuning in terms of the cavity linewidth, λ_o is the center wavelength of the input laser field, and c is the velocity of light.

In addition, the detuned cavity has a finite response time on the scale of γ^{-1} and hence the intracavity power buildup lags the mirror motion. This lag in effect leads to a viscous damping force with a damping coefficient given by [59, 67], again under the assumption that $\Omega \ll \gamma$:

$$\Gamma = \frac{2{\rm K}_{\rm os}}{M\gamma[1+\delta_\gamma^2]} \tag{5.2}$$

where M is the reduced mass of the two cavity mirrors. Compared with the fixed mirror the microresonator has a negligible mass and hence the reduced mass is simply equal to the mass of the cantilever.

In a stable cavity operation, the equilibrium is maintained by a positive restoring force and a strong damping force. These forces requires a positive spring constant ($K > 0$) and a

negative damping coefficient ($\Gamma < 0$). But as is evident from the dependence of K and Γ on the sign of δ (Eq. 1 and Eq. 2), a positive (restoring) spring constant implies instabilities due to negative damping force, under the assumption that $\Omega \ll \gamma$. The instabilities due to negative damping usually requires a feedback control.

In our experiment, the system is stabilized by adjusting the detuning of the C and SC components of the intracavity field such that the blue detuned C polarization component creates a large restoring force and only small anti-damping force, while the red detuned SC polarization creates a small anti-restoring force and a large damping force. At detunings of $\delta_C \approx 5.3\gamma$ and $\delta_{SC} \approx -2.1\gamma$, the intracavity carrier and subcarrier polarizations component fields interact with the mechanical system resulting in $K_{\mathrm{tot}} \Rightarrow K_{\mathrm{C}} + K_{\mathrm{SC}} > 0$ and $\Gamma_{\mathrm{tot}} \Rightarrow \Gamma_{\mathrm{C}} + \Gamma_{\mathrm{SC}} < 0$.

Fig 5.2 depicts the numerical model for operating regimes of our system at a fixed input power. The total optical rigidity due to the two polarization field components is plotted as a function of carrier and the sub-carrier detunings. The numerical model is in agreement with our experimentally observed stable optical trap, as can be seen from the locking acquisition of our opto-mechanical system (Fig 5.3). The blue dotted line in Fig 5.2. correspond to the locking acquisition in Fig 5.3 where the amplitudes for the transmission of the carrier (I), subcarrier (II), and the feedback control signal are shown. The feedback control signal is designed to provide a damping force and is capable of counteracting the optical anti-damping that is dominant during initial locking, which is shown as region 1 in Fig. 2 and 3. When the system crosses into region 2, the SC crosses onto the other side of resonance, and exerts a strong anti-restoring force. The feedback is unable to counteract an anti-restoring force, and the system oscillates uncontrollably. As the SC detuning increases, and the system moves into the stable region 3, the system stabilizes as the restoring force from the C exceeds the anti-restoring force of the SC. At this point, the feedback loop is turned off, and the system remains locked and stable. This does result in slightly higher vibration levels in the absence of the damping feedback loop.

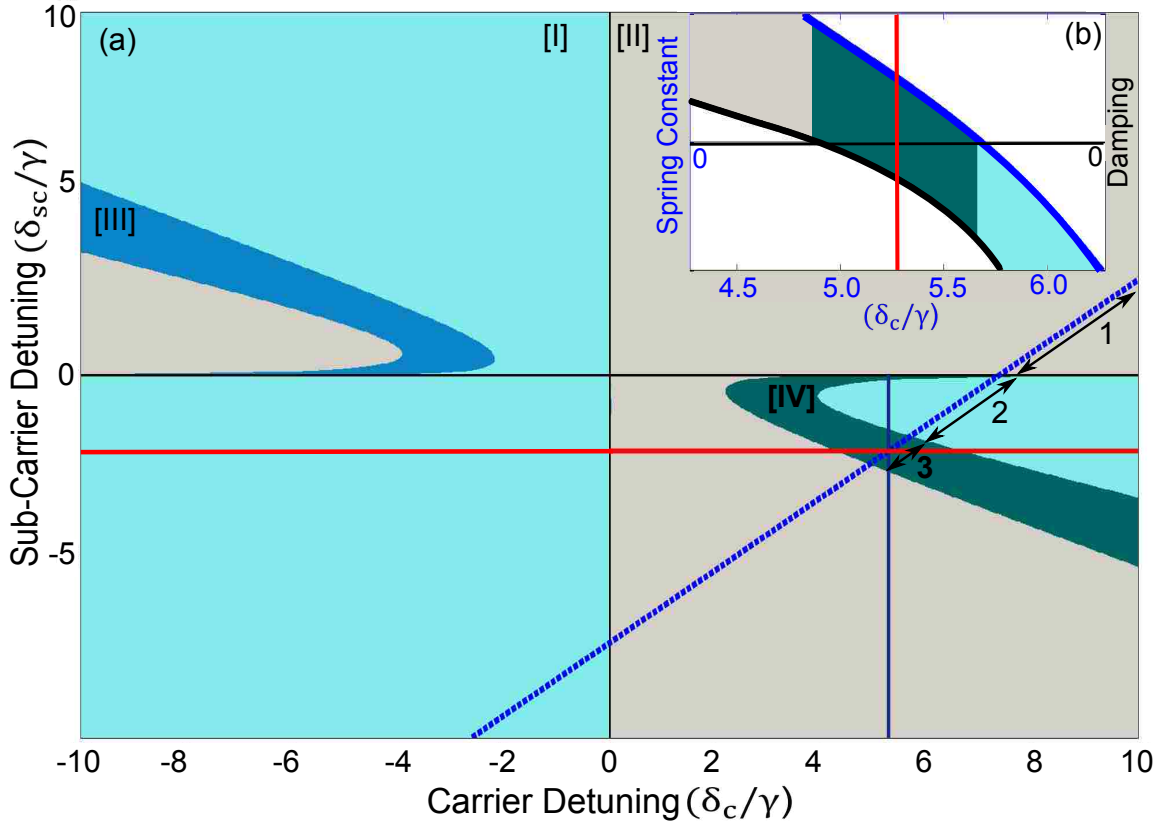

Figure 5.2: Graphical representation for the total optical rigidity as a function of detunings of the carrier C and subcarrier SC at a fixed input power ratio of 22:1, respectively. The shaded regions [I], [II], [III], and [IV] respectively correspond to statically unstable region with K<0 and Γ<0, dynamically unstable region with K>0 and Γ>0, anti-stable region with K<0 and Γ>0, and stable region with K>0 and Γ<0. The dotted blue line represent the trajectory of the C over the cavity resonance and agrees with both the calculated and the experimentally measured data. Regions 1, 2, and 3 on the trajectory of C are in direct correspondence with the real time sweep data as shown in Fig 3. A stable optical trap is achieved at $\delta_C/\gamma \sim 5.3$ and $\delta_{SC}/\gamma \sim -2.1$. The inset (b) shows the spring constant and damping as a function of δ_C/γ, K and Γ where the vertical red line represent the stable optical trap from the experimental data.

The inset plot (b) of Fig 5.2 depicts the total spring constant and the damping coefficient due to the two polarization components, as a function of carrier detuning around the stable optical trap region. The results further correspond to the experimental measurement for the optical spring response at a polarization dependent stable optical trap, as discussed above.

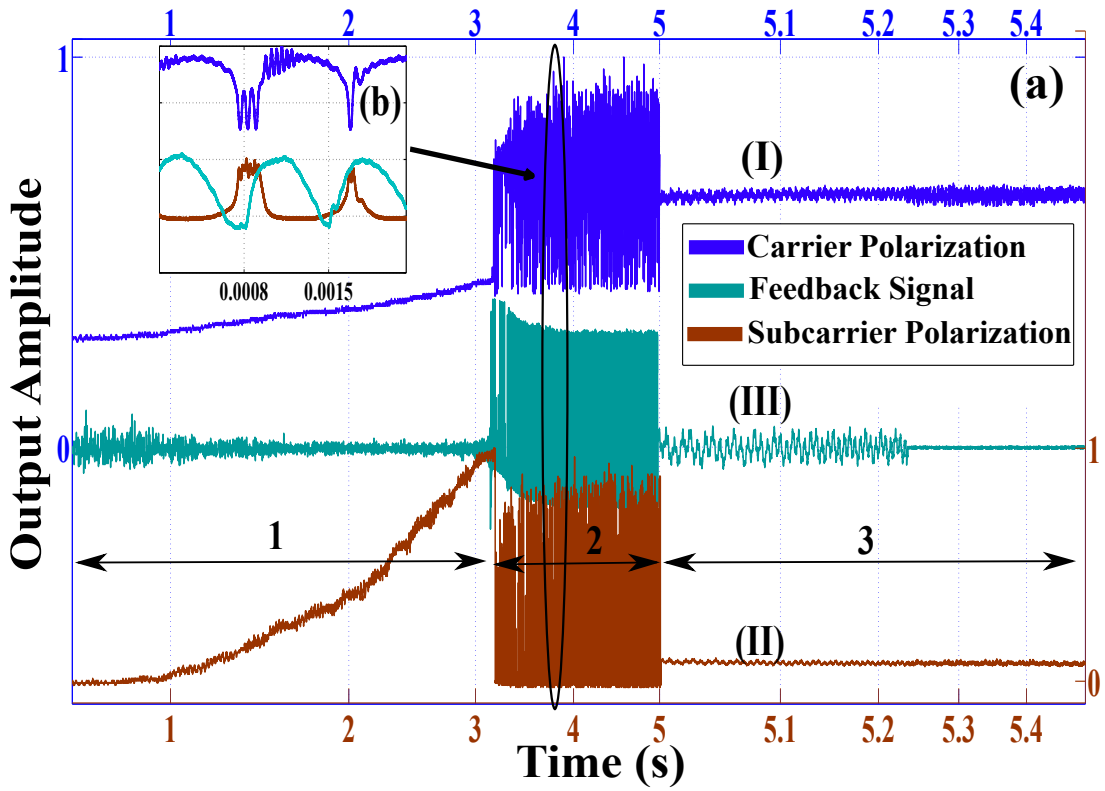

Figure 5.3: The real time sweep data showing the output signal for the C polarization (I), the SC polarization (II), and the feedback to the Amp Mod (III). The region 1 of the plot shows the rise in the amplitude for the C and the SC polarizations, as they sweep up the resonant cavity. Oscillations as a result of static instabilities are shown in the region 2 of the plot and are magnified in the inset plot (b). The region 3 of the plot shows the system being stable and independent of the feedback control, as shown in region of the plot where the feedback is turned off.

As shown in Fig 5.4, the mechanical resonance of the microresonator is shifted from 274 Hz to about 21 kHz. The optical trap is stable as can be seen from the decrease in the phase, allowing the system to be operated without any electronic feedback control. The fluctuations of the optically trapped mirror are relatively large for the performed measurement regime, and we believe that these fluctuations may give rise to some non-linearities that may be contributing to the noise in this measurement. Fig 5.4 shows the effects of such fluctuations on the measured Q of the oscillator as compared to the calculated Q. We have verified that this stabilization is due to polarization and not other effects, such as photothermal effects, by confirming the polarization dependence of the observed stability.

We note that by varying the input polarization angle and hence the power in the C and the SC, the observed stability region shifts in agreement with the expected shifts in the detunings of the C and the SC polarizations, and lies in the stable region IV of Fig 5.2.

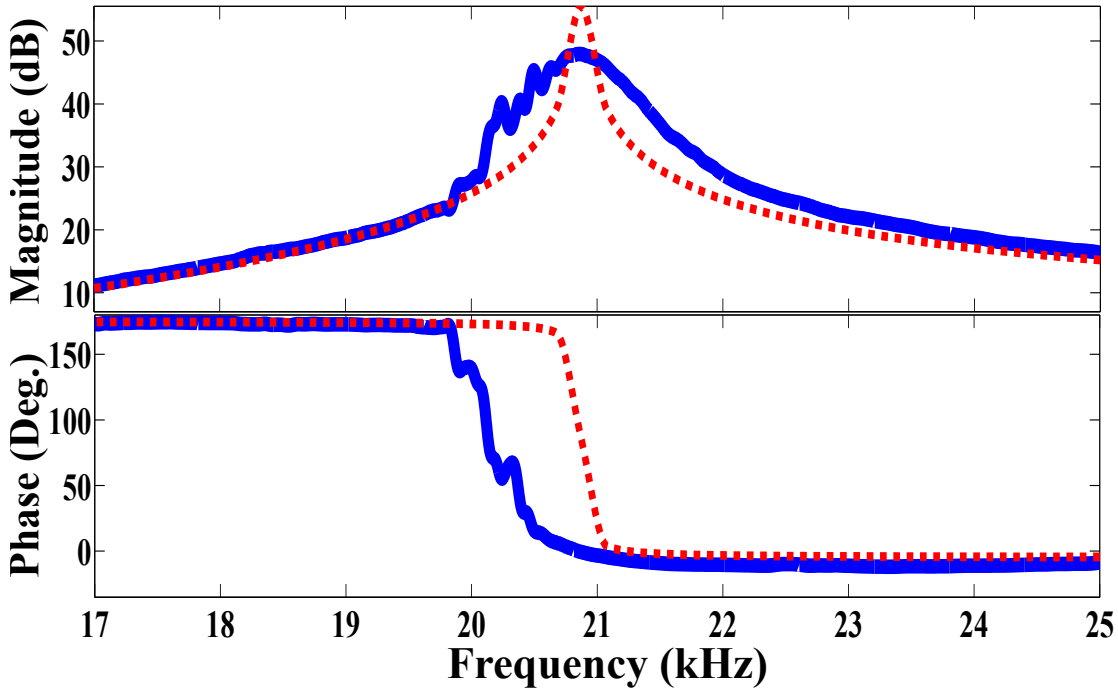

Figure 5.4: The measured transfer function of a signal sent to the amplitude modulator to the transmission photodetector of the carrier is shown (blue), along with the calculated optical response (dotted red). We note that this measurement is performed open-loop, where the feedback signal to the amplitude modulator is turned off here and the cavity is self-stabilized as a result of an optical trap. The disagreement between the measured and calculated Q is attributed to the fact that the the resulting vibrations in the system are sufficient to jitter the intracavity power and modulate the optical spring frequency in the time that it takes to perform this measurement.

Further the Fig 5.5 shows the available range fot the stable optical trap. The experimental data is fitted to have a smooth fit for a better understanding of the dynamical range and the affects on the overall quality factor of the optical spring. Since the frequency shift is proportional to the birefringence, the range is fixed for a particular resonator unless a rotational degree of freedom is added to the microresonator end mirror. Such effects hence need further investigations to explore the full range of usable dynamics to achieve a high quality dual optical trap

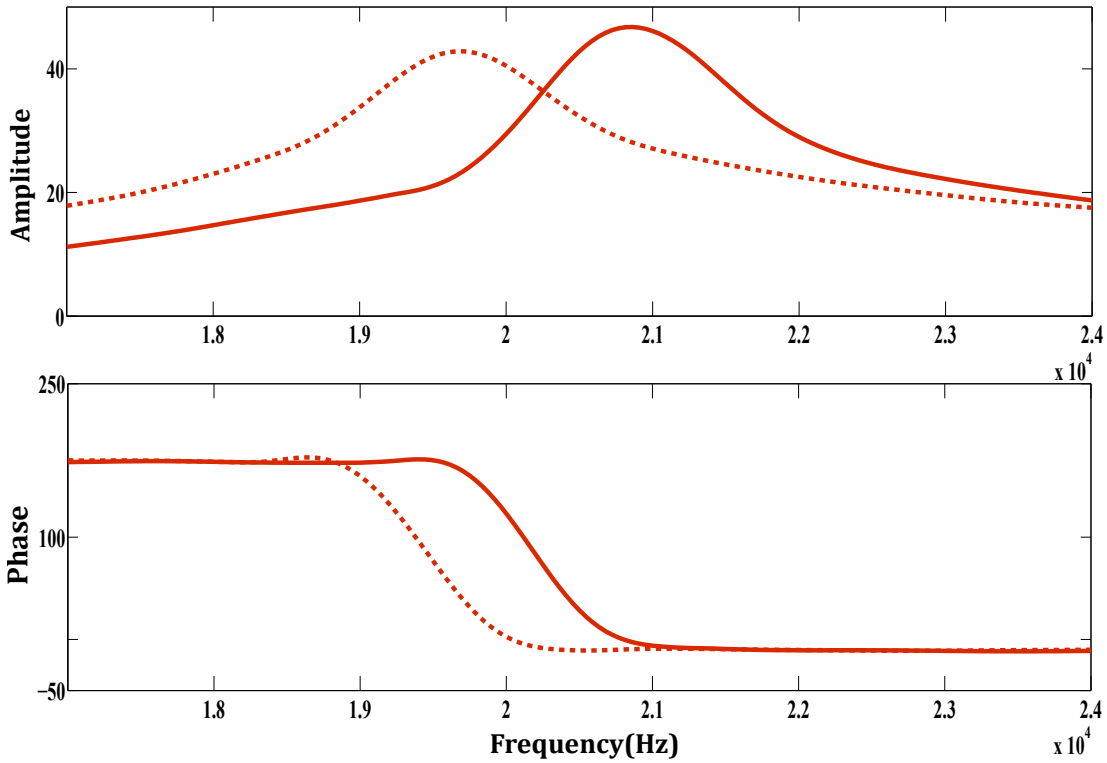

Figure 5.5: The smooth data showing the available range of stable optical trap due to the birefringence of the microresonator

5.3 Overview

Owing to the simplicity of the technique, the polarization based optical trapping technique has many potential applications that include but not limited to the high sensitivity optomechanical systems for gravitational wave detectors, dark matter detection, and many body interactions in a macroscopic system. Since our technique does not depend on the absorption, the application can be used without degrading the quantum limited sensitivity of the experiment. In conclusion, we have exhibited a polarization dependent stable optical trap for a microresonator based opto-mechanical system, as the outcome of a strong optical spring and optical damping. The dynamics of the system are controlled by the radiation pressure and depend on the detunings of the polarization components of the input field. We experimentally demonstrated the stability of the system and confirmed that the deactivation of the feedback control does not render the system unstable. We believe our scheme to be a useful technique for manipulating and stabilizing the dynamics

of the vast variety of opto-mechanical systems. We note that it would beneficial to have control over the birefringence effect, so that the difference in the detunings of the carrier and subcarrier, $\delta_{\mathrm{C}} - \delta_{\mathrm{SC}}$ could be adjusted, ideally to lie in the range of about 3γ. In the present measurement, the large separation of the two polarizations leads to a smaller than desired optical spring.

References

[1] C. W. Misner, K. S. Thorne, and J.A Wheeler. Gravitation.

[2] R. A. Hulse and J. H. Taylor. Discovery of a pulsar in a binary system. , 195:L51–L53, January 1975.

[3] J. H. Taylor and J. M. Weisberg. Further experimental tests of relativistic gravity using the binary pulsar PSR 1913 + 16. , 345:434–450, October 1989.

[4] B. P. et. al. Abbott. Observation of gravitational waves from a binary black hole merger. *Phys. Rev. Lett.*, 116:061102, Feb 2016.

[5] B.P. et.al. Abbott. Properties of the binary black hole merger gw150914. *LIGO-P1500218*, 2016.

[6] J. Weber. Detection and generation of gravitational waves. *Phys. Rev.*, 117:306–313, Jan 1960.

[7] E. Mauceli, Z. K. Geng, W. O. Hamilton, W. W. Johnson, S. Merkowitz, A. Morse, B. Price, and N. Solomonson. The allegro gravitational wave detector: Data acquisition and analysis. *Phys. Rev. D*, 54:1264–1275, Jul 1996.

[8] M Cerdonio, M Bonaldi, D Carlesso, E Cavallini, S Caruso, A Colombo, P Falferi, G Fontana, P L Fortini, R Mezzena, A Ortolan, G A Prodi, L Taffarello, G Vedovato, S Vitale, and J P Zendri. The ultracryogenic gravitational-wave detector auriga. *Classical and Quantum Gravity*, 14(6):1491, 1997.

[9] P. Astone, D. Babusci, M. Bassan, P. Carelli, G. Cavallari, E. Coccia, C. Cosmelli, S. D'Antonio, V. Fafone, A. C. Fauth, G. Federici, G. Giordano, A. Marini, Y. Minenkov, I. Modena, G. Modestino, A. Moleti, G. V. Pallottino, G. Pizzella, L. Quintieri, A. Rocchi, F. Ronga, R. Terenzi, G. Torrioli, and M. Visco. Increasing the bandwidth of resonant gravitational antennas: The case of explorer. *Phys. Rev. Lett.*, 91:111101, Sep 2003.

[10] E. Coccia, V. Fafone, G. Frossati, J. A. Lobo, and J. A. Ortega. Hollow sphere as a detector of gravitational radiation. *Phys. Rev. D*, 57:2051–2060, Feb 1998.

[11] N.P. Linthorne, P.J. Veitch, D.G. Blair, P.J. Turner, M.E. Tobar, and A.G. Mann. Niobium gravitational radiation antenna with superconducting parametric transducer. *Physica B: Condensed Matter*, 165:9 – 10, 1990.

[12] J. A. Ellis, X. Siemens, and J. D. E. Creighton. Optimal strategies for continuous gravitational wave detection in pulsar timing arrays. *The Astrophysical Journal*, 756(2):175, 2012.

[13] Robert L. Forward. Wideband laser-interferometer graviational-radiation experiment. *Phys. Rev. D*, 17:379–390, Jan 1978.

[14] R. Weiss. Electromagnetically coupled broadband gravitational antenna.

[15] P. Linsay, P. Saulson, R. Weiss, National Science Foundation (U.S.), Massachusetts Institute of Technology. Gravitation Research Group, Inc Arthur D. Little, Stone, and Webster Engineering Corporation. *A Study of a Long Baseline Gravitational Wave Antenna System*. publisher not identified, 1983.

[16] B. P. Abbott, R. Abbott, T. D. Abbott, M. R. Abernathy, F. Acernese, K. Ackley, C. Adams, T. Adams, P. Addesso, R. X. Adhikari, and et al. Prospects for Observing and Localizing Gravitational-Wave Transients with Advanced LIGO and Advanced Virgo. *Living Reviews in Relativity*, 19, February 2016.

[17] Gregory M Harry, Matthew R Abernathy, Andres E Becerra-Toledo, Helena Armandula, Eric Black, Kate Dooley, Matt Eichenfield, Chinyere Nwabugwu, Akira Villar, D R M Crooks, Gianpietro Cagnoli, Jim Hough, Colin R How, Ian MacLaren, Peter Murray, Stuart Reid, Sheila Rowan, Peter H Sneddon, Martin M Fejer, Roger Route, Steven D Penn, Patrick Ganau, Jean-Marie Mackowski, Christophe Michel, Laurent Pinard, and Alban Remillieux. Titania-doped tantala/silica coatings for gravitational-wave detection. *Classical and Quantum Gravity*, 24(2):405, 2007.

[18] Brian J. Meers. Recycling in laser-interferometric gravitational-wave detectors. *Phys. Rev. D*, 38:2317–2326, Oct 1988.

[19] B. P. et. al. Abbott. Gw150914: The advanced ligo detectors in the era of first discoveries. *Phys. Rev. Lett.*, 116:131103, Mar 2016.

[20] Gabriela Gonzlez. Suspensions thermal noise in the ligo gravitational wave detector. *Classical and Quantum Gravity*, 17(21):4409, 2000.

[21] A V Cumming, L Cunningham, G D Hammond, K Haughian, J Hough, S Kroker, I W Martin, R Nawrodt, S Rowan, C Schwarz, and A A van Veggel. Silicon mirror suspensions for gravitational wave detectors. *Classical and Quantum Gravity*, 31(2):025017, 2014.

[22] Yu. Levin. Internal thermal noise in the ligo test masses: A direct approach. *Phys. Rev. D*, 57:659–663, Jan 1998.

[23] Massimo Granata, Emeline Saracco, Nazario Morgado, Alix Cajgfinger, Gianpietro Cagnoli, Jérôme Degallaix, Vincent Dolique, Danièle Forest, Janyce Franc, Christophe Michel, Laurent Pinard, and Raffaele Flaminio. Mechanical loss in state-of-the-art amorphous optical coatings. *Phys. Rev. D*, 93:012007, Jan 2016.

[24] Peter R. Saulson. Thermal noise in mechanical experiments. *Phys. Rev. D*, 42:2437–2445, Oct 1990.

[25] J. Agresti, G. Castaldi, R. DeSalvo, V. Galdi, V. Pierro, and I. M. Pinto. Optimized multilayer dielectric mirror coatings for gravitational wave interferometers. In *Society of Photo-Optical Instrumentation Engineers (SPIE) Conference Series*, volume 6286 of , page 628608, August 2006.

[26] G. Cagnoli, J. Hough, D. DeBra, M.M. Fejer, E. Gustafson, S. Rowan, and V. Mitrofanov. Damping dilution factor for a pendulum in an interferometric gravitational waves detector. *Physics Letters A*, 272(12):39 – 45, 2000.

[27] M. Bassan. *Advanced Interferometers and the Search for Gravitational Waves: Lectures from the First VESF School on Advanced Detectors for Gravitational Waves*. Astrophysics and Space Science Library. Springer International Publishing, 2014.

[28] Garrett D. Cole. Cavity optomechanics with low-noise crystalline mirrors. In *Proc. SPIE 8458, Optics & Photonics, Optical Trapping and Optical Micromanipulation IX*, page 8458?07. SPIE, August 2012.

[29] G. D. Cole, W. Zhang, M. J. Martin, J. Ye, and M. Aspelmeyer. Tenfold reduction of Brownian noise in high-reflectivity optical coatings. newblock *Nature Photonics*, 7, 644-650, 2013.

[30] Garrett D. Cole, Simon Gröblacher, Katharina Gugler, Sylvain Gigan, and Markus Aspelmeyer. Monocrystalline $Al_xGa_{1-x}As$ heterostructures for high-reflectivity high-Q micromechanical resonators in the megahertz regime. *Applied Physics Letters*, 92(26):261108, 2008.

[31] Garrett D. Cole, Pen-Li Yu, Claus Gärtner, Karoline Siquans, Ramon Moghadas Nia, Jonas Schmle, Jason Hoelscher-Obermaier, Thomas P. Purdy, Witlef Wieczorek, Cindy A. Regal, and Markus Aspelmeyer. Tensile-strained $InGa_{1-x}P$ membranes for cavity optomechanics. *Applied Physics Letters*, 104(20), 2014.

[32] Carlton M. Caves. Quantum-mechanical radiation-pressure fluctuations in an interferometer. *Phys. Rev. Lett.*, 45:75–79, Jul 1980.

[33] Carlton M. Caves. Quantum-mechanical noise in an interferometer. *Phys. Rev. D*, 23:1693–1708, Apr 1981.

[34] H. J. Kimble, Yuri Levin, Andrey B. Matsko, Kip S. Thorne, and Sergey P. Vyatchanin. Conversion of conventional gravitational-wave interferometers into quantum nondemolition interferometers by modifying their input and/or output optics. *Phys. Rev. D*, 65:022002, Dec 2001.

[35] T. R. Corbitt. Quantum noise and radiation pressure effects in high power optical interferometers. *Ph.D Thesis, Massachusetts Institute of Technology*, August 2008.

[36] S. L. Danilishin and F. Y. Khalili. Quantum measurement theory in gravitational-wave detectors. *Living Rev. Relativity*, 15, 2012.

[37] Carlton M. Caves and Bonny L. Schumaker. New formalism for two-photon quantum optics. i. quadrature phases and squeezed states. *Phys. Rev. A*, 31:3068–3092, May 1985.

[38] Bonny L. Schumaker and Carlton M. Caves. New formalism for two-photon quantum optics. ii. mathematical foundation and compact notation. *Phys. Rev. A*, 31:3093–3111, May 1985.

[39] Thomas Corbitt, Yanbei Chen, and Nergis Mavalvala. Mathematical framework for simulation of quantum fields in complex interferometers using the two-photon formalism. *Phys. Rev. A*, 72:013818, Jul 2005.

[40] T. P. Purdy, P.-L. Yu, R. W. Peterson, N. S. Kampel, and C. A. Regal. Strong optomechanical squeezing of light. *Phys. Rev. X*, 3:031012, Sep 2013.

[41] Daniel W. C. Brooks, Thierry Botter, Sydney Schreppler, Thomas P. Purdy, Nathan Brahms, and Dan M. Stamper-Kurn. Non-classical light generated by quantum-noise-driven cavity optomechanics. *Nature*, 488(7412):476–480, August 2012.

[42] A. Pontin, C. Biancofiore, E. Serra, A. Borrielli, F. S. Cataliotti, F. Marino, G. A. Prodi, M. Bonaldi, F. Marin, and D. Vitali. Frequency-noise cancellation in optomechanical systems for ponderomotive squeezing. *Phys. Rev. A*, 89:033810, Mar 2014.

[43] V. B. Braginsky, Khalili F. B., and K. S. Thorne. *Quantum measurement*. Cambridge University Press, 1995.

[44] V. B. Braginskiĭ. Classical and Quantum Restrictions on the Detection of Weak Disturbances of a Macroscopic Oscillator. *Soviet Journal of Experimental and Theoretical Physics*, 26:831, April 1968.

[45] S.P. Vyatchanin. The estimation of signal force parameters in quantum variation measurement. *Physics Letters A*, 239(45):201 – 208, 1998.

[46] S. P. Vyatchanin and Matsko A. B. Quantum variational measurements of force and compensation of the nonlinear backaction in an interferometric displacement transducer. *JETP*, October 1996.

[47] S.P. Vyatchanin and E.A. Zubova. Quantum variation measurement of a force. *Physics Letters A*, 201(4):269 – 274, 1995.

[48] R. E. Slusher, L. W. Hollberg, B. Yurke, J. C. Mertz, and J. F. Valley. Observation of squeezed states generated by four-wave mixing in an optical cavity. *Phys. Rev. Lett.*, 55:2409–2412, Nov 1985.

[49] Ling-An Wu, H. J. Kimble, J. L. Hall, and Huifa Wu. Generation of squeezed states by parametric down conversion. *Phys. Rev. Lett.*, 57:2520–2523, Nov 1986.

[50] K. Schneider, M. Lang, J. Mlynek, and S. Schiller. Generation of strongly squeezed continuous-wave light at 1064 nm. *Opt. Express*, 2(3):59–64, Feb 1998.

[51] Henning Vahlbruch, Moritz Mehmet, Simon Chelkowski, Boris Hage, Alexander Franzen, Nico Lastzka, Stefan Goßler, Karsten Danzmann, and Roman Schnabel. Observation of squeezed light with 10-db quantum-noise reduction. *Phys. Rev. Lett.*, 100:033602, Jan 2008.

[52] T. W. Hansch and A. L. Schawlow. Cooling of gases by laser radiation. *Optics Communications*, 13:68, January 1975.

[53] D. J. Wineland and Wayne M. Itano. Laser cooling of atoms. *Phys. Rev. A*, 20:1521–1540, Oct 1979.

[54] Stig Stenholm. The semiclassical theory of laser cooling. *Rev. Mod. Phys.*, 58:699–739, Jul 1986.

[55] Markus Aspelmeyer, Tobias J. Kippenberg, and Florian Marquardt. Cavity optomechanics. *Rev. Mod. Phys.*, 86:1391–1452, Dec 2014.

[56] Thomas Corbitt, Yanbei Chen, Edith Innerhofer, Helge Müller-Ebhardt, David Ottaway, Henning Rehbein, Daniel Sigg, Stanley Whitcomb, Christopher Wipf, and Nergis Mavalvala. An all-optical trap for a gram-scale mirror. *Phys. Rev. Lett.*, 98:150802, Apr 2007.

[57] Thomas Corbitt, Christopher Wipf, Timothy Bodiya, David Ottaway, Daniel Sigg, Nicolas Smith, Stanley Whitcomb, and Nergis Mavalvala. Optical dilution and feedback cooling of a gram-scale oscillator to 6.9 mk. *Phys. Rev. Lett.*, 99:160801, Oct 2007.

[58] Benjamin S. Sheard, Malcolm B. Gray, Conor M. Mow-Lowry, David E. McClelland, and Stanley E. Whitcomb. Observation and characterization of an optical spring. *Phys. Rev. A*, 69:051801, May 2004.

[59] V.B. Braginsky and S.P. Vyatchanin. Low quantum noise tranquilizer for fabryperot interferometer. *Physics Letters A*, 293(56):228 – 234, 2002.

[60] F. Sugihwo, M. C. Larson, and J. S. Harris. Simultaneous optimization of membrane reflectance and tuning voltage for tunable vertical cavity lasers. *Applied Physics Letters*, 72(1):10–12, 1998.

[61] W. Z. Korth, H. Miao, T. Corbitt, G. D. Cole, Y. Chen, and R. X. Adhikari. Suppression of quantum-radiation-pressure noise in an optical spring. *Phys. Rev. A*, 88, 033805, 4 September 2013.

[62] G. D. Cole, E. S. Bjorlin, Qi Chen, Chung-Yeung Chan, Shaomin Wu, C. S. Wang, N. C. MacDonald, and J. E. Bowers. Mems-tunable vertical-cavity SOAs. *IEEE Journal of Quantum Electronics*, 41(3):390–407, March 2005.

[63] Garrett D. Cole, Elaine Behymer, Tiziana C. Bond, and Lynford L. Goddard. Short-wavelength mems-tunable vcsels. *Opt. Express*, 16(20):16093–16103, Sep 2008.

[64] Simon Groblacher, Jared B. Hertzberg, Michael R. Vanner, Garrett D. Cole, Sylvain Gigan, K. C. Schwab, and Markus Aspelmeyer. Demonstration of an ultracold micro-optomechanical oscillator in a cryogenic cavity. *Nat Phys*, 5(7):485–488, July 2009.

[65] Garrett D. Cole, Wei Zhang, Michael J. Martin, Jun Ye, and Markus Aspelmeyer. Tenfold reduction of brownian noise in high-reflectivity optical coatings. *Nat Photon*, 7(8):644–650, August 2013.

[66] Gregory M. Harry, Helena Armandula, Eric Black, D. R. M. Crooks, Gianpietro Cagnoli, Jim Hough, Peter Murray, Stuart Reid, Sheila Rowan, Peter Sneddon, Martin M. Fejer, Roger Route, and Steven D. Penn. Thermal noise from optical coatings in gravitational wave detectors. *Appl. Opt.*, 45(7):1569–1574, Mar 2006.

[67] Thomas Corbitt, David Ottaway, Edith Innerhofer, Jason Pelc, and Nergis Mavalvala. Measurement of radiation-pressure-induced optomechanical dynamics in a suspended fabry-perot cavity. *Phys. Rev. A*, 74:021802, Aug 2006.

[68] Garrett D. Cole, Wei Zhang, Bryce J. Bjork, David Follman, Paula Heu, Christoph Deutsch, Lindsay Sonderhouse, John Robinson, Chris Franz, Alexei Alexandrovski, Mark Notcutt, Oliver H. Heckl, Jun Ye, Markus Aspelmeyer. High-performance near- and mid-infrared crystalline coatings. *arXiv:1604.00065*.

[69] Alessandra Buonanno and Yanbei Chen. Signal recycled laser-interferometer gravitational-wave detectors as optical springs. *Phys. Rev. D*, 65:042001, Jan 2002.

[70] Alessandra Buonanno and Yanbei Chen. Signal recycled laser-interferometer gravitational-wave detectors as optical springs. *Phys. Rev. D*, 65:042001, Jan 2002.

[71] Stefano Mancini, David Vitali, and Paolo Tombesi. Optomechanical cooling of a macroscopic oscillator by homodyne feedback. *Phys. Rev. Lett.*, 80:688–691, Jan 1998.

[72] Osamu Miyakawa, Robert Ward, Rana Adhikari, Matthew Evans, Benjamin Abbott, Rolf Bork, Daniel Busby, Jay Heefner, Alexander Ivanov, Michael Smith, Robert Taylor, Stephen Vass, Alan Weinstein, Monica Varvella, Seiji Kawamura, Fumiko Kawazoe, Shihori Sakata, and Conor Mow-Lowry. Measurement of optical response of a detuned resonant sideband extraction gravitational wave detector. *Phys. Rev. D*, 74:022001, Jul 2006.

[73] T. J. Kippenberg, H. Rokhsari, T. Carmon, A. Scherer, and K. J. Vahala. Analysis of radiation-pressure induced mechanical oscillation of an optical microcavity. *Phys. Rev. Lett.*, 95:033901, Jul 2005.

[74] David Kelley, James Lough, Fabian Mangaña Sandoval, Antonio Perreca, and Stefan W. Ballmer. Observation of photothermal feedback in a stable dual-carrier optical spring. *Phys. Rev. D*, 92:062003, Sep 2015.

[75] Antonio Perreca, James Lough, David Kelley, and Stefan W. Ballmer. Multidimensional optical trapping of a mirror. *Phys. Rev. D*, 89:122002, Jun 2014.

[76] Armen E Allahverdyan, Karen Hovhannisyan, and Guenter Mahler. Optimal refrigerator. *Physical Review E*, 81(5):051129, 2010.

[77] Marlan O. Scully, M Suhail Zubairy, Girish S Agarwal, and Herbert Walther. Extracting work from a single heat bath via vanishing quantum coherence. *Science*, 299(5608):862–864, 2003.

[78] Robert Alicki. The quantum open system as a model of the heat engine. *Journal of Physics A: Mathematical and General*, 12(5):L103, 1979.

[79] HT Quan, Y Liu, CP Sun, and Franco Nori. Quantum thermodynamic cycles and quantum heat engines. *Physical Review E*, 76(3):031105, 2007.

[80] Herbert Spohn. Entropy production for quantum dynamical semigroups. *Journal of Mathematical Physics*, 19:1227, 1978.

[81] Xiaoting Wang, Sai Vinjanampathy, Frederick W. Strauch, and Kurt Jacobs. Ultraefficient cooling of resonators: Beating sideband cooling with quantum control. *Phys. Rev. Lett.*, 107:177204, Oct 2011.

[82] Xiaoting Wang, Sai Vinjanampathy, Frederick W. Strauch, and Kurt Jacobs. Absolute dynamical limit to cooling weakly coupled quantum systems. *Phys. Rev. Lett.*, 110:157207, Apr 2013.

[83] S. Machnes, J. Cerrillo, M. Aspelmeyer, W. Wieczorek, M. B. Plenio, and A. Retzker. Pulsed laser cooling for cavity optomechanical resonators. *Phys. Rev. Lett.*, 108:153601, Apr 2012.

[84] Simon Stellmer, Benjamin Pasquiou, Rudolf Grimm, and Florian Schreck. Laser cooling to quantum degeneracy. *Phys. Rev. Lett.*, 110:263003, Jun 2013.

[85] K. Helmerson, D. Hutchinson, K. Burnett, and W. D. Phillips. Atom lasers. *Physics World*, page 31, August 1999.

[86] K. Gibble and S. Chu. Atomic clocks and cold atom scattering. *Metrologia*, page 201, 1992.

[87] T. W. Hansch and A. L. Schawlow. Cooling of gases by laser radiation. *Optics Communications*, 13:68, January 1975.

[88] D. J. Wineland, R. E. Drullinger, and F. L. Walls. Radiation-pressure cooling of bound resonant absorbers. *Phys. Rev. Lett.*, 40:1639–1642, Jun 1978.

[89] William D. Phillips. Nobel lecture: Laser cooling and trapping of neutral atoms. *Rev. Mod. Phys.*, 70:721–741, Jul 1998.

[90] D. J. Wineland, J. Dalibard, and C. Cohen-Tannoudji. Sisyphus cooling of a bound atom. *J. Opt. Soc. Am. B*, 9(1):32–42, Jan 1992.

[91] J. Dalibard and C. Cohen-Tannoudji. Laser cooling below the doppler limit by polarization gradient: simple theoretical models. *J. Opt. Soc. Am. B*, pages 2023–2045, 1989.

[92] Harold Metcalf. Entropy exchange in laser cooling. *Phys. Rev. A*, 77:061401, Jun 2008.

[93] S. E. Galica, L. Aldridge, and E. E. Eyler. Four-color stimulated optical forces for atomic and molecular slowing. *Phys. Rev. A*, 88:043418, Oct 2013.

[94] Christopher Corder, Brian Arnold, and Harold Metcalf. Laser cooling without spontaneous emission. *Phys. Rev. Lett.*, 114:043002, Jan 2015.

[95] Wolfgang Ketterle and David E. Pritchard. Atom cooling by time-dependent potentials. *Phys. Rev. A*, 46:4051–4054, Oct 1992.

[96] G. S. Agarwal and K. Tara. Nonclassical properties of states generated by the excitations on a coherent state. *Phys. Rev. A*, 43:492–497, Jan 1991.

[97] A. Zavatta, S. Viciani, and M. Bellini. Quantum-to-classical transition with single-photon-added coherent states of light. *Science*, 306:660–662, 22 Oct 2004.

[98] E.T. Jaynes and F.W. Cummings. Comparison of quantum and semiclassical radiation theories with application to the beam maser. *Proceedings of the IEEE*, 51.

[99] Stephen Barnett and Paul M. Radmore. *Methods in Theoretical Quantum Optics*. Oxford University Press, USA, 1997.

[100] M. Sargent and M. O. Scully. *Laser Physics*. Addison-Wesley, New York, USA, 1974.

[101] Daniel A. Steck. Rubidium 87 d line data. 23 Dec 2010. Available at http://steck.us/alkalidata.

Appendix A
Calculation of the Optical Spring

A.1 Optical Spring

For complete form for the optical spring, we need should identify the source of decoherence for the cavity decay. Under the assumption of no scattering losses, the cavity decay rate is an outcome of the finite transmission of the optical mirrors in the cavity For an input electric field $E_{\rm in}$, the displacement operator $\hat{x}_n$ for the vibrational modes of a mirrored resonator can be represented as harmonic oscillation around the measurement frequency [75].

$$\hat{x}_n(\Omega) = x_o e^{i\Omega t} e^{-i\Omega(2n-1)\tau} \tag{A.1}$$

where x_o is the zero point motion of the mirror, $\tau = L/c$ is the time taken by light to travel from the input mirror to the movable end mirror, L is the length of the Fabry-Perot cavity. Under the approximation that the measurement frequency cavity linewidth $\Omega << \gamma$, and single mode cavity, $n = 1$.

For the transmission amplitude t_1 of the input mirror, the coupled optical field into the cavity is $t_1 E_{\rm in}$. The displacement x_1 of the movable end mirror causes the phase shift of the circulating optical field. If r_1 and r_2 are the reflection amplitudes of the input mirror and the movable end mirror, the total circulating optical field can be written as:

$$E_{\rm circ} = t_1 E_{\rm in} + t_1 E_{\rm in} r_1 r_2 e^{-i2k(L+x_1)} \Rightarrow t_1 E_{\rm in}(1 + r_1 r_2 e^{-i2kL} e^{i2x_1}) \tag{A.2}$$

where the factor of 2 comes due to the field being reflected and hence the total distance covered by the circulating field is $2L$.

To the first order approximation, the above equation can be written as:

$$E_{\text{circ}} \approx \frac{t_1 E_{\text{in}}}{1 - r_1 r_2 e^{-i2kL}} \left\{ 1 - \frac{i2kx_1 r_1 r_2 e^{-i2kL}}{1 - r_1 r_2 e^{-i2kL}} \right\}. \tag{A.3}$$

Therefore the power circulating inside the cavity is:

$$P_{\text{circ}} = -\|E_{\text{circ}}\|^2 = \left\| \frac{t_1 E_{\text{in}}}{1 - r_1 r_2 e^{-i2kL}} \left\{ 1 - \frac{i2kx_1 r_1 r_2 e^{-i2kL}}{1 - r_1 r_2 e^{-i2kL}} \right\} \right\|^2. \tag{A.4}$$

$$P_{\text{circ}} \approx \frac{{t_1}^2 {E_{\text{in}}}^2 r_1 r_2 x}{(1 - r_1 r_2 e^{-i2kL})(1 - r_1 r_2 e^{i2kL})} \left\{ \frac{r_1 r_2 e^{-i2kL}}{1 - r_1 r_2 e^{-i2kL}} + \frac{r_1 r_2 e^{i2kL}}{1 - r_1 r_2 e^{ikL}} \right\} \tag{A.5}$$

By definition of the optical spring.

$$2F_{\text{rad}} = -K_{\text{os}} x \text{ and } F_{\text{rad}} = \tfrac{2{r_2}^2}{c} P_{\text{circ}}$$

Therefore after simplifying the above equation A.5 for a given detuning $\delta = \omega_o - \omega_c$. Under the approximation:

$$e^{-i2kL} = e^{-2i\delta\tau} \approx 1 - i2\delta\tau$$

The optical spring coefficient is given as:

$$K_{\text{os}} \approx -4P_{\text{in}} {t_1}^2 {r_2}^2 \frac{i2kr_1 r_2}{c(1 - r_1 r_2 + i2\delta r_1 r_2 \tau)(1 - r_1 r_2 - i2\delta r_1 r_2 \tau)} \times \left(\tfrac{1 - i2\delta\tau}{1 - r_1 r_2 (1 - i2\delta\tau} - \tfrac{1 - i2\delta\tau}{1 + r_1 r_2 (1 + i2\delta\tau} \right) \tag{A.6}$$

This under further definition of $\delta/\gamma = \delta_\gamma$ and wave number $k = 2\pi/\lambda_o$

$$K_{\text{os}} \approx \frac{16\pi P_{\text{in}} {t_1}^2 {r_2}^2 r_1 r_2}{c\lambda_o (1 - r_1 r_2)^3 (1 + \delta_\gamma)^2} \tag{A.7}$$

Appendix B
Laser Cooling by Stimulated Emission

B.1 Introduction

Thermodynamic tasks in the quantum regime have been the subject of intense study in the recent past, where quantum coherence can aid in improved performance. For instance, quantum thermal machines have been recently studied from the standpoint of efficiency of work extraction [76, 77, 78, 79] and entropy production [80]. Another example involves conventional schemes like sideband cooling that have been recently improved by the application of quantum control protocols [81, 82, 83]. Laser cooling often represents the first step in quantum-state engineering protocols that are important for various quantum technology tasks. Such tasks include preparing Bose-Einstein condensates [84] for precision metrology [85, 86] and engineering cold mesoscopic systems such as nano-mechanical resonators [73] for sensing.

Most conventional laser-cooling schemes, as shown in B.1, assume spontaneous emission to be the carrier of entropy lost by the atoms being cooled. Such cooling schemes, for example in Doppler cooling [87, 88], typically involve cooling of motional degrees of freedom by momentum exchange between the atoms and the field.

Since these conventional schemes do not take into account the cooling of any electronic degrees of freedom, such cooling methods only work for specific alkali atoms. Cooling of other atoms and molecules, which have excitations in multiple degrees of freedom, is not possible with these aforementioned cooling schemes. Furthermore, the efficiency of these spontaneous emission based cooling schemes is limited because of effects such as Doppler shift and optical pumping [89].

Sub-Doppler cooling of external and internal spin atomic degrees of freedom, along with the issues related to optical pumping and Doppler shifts, were addressed in Sisyphus

cooling by interacting atoms with counter-propagating, orthogonally polarized beams of light [90]. The random recoil fluctuations caused by spontaneous emission still limit the cooling of atomic momentum spread beyond the recoil limit [91]. Sub-recoil temperatures are attainable with techniques including velocity selective coherent population trapping and Raman cooling [91], but are only investigated for sub-micro-Kelvin regimes.

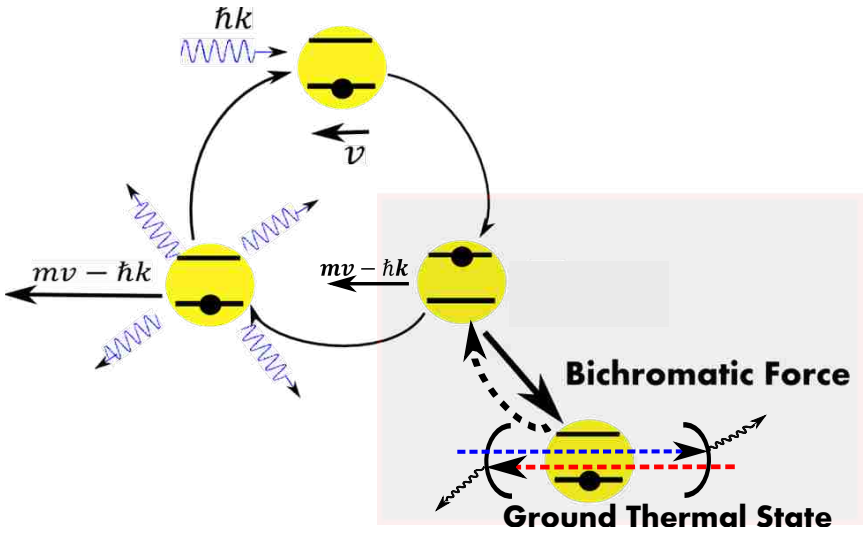

Figure B.1: Schematic of the conventional cooling scheme as compared to the cooling of excited energy states of the atoms by stimulated emission due to atomic interactions with the bichromatic field. Photon carrying momentum $\hbar k$ hits the atom travelling in opposite direction with velocity v. The gained photon is spontaneously emitted in random direction reducing the effective velocity to $v - \hbar k/m$. In bichromatic interactions the atom initially in random thermal state undergo stimulated emission to its ground thermal state.

Metcalf *et al.* [92], proposed a more efficient cooling scheme based on stimulated emission of the atoms produced by a bichromatic field. In yet another work, the control and the robustness of the bichromatic force was investigated [93]. It was suggested that the fields constitute enough of a reservoir to carry the entropy, lost by the atoms, away from the system being cooled. The controllability of the stimulated emission here serves as a mechanism to circumvent issues such as Doppler shifts, optical pumping, and the recoil limit. In later experimental investigations, Metcalf *et al.* [94] demonstrated such non-spontaneous emission based cooling of He atoms.

Furthermore, since the stimulated emission based cooling is not dependent on the random spontaneous emission of light, a broader range of atoms and even molecules can be prospectively cooled over a wide range of temperature. But in complex atomic systems and the molecules, the internal vibrational and rotational motions are more prominent rather than just the translational motion. Such investigation dealing with the de-excitation of the internal degrees of freedom has not been well studied for the stimulated emission model of cooling and hence need to be addressed for an efficient laser cooling scheme.

In this current article I carry out a study of bichromatic cooling to determine its feasibility for cooling of the internal degrees of freedom of atoms. I study the stimulated emission model for laser cooling of a two level atomic state, interacting with a standing wave of a bichromatic field. Such a model requires quantization of the field to incorporate both, the angular momentum transfer for cooling of internal degrees of freedom, and the entropy flow from the atom to the fields. In our model, the fields are used as the low-entropy reservoirs into which the atomic entropy is transferred [95]. I contrast this with standard cooling techniques where spontaneous emission is employed to transfer entropy. Interaction cycles for increasing average number of photons in the field were studied numerically to observe the flow of von-Neumann entropy in the atom-field system, the change in the population, and suggestively the excitation spread of the atom. I further show, by analyzing the Carnot-like thermodynamic cycles that this scheme of employing simulated emission using bichromatic field constitutes an efficient laser cooling scheme.

In Sec. B.2, I outline the physical system considered and various sources of decoherence. I also detail the control protocol used to cool the atomic degrees of freedom. In Sec. B.3, I solve for the dynamics of the two-level atom and highlight the cooling of the atom based on stimulated emission. In the final section, I present our conclusions.

B.2 Model Description

Our model of the physical system consists of a two-level atom interacting with a bichromatic field, schematically shown in Fig. B.2. Here the atomic states are represented

respectively by ground state $|g\rangle$ and excited state $|e\rangle$. Coherent states are used to describe the light field [96, 97]. The two counter-propagating light fields that are red and blue detuned with respect to the atomic transition frequency, form a standing wave of bichromatic field to a close approximation. Hence the atoms interacting with the bichromatic field experience a potential gradient that excites the atoms and subsequently pump the atoms to the ground states.

The standard Jaynes-Cummings interaction [98] is used to describe the atom-field interaction Hamiltonian of our system, namely:

$$\hat{H}_{\text{int}} = \hbar[g_r e^{-i\delta_r t}\hat{r}^\dagger\hat{\sigma}_- + g_b e^{-i\delta_b t}\hat{b}^\dagger\hat{\sigma}_-] + \text{H.C.} \tag{B.1}$$

where $\hat{\sigma}_\pm$ are the atomic raising and lowering operators, $\hat{r}^\dagger, \hat{b}^\dagger$ are the creation operators for the red and blue fields respectively, $\delta_{r,b}$ are the detunings of the fields and $\mathrm{g}_{r,b}$ are the coupling constants.

The decay coefficients of the system that includes the atom and the bichromatic field, are set such that stimulated emission caused by the standing wave of the counter-propagating quantized bichromatic field is a dominant mode of de-excitation of the atom. This condition is important to show that the interacting fields provide an efficient reservoir for entropy flow.

The system as a whole loses its entropy through the field interactions with the outside environment at a rate of γ_r and γ_b for the red- and blue-detuned fields, respectively. To avoid Rabi flopping between the system and reservoirs, and hence staturating the entropy transfer, I assume a physical system where atoms interact with a fresh beam of pulsed laser fields. In our work, the above mentioned model of the physical system is simulated as a series of atomic interactions with a pure state bichromatic field. The time period for each interaction cycle is tuned to ensure efficient cooling. Furthermore the condition $\tau < 1/\gamma_{r,b}$ is imposed such that the relaxation time of the fields τ is slow enough to see the entropy changes in the interacting fields but fast enough that the fields decay without reheating

the atom.

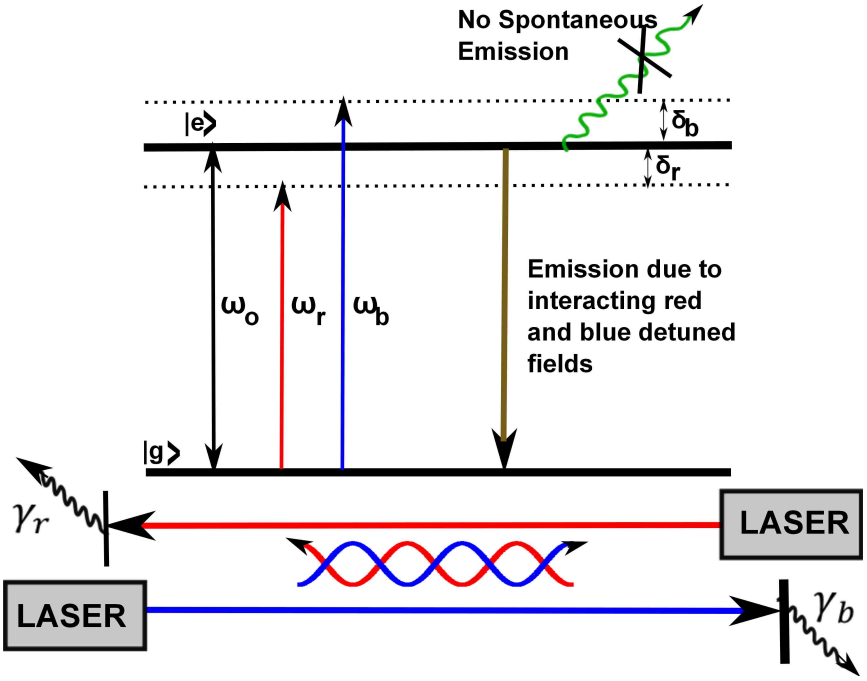

Figure B.2: Schematic for atomic interactions with a bichromatic field. The states $|g\rangle$ and $|e\rangle$ are the ground and excited energy states of the atomic subsystem. Fields at frequencies ω_b and ω_r are equally detuned ($\delta_r = -\delta_b$), above (blue) and below (red) from the atomic resonance frequency ω_o. Decay constants associated with the interaction of the fields with their respective environments are represented by γ_b and γ_r respectively.

Time evolution of the system density matrix ρ is calculated according the Lindblad Master equation given by Eq. B.2 [99, 100].

$$\dot{\hat{\rho}}(t) = \left[\begin{array}{c} -\frac{i}{\hbar}[\hat{H}_{\text{int}}, \hat{\rho}(t)] - \frac{\Gamma}{2}[\bar{n}+1]\mathcal{D}(\sigma_-)[\hat{\rho}(t)] - \frac{\Gamma}{2}[\bar{n}]\mathcal{D}(\sigma_+)[\hat{\rho}(t)] - \\ \sum_{k=r,b}\left[\frac{\Gamma_i}{2}[\bar{n}_k+1]\mathcal{D}(\sigma_-)[\hat{\rho}(t)] - \frac{\Gamma_k}{2}[\bar{n}_k]\mathcal{D}(\sigma_+)[\hat{\rho}(t)]\right] \end{array} \right] \tag{B.2}$$

Note that $\mathcal{D}(\hat{c})[\hat{\rho}(t)] := \{\hat{c}^\dagger\hat{c}, \hat{\rho}(t)\} - 2\hat{c}\hat{\rho}(t)\hat{c}^\dagger$ for operator $\hat{c}$. The sum over $k = r, b$ represents the interaction cycles for red-detuned and blue-detuned fields, respectively. At time $t = 0$, the initially uncorrelated state of the system $\hat{\rho}_A(0)$ is the thermal state given above and $\hat{\rho}_k(0)$ are the initial pure state density matrices of the respective fields.

In Eq. B.2, the second and third terms represent the evolution of the system to its

steady state at time t, and Γ is the decay coefficient related to it. Here $\bar{n}$ represents the number of thermal excitations in the atomic steady state given by plank's law. The fourth and the fifth terms represent the emission and absorption cycle of the atom-field interactions [99]. Γ_r, Γ_b are set much greater than $\Gamma = 1/\tau_a$, for τ_a to be the steady state lifetime of the atom. This condition artificially set the atom to be in quasi steady state during the interaction and hence compensates for the relatively lower quantum number of the field in our calculations. This would be not be an issue in the real experimental world, where the average field quantum number is in excess of 10^{10} per second.

B.3 Cooling by Stimulated Emission

I calculated the changes in von Neumann entropy of the atomic and the bichromatic field subsystems from their respective time-evolved density matrices. I further investigated the entropy profile of the total atom-field system along with changes in the ground state population of the atomic subsystem.

Our generalized model is an effort suggestive of stimulated emission based laser cooling in various atomic systems. For instance, here I investigated the system similar to the D_2 transition of Sodium atom with an atomic transition frequency ω_o of $2\pi \times 508.8$ THz [101]. Following the large detuning approximation, the coupling constants were set to inversely follow the detuning. A spread in the overall velocity distribution of the atom was considered as a result of the excited internal quantum states of the atom. For a weaker coupling regime the respective detunings of the red and the blue fields were set to be ∓ 1.5 MHz around ω_o and corresponds to a velocity spread $\Delta v = \delta\lambda/4\pi$ of about 0.29 m/s that is also the recoil velocity of the sodium atom . The decay coefficients Γ_r, Γ_b, for the two fields, were set equal to 100Γ. For a stronger coupling regime, the coupling constants were doubled and the detunings were reduced correspondingly.

Fig. B.3 shows the results of our calculations for entropy flow of the atom-field system during weakly and strongly coupled atomic interactions with the standing wave of the counter-propagating bichromatic field. Three distinct cases of field quantum numbers 8,

18, and 50 are presented. As expected, the decrease in the entropy of the atom is directly proportional to the increase in the field quantum number and the coupling between the atom and the fields. The lowered effects of the increased field for the $\bar{n}_{r,b} = 50$ case is understood to be the truncation error and hence resulting from the lower effective number of available modes.

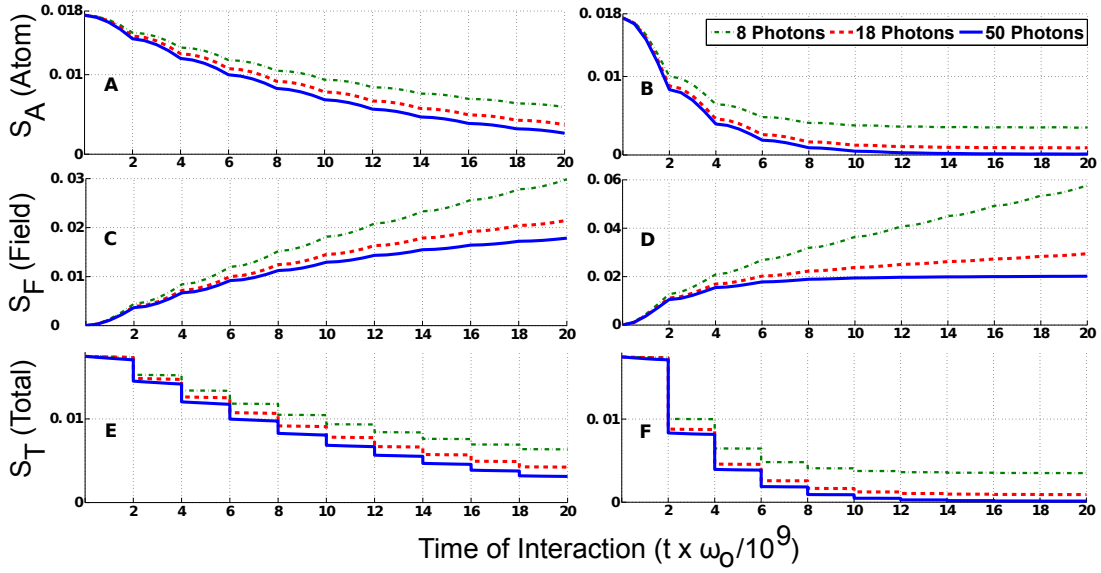

Figure B.3: Entropy flow during atomic interactions with the bichromatic field. Curves (I), (II), and (III) represent the results of atomic interactions with 8, 18, and 50 photon fields respectively. Subplots (A) and (B) show the change in entropy of the atom in the weak and strong coupling regimes. Subplots (C) and (D) show the corresponding changes in the entropy of the field in weak and strong coupling regimes. (E) and (F) are the changes in the total entropy of the system (atom and field). The steps at definite intervals of time are the injection points for the fresh field into the system.

Also from Fig. B.3, I see that the decrease in atomic entropy is accompanied by corresponding increase in the entropy of the light field. An increase in the reservoir capacity of the light field, with increasing field quantum number, is observed resulting from the increasing number of available modes in the fields. Discontinuities at definite time intervals are the injection points of fresh field into the system and are an artifact of our model. Although each interaction cycle with a fresh beam light field is parametrized to have no information of the previous cycle, I kept track of the cumulative entropy gained by the

fields to ascertain the total entropy lost from the system. The total entropy of the system, as expected, stays constant until the end of the interaction cycle where it undergoes a sharp decrease, owing to the fields carrying the entropy away from the whole system and dissipating it into the outside environment.

To ascertain the cooling of the atoms, I also studied the changes in the ground state and effectively the excited state population of the atomic subsystem as a function of the time of interaction. As evident in Fig. B.4, I see an increase in the ground state population of the atom. The change in the ground state atomic population of the atom is directly dependent on the intensity of the light field, and the coupling strength of the atom-field interaction. This dependence directly corresponds to the changes in the entropy of the atoms, hence I confirm the decrease in the entropy of the atoms to be the indicator of cooling the atomic sample towards its ground state.

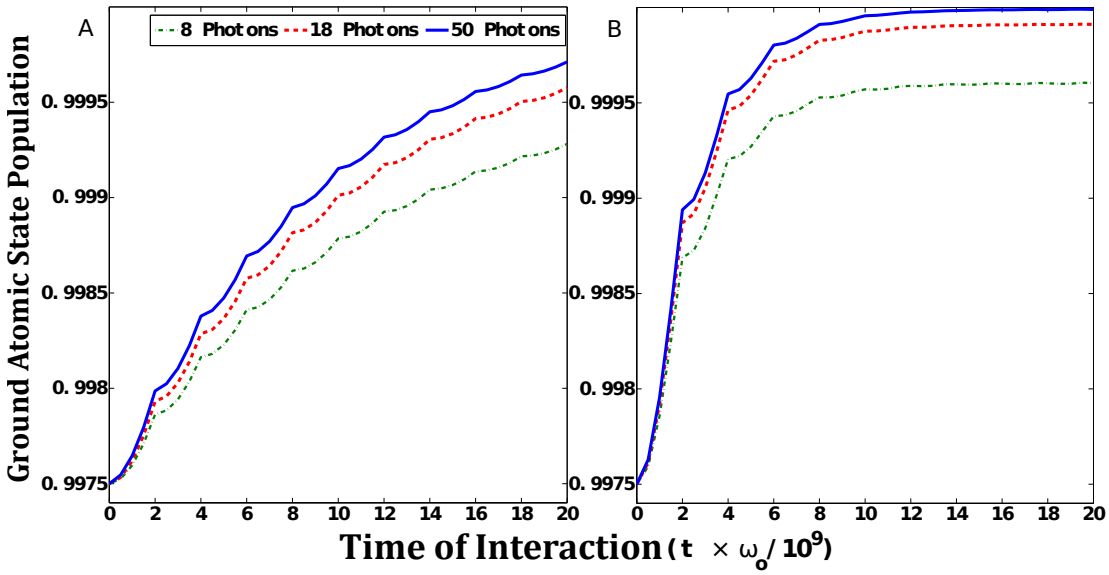

Figure B.4: Increase in population of the ground state of the atom during (A) weak and (B) strong interactions with the bichromatic field. As before (I),(II) and (III) are the changes due to interactions with 8-, 18- and 50-photon fields.

Further, the decrease in the probability of the excited state population of the atom indirectly corresponds to the decrease in the velocity spread and hence the temperature of

the atomic sample. Considering the energy states of the atom to be thermal, the population of the two atomic states can be described by the Boltzmann distribution. I calculated the maximum fractional change of the logarithm of the population of the atomic sample by a factor of 2, for the strong coupling regime of the field quantum number 50 that may suggest about $\times 1.4$ decrease in the velocity spread of the atomic sample being cooled . It is worth mentioning that the suggestive drop in the velocity spread requires further explicit analytic calculations to identify the cooling limit of our scheme.

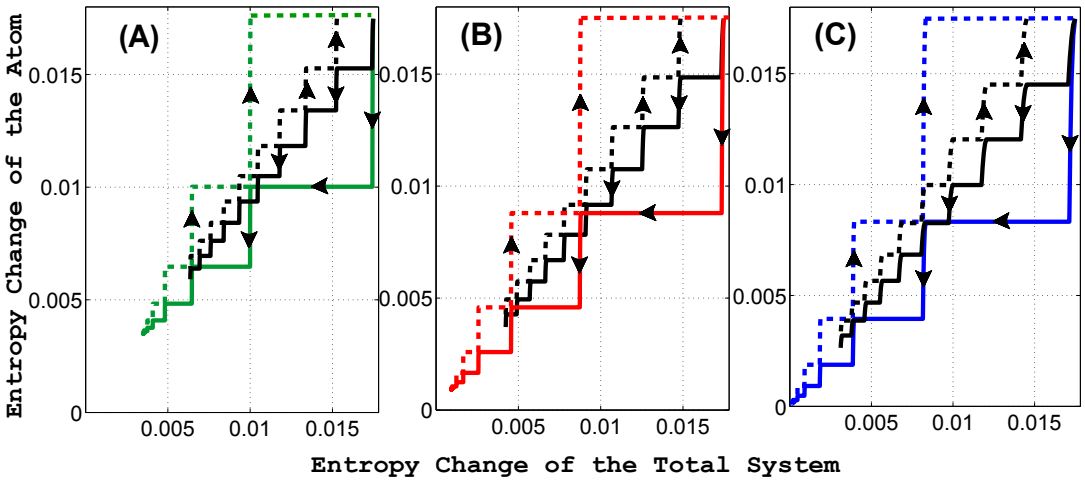

Figure B.5: Comparison of the thermodynamic cycle occurring during strong (green, red, and blue curves) and weak (black curve) atom-field interactions of the modeled system. Change in the total entropy of the system is plotted against the change in entropy of the atomic sample. Subplots (A), (B), and (C) are the cases for atom interacting with 8, 18, and 50 photon bichromatic field, respectively. Dotted curve in each subplot represents a hypothetical model for atom being heated by the field, back to its initial state.

Finally, to check the efficiency of cooling of our system, I investigate for a thermodynamic cycle between the entropy of the atom and the total entropy of the system. Since at the beginning and the end of the interaction cycles, the total entropy of the system is equal to that of the atoms, it makes sense to associate the entropy of the atom to the total entropy of the system. Hence the initial and final entropy of the atom can be regarded as that of the hot and cold reservoirs, respectively. The cycle can also be seen as energy passed out of the system for the amount supplied by the hot reservoir, which in our case

are approximately equal (as is evident from the initial and final entropy of the total system for each interaction cycle).

Fig. B.5 shows the relationship between the entropy change of the atomic subsystem and the total entropy change of the system, for both the weaker and the stronger coupling regime. I note that the cooling of the atoms becomes more and more efficient with an increase in the strength of the light field and that of the atom-field interactions. This increase in the efficiency, as a function of the field intensity and the interaction strength, is also evident from the cooling from total interaction. Hence our results are suggestive of our system reaching maximal efficiency at intense field strength and the appropriate coupling strength.

B.4 Conclusions

I presented a suggestive model for the efficient cooling by stimulated emission of two level atoms produced by a standing wave of counter-propagating bichromatic fields. The decrease in the entropy of the atoms along with an increase in the ground state population of the atoms, confirm the cooling of the atom to its ground state. The rise in the entropy of the fields along with a constant total entropy of the system during the interaction are suggestive of the fields being an efficient reservoir for the entropy lost by the atoms. While our simple model shows only cooling of internal degrees of freedom of the atoms, we can expect this cooling to be transferred to external (motional) degrees of freedom through collisions and thermal equilibrium. The cooling limit as such, and quantifying the relationship between rotational and vibrational atomic energy to the atomic states population, is still under investigation.

Stimulated emission of the atoms is evident from the atom-field entropy profile and the enhanced effects of increased field intensity on the atomic system.

Our numerical model is limited by the computation power available. Analytic calculations to further understand the dynamics of the more complicated system along with the consideration of ground-state splitting of the atomic state and other effects such as stronger

light fields, effects of polarization of the fields and center-of-mass motion of the atom are under ongoing investigation.

Vita

Robinjeet Singh obtained his basic education from St. Francis School, Tarn Taran, Punjab, India. His keen interest in the laws of Physics were developed, in the later years of his high school. He obtained his Bachelor's and then Master's degree in Physics from Guru Nanak Dev University, Amritsar, Punjab, India.

To further his endeavors in the field of experimental Physics, he enrolled in a Doctoral program in Physics at the Louisiana State University, Baton Rouge, LA, United States. His research under the advise of Dr. Jonathan P. Dowling and Dr. Thomas Corbitt, primarily involved investigations in the field of quantum optics and cavity optomechanics. He obtained Master of Science in Physics and Astronomy in 2013, from the Louisiana State University. He obtained his Ph.D. degree in Physics and Astronomy, on December 16, 2016.